SANDIA REPORT

SAND2000-0207
Unlimited Release
Printed January 2000

Final Report on LDRD Project: A Phenomenological Model for Multicomponent Transport with Simultaneous Electrochemical Reactions in Concentrated Solutions

Ken S. Chen, Gregory H. Evans, Richard S. Larson, David R. Noble, and William G. Houf

Prepared by
Sandia National Laboratories
Albuquerque, New Mexico 87185 and Livermore, California 94550

Sandia is a multiprogram laboratory operated by Sandia Corporation, a Lockheed Martin Company, for the United States Department of Energy under Contract DE-AC04-94AL85000.

Sandia National Laboratories

Issued by Sandia National Laboratories, operated for the United States Department of Energy by Sandia Corporation.

Available to DOE and DOE contractors from
Office of Scientific and Technical Information
P.O. Box 62
Oak Ridge, TN 37831

Prices available from (703) 605-6000
Web site: http://www.ntis.gov/ordering.htm

Available to the public from
National Technical Information Service
U.S. Department of Commerce
5285 Port Royal Rd
Springfield, VA 22161

NTIS price codes
Printed copy: A02
Microfiche copy: A01

SAND2000-0207
Unlimited Release
Printed January 2000

Final Report on LDRD Project: A Phenomenological Model for Multicomponent Transport with Simultaneous Electrochemical Reactions in Concentrated Solutions

Ken S. Chen*, Gregory H. Evans**, Richard S. Larson**, David R. Noble †, William G. Houf**

* Multiphase Transport Processes Department
† Microscale Sciences & Technology Department
Sandia National Laboratories
P.O. Box 5800
Albuquerque, New Mexico 87185-0834

** Chemical and Materials Process Modeling Department
Sandia National Laboratories
Livermore, CA 94550

ABSTRACT

This report documents the accomplishments in our LDRD project. A phenomenological model was developed for multicomponent transport of charged species with simultaneous electrochemical reactions in concentrated solutions, and was applied to model processes in a thermal battery cell. A new general framework was formulated and implemented in GOMA (a multidimensional, multiphysics, finite-element computer code developed and being enhanced at Sandia) for modeling multidimensional, multicomponent transport of neutral and charged species in concentrated solutions. The new framework utilizes the Stefan-Maxwell equations that describe multicomponent diffusion of interacting species using composition-insensitive binary diffusion coefficients. The new GOMA capability for modeling multicomponent transport of neutral species was verified and validated using the model problem of ternary gaseous diffusion in a Stefan tube. The new GOMA-based thermal battery computer model was verified using an idealized battery cell in which concentration gradients are absent; the full model was verified by comparing with that of Bernardi and Newman (1987) and validated using limited thermal battery discharge-performance data from the open literature (Dunning 1981) and from Sandia (Guidotti 1996). Moreover,

a new Liquid Chemkin Software Package was developed, which allows the user to handle many aspects of liquid-phase kinetics, thermodynamics, and transport (particularly in terms of computing properties). Lastly, a Lattice-Boltzmann-based capability was developed for modeling pore- or micro-scale phenomena involving convection, diffusion, and simplified chemistry; this capability was demonstrated by modeling phenomena in the cathode region of a thermal battery cell.

ACKNOWLEDGMENT

We would like to acknowledge the contribution of Michael E. Coltrin (Org. 1126) in the early stage of this project and the contribution of Fran M. Rupley (formerly Org. 8345) in coding the software routines in the Liquid Chemkin Package. We would like to thank Ronald A. Guidotti (Org. 2522) for sharing his knowledge and expertise on thermal batteries and for providing the thermal battery discharge-performance data used for model validation in this project. We would also like to acknowledge our collaboration with Harry K. Moffat (Org. 1126) on GOMA/Chemkin coupling, and helpful discussions with Gregory L. Scharrer (formerly Org. 2522 and currently Org. 2553) on thermal battery design. Moreover, we are indebted to the GOMA Development Team, particularly P. Randall Schunk (Org. 9114), Philip A. Sackinger (Org. 9111), Rekha R. Rao (Org. 9114), Thomas Baer (Org. 9114), and Samuel R. Subia (9111), for helpful discussions/assistance in GOMA implementation. Lastly, we would like to acknowledge the technical discussions with and the technical assistance from our consultants, Professors John Newman and Ralph Greif of UC Berkeley, and Professor John Weidner of Univ. of South Carolina, during the course of this project; and we are thankful to Professor J. A. Wesselingh of the University of Groningen, The Netherlands, for helpful comments on Chapter 4.

CONTENTS

1. INTRODUCTION

This report documents work performed in our LDRD project titled "A Phenomenological Model for Multicomponent Transport with Simultaneous Electrochemical Reactions in Concentrated Solutions", which was divided into four sub-tasks: 1) development of a new GOMA-based electrochemical computer model for a thermal battery cell (GOMA refers to a multidimensional, multiphysics, finite-element computer code developed and being enhanced at Sandia); 2) development of a new Liquid Chemkin software package; 3) estimation of Stefan-Maxwell diffusion coefficients for liquid-phase processes; and 4) microscale modeling of diffusion-controlled transport in a thermal battery cell using the Lattice-Boltzmann method. In the following, some background information and motivation for the project are presented. Salient features of thermal battery processes are discussed, and some relevant previous works are briefly reviewed. Lastly, a short description of the report's organization is given.

Many processes (e.g., thermal batteries, stockpile metal corrosion, electroforming, and LIGA fabrication of iMEMS devices) involve liquid-phase species transport with electrochemical reactions and are important to Sandia's DP mission. In the case of thermal batteries (the focus application of this project), the process involves multicomponent transport of charged species with simultaneous electrochemical reactions in a concentrated solution. More specifically, in a thermal battery cell, an interacting molten mixture of electrolytes is transported between electrode surfaces where electrochemical reactions take place. In terms of their importance, thermal batteries are employed as the primary power source in nuclear weapons because of inherent advantages such as long shelf life, fast activation, rugged construction, and high reliability (see Guidotti 1995 for a detailed technology review of thermal batteries and comments on future research and development directions). Most applications use lithium alloys (e.g., LiAl or Li(Si)) as anodes, metal-sulfides (e.g., FeS or FeS_2) as cathodes, and molten salts (e.g., LiCl-KCl, LiCl-LiBr-KBr, LiBr-KBr-LiF, LiCl-LiBr-LiF) as electrolytes. They are usually activated by melting the solid electrolytes using a pyrotechnic heat source based on Fe and $KClO_4$; typical operating temperatures are between 350 and 550°C. Two important characteristics of lithium and sulfur based thermal batteries are high open-circuit potential and high theoretical energy density. Reduced electrolyte decomposition, lowered ohmic resistance, and decreased mass-transfer limitations are the main advantages of employing molten salt electrolytes. High temperature operation also results in relatively fast electrochemical reactions. Operating at higher temperatures, however, causes increased corrosion and increased volatility and solubility of the active materials (cf. Bernardi 1986, Bernardi and Newman 1987).

Complex multi-physics phenomena occur in a thermal battery process including: i) thermodynamics (open-circuit potential sets the upper bound for the total cell voltage); ii) multi-species diffusion in a concentrated solution (solventless molten salt electrolyte) driven by gradients in both concentration and electrical potential where the conventional Fick's first law does not apply; iii) convection caused by diffusion and/or electrochemical reactions having molar volume differences between the products and reactants; iv) energy transport (heat loss to the environment and Joule heating are the two main sources responsible for temperature gradients and time-dependent behavior of cell temperature); v) electrochemical reactions at electrolyte/electrode interfaces

(chemical composition and phases vary significantly as the state of discharge changes). Besides multi-physics phenomena, a thermal battery process involves multiple length scales ranging from submicron dimensions in electrode pores to a fraction of a millimeter in the electrode and separator regions in the direction of ionic transport, and up to several centimeters in the direction normal to ionic transport and at the system unit level. Inherent in the multi-physics phenomena of species diffusion, convection, heat transfer, and electrochemical kinetics are multiple time scales. Lastly and very importantly, a thermal battery process is multi-dimensional mainly due to two factors: 1) energy transport occurs in both the direction of species diffusion and the direction normal to species diffusion because of heat losses in these two directions, particularly at the system (i.e. full battery) level; 2) thicknesses of the electrode and separator disks or plates are nonuniform because of manufacturing difficulties (in practice, electrodes and separators are very thin, about 250 μm).

Accurate prediction of battery performance (e.g., discharge voltage vs. time) requires proper descriptions of diffusion of charged species (driven by concentration and electrical-potential gradients), energy transport, electrochemical reactions, and thermodynamic potentials. The classical dilute-solution framework based on Fick's first law is generally valid only for non-interacting species diffusing in dilute solution and is not appropriate for describing multicomponent diffusion in concentrated solventless solutions as in thermal batteries. A concentrated solution theory was employed by Pollard and Newman (1981) to provide a framework for the description of isothermal transport processes in a mixture of two binary molten salts with a common ion. They converted the binary diffusion coefficients into three transport properties, namely an effective diffusion coefficient, an effective electrolyte conductivity, and a transference number. This approach describes the flux equations in terms of diffusion, migration, and convection. Pollard and Newman (1981) further employed this specific framework in modeling a LiAl/LiCl-KCl/FeS thermal battery cell. Bernardi and Newman (1987) extended the work of Pollard and Newman (1981) to model a LiAl/LiCl-KCl/FeS_2 thermal battery cell. Tribollet and Newman (1984) employed the Stefan-Maxwell equations in developing a model that describes the species transport in a concentrated solution. They then used the model to treat the steady state and the impedance of an electrochemical interface. We are not aware of any published work that uses the Stefan-Maxwell description of diffusion fluxes to model battery processes, although Meyers (1998) recently used such a formulation for a fuel cell.

Comprehensive thermal finite-element computer models of two thermal battery systems were developed by Dobranich (1995), and they enable the predictions of temperature distributions within individual cells. However, prior to the present work, predictive capabilities did not exist at Sandia for computing voltage-vs.-time battery performance either at the cell level or at the system level.

This report is organized as follows. In Chapter 2, the development of a GOMA-based thermal battery model and some case-study results are presented. Here, a new general framework and its implementation in GOMA for modeling multi-dimensional multicomponent transport with simultaneous electrochemical reactions in concentrated solutions are described. Verification and validation of the new GOMA-based capability developed in this project were carried out in several steps. First, the new GOMA capability for modeling multicomponent transport of neutral species was verified and validated using the model problem of ternary gaseous diffusion in a Stefan tube. Next, the new GOMA-based thermal battery computer model was verified using an ideal-

ized battery cell in which concentration gradients are absent. Lastly, the full model was verified by comparing with that of Bernardi and Newman (1987) and validated using limited thermal-battery discharge-performance data from the open literature (Dunning 1981) and from Sandia (Guidotti 1996). In Chapter 3, the development of a new Liquid Chemkin software package is described; this new capability allows the user to handle many aspects of liquid-phase kinetics, thermodynamics, and transport (particularly in terms of computing properties). In Chapter 4, the estimation of Stefan-Maxwell diffusion coefficients for liquid processes is discussed. In Chapter 5, the development of a Lattice-Boltzmann-based capability for modeling pore- or micro-scale phenomena involving convection, diffusion, and simplified chemistry is presented; the capability was demonstrated by modeling phenomena in the cathode region of a thermal battery cell. Lastly, a list of publications, technical presentations, and technical memoranda produced in this project is provided.

2. DEVELOPMENT OF A GOMA-BASED THERMAL BATTERY CELL MODEL AND COMPUTED RESULTS OF CASE STUDIES

2.1 Governing Equations, Boundary Conditions, and Numerical Solution Methods for a Thermal Battery Cell

A cutaway view of a typical thermal battery system, which normally consists of a stack of cells, is shown in Figure 2.1a. A typical cell (shown in Figure 2.1b) consists of the anode, the separator, the cathode, and the heat source, which is ignited to provide the energy for melting the solid electrolyte prior to battery discharge. In the present work we focus on predicting phenomena during battery discharge, i.e. after the solid electrolyte is completely melted. Consequently, a cell consisting of only the anode, the cathode, and the separator (as shown in Figure 2.1c) is of interest in the present work. In practice, a reservoir (thickness much smaller than the separator) is often present to allow overflow of the electrolyte melt; for simplicity it is ignored in the present work (the presence of a reservoir does not create modeling difficulty since it can be considered as part of the separator with a porosity of unity). The physical phenomena that occur in a thermal battery cell can be briefly summarized as follow: right before battery discharge is to start, the heat pellets are ignited and burned, which provides thermal energy to melt the solid electrolyte. Once the electrolyte is in molten form, battery discharge begins. During discharge, as indicated in Figure 2.1d, electrons are produced from the oxidation electrochemical reactions in the negative electrode (anode) and are consumed by the reduction reactions in the positive electrode (cathode). These electrons are conducted through the wire, which connects the thermal battery cell and the load, from the anode to the cathode. When the electrons are being conducted from the anode through the wire to the cathode, Li^+ ions are simultaneously migrating from the anode to the cathode through the electrolyte solution (Figure 2.1d).

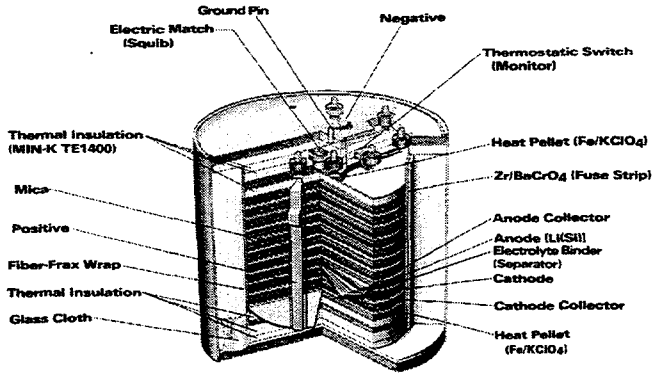

Figure 2.1a Cutaway view of a typical thermal-battery system

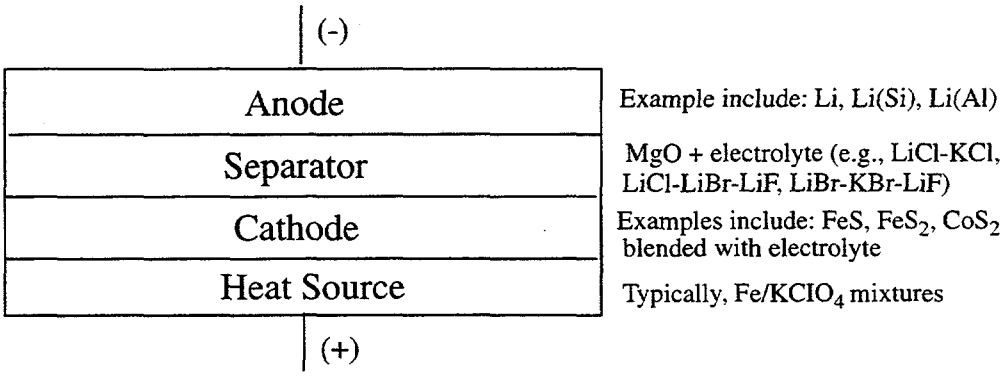

Figure 2.1b Schematics of a thermal battery cell

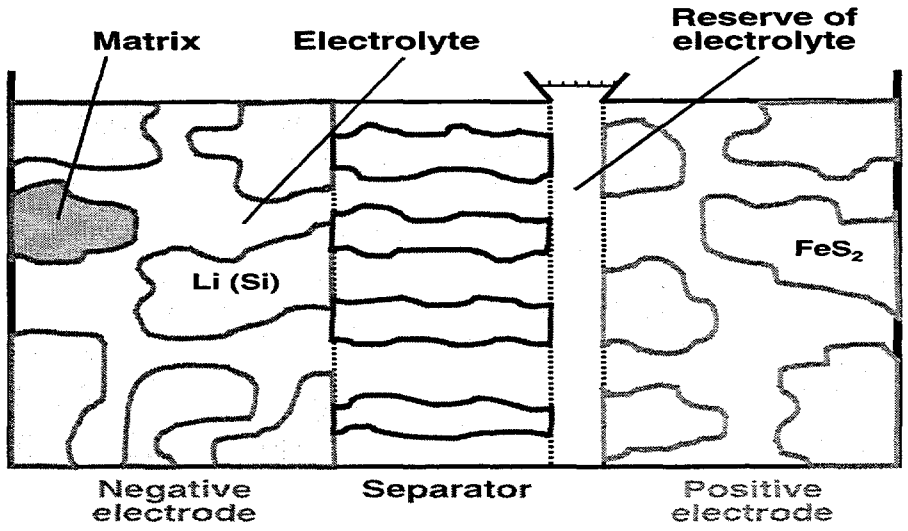

Figure 2.1c. Cross section of a thermal battery cell (excluding the heat source)

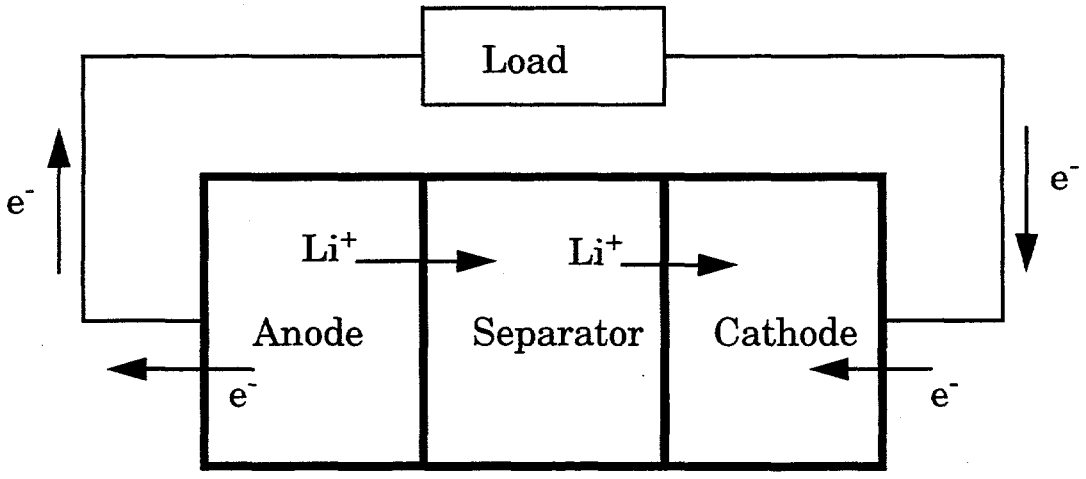

Figure 2.1d. A thermal battery cell connected with a load

The governing equations describing the phenomena in a thermal battery cell are presented below. The primary and auxiliary variables, boundary conditions for the primary variables, and initial conditions for the mole fraction of each species, porosity, and temperature are given. The present model is based on the macroscopic treatment of transport in the electrode regions developed by Newman and Tobias (1962); that is, the liquid electrolyte phase and the solid electrode phase are treated as two superposed continua. This macroscopic approach can be justified using volume averaging (see Newman and Tobias (1962) on the detailed development of the macroscopic theory of electrodes; see also Newman and Tiedemann (1975)). An m-dimensional thermal battery cell with an electrolyte consisting of n ionic species can be described by the n+5+m primary variables and (2n+2)m+n+2 auxiliary variables listed in Table 2.1.

Table 2.1. Unknowns for a Multi-dimensional Thermal-Battery Cell

Name	No. of Eq.	Type	Unknown Description	Units
x_i	n^*	primary	Mole fraction of ionic species i	
Φ_1	1	primary	Electrical potential in solid electrode	volt
Φ_2	1	primary	Electrical potential in liquid electrolyte	volt
ε	1	primary	Porosity or electrolyte volume fraction	
$\boldsymbol{u}$	m^{**}	primary	Superficial mass-average velocity	m/s
p	1	primary	Hydrodynamic pressure in electrolyte	N/m^2
T	1	primary	Cell temperature	K
$\boldsymbol{J}_i$	$n \cdot m$	auxiliary	Superficial diffusive flux of species i (wrt $\boldsymbol{u}$)	mole/m^2-s
$\nabla \mu_i$	$n \cdot m$	auxiliary	electrochemical potential gradient of species i	J/mole-m
r_i	n	auxiliary	Rate of production/consumption of species i per unit electrode volume	mole/m^3-s
i_1	m	auxiliary	Superficial current density in solid electrode	A/m^2
i_2	m	auxiliary	Superficial current density in electrolyte	A/m^2
ρ	1	auxiliary	Electrolyte density	kg/m^3
c	1	auxiliary	Total molar concentration of electrolyte	mole/m^3

* n is the total number of ionic species in the liquid electrolyte
** m is the problem dimension; e.g., m = 3 for a three-dimensional process.

2.1.1 Governing Equations

Mole Fractions of Species 1 through n-1. The principle of species mass conservation describes the mole fractions of species 1 through n-1 (n is the number of ionic species):

$$\frac{\partial}{\partial t}(\varepsilon c x_i) + \nabla \cdot (\boldsymbol{u} c x_i) + \nabla \cdot \boldsymbol{J}_i = r_i \qquad (2.1)$$

where the rate of production or consumption of species i is given by Faraday's law

combined with Butler-Volmer kinetics:

$$r_i = -\sum_j \frac{s_{ij} ai_{j,0(ref)}}{n_j F} \prod_k \left(\frac{x_{ko}}{x_{k,ref}}\right)^{\beta_{kj}} \left[e^{\frac{\alpha_{aj} F(\Phi_1 - \Phi_2 - U_{j,0})}{RT}} - e^{\frac{\alpha_{cj} F(\Phi_1 - \Phi_2 - U_{j,0})}{RT}} \right] \quad (2.2).$$

In Equation (2.1), the molar flux, $\boldsymbol{J}_i$, is given by the Stefan-Maxwell flux model:

$$\frac{x_i}{RT}\left(\nabla\mu_i + \bar{S}_i \nabla T - \frac{M_i}{\rho}\nabla p\right) = \sum_{j \neq i} \frac{x_i \boldsymbol{J}_j - x_j \boldsymbol{J}_i}{c\varepsilon D_{ij}} \quad (2.3)$$

where the gradient of the electrochemical potential, $\nabla\mu_i$, is given by

$$\nabla\mu_i = z_i F \nabla\Phi_2 + \frac{RT}{x_i}\nabla x_i + RT \sum_{l=1}^{n-2} \left(\frac{\partial \ln\gamma_i}{\partial x_l}\right)_{T,p} \nabla x_l - \bar{S}_i \nabla T + \bar{V}_i \nabla p \quad (2.4).$$

The Multi-dimensional Multi-component Molar Diffusive Flux. An equation relating the molar diffusion fluxes with respect to the mass average velocity is the constraint of zero total diffusive mass flux:

$$\sum_{i=1}^{n} M_i \boldsymbol{J}_i = 0 \quad (2.5).$$

Replacing the first equation (i.e. i = 1) in Equation (2.3) by Equation (2.5) and casting the resultant equation set in matrix-equation form give:

$$\boldsymbol{b}\boldsymbol{J} = \boldsymbol{d} \quad (2.6)$$

where $\boldsymbol{b}$ is a matrix of dimension N by N with N being the product of number of species (n) and the dimension of the problem (m), i.e. $N = n \cdot m$. Components of $\boldsymbol{J}$, $\boldsymbol{b}$, and $\boldsymbol{d}$ are:

$$d_{i_q} = 0 \qquad \text{for} \quad i_q = 1,..., m.$$

$$d_{i_q} = \frac{x_k}{RT}\left[(\nabla\mu_k)_q + \bar{S}_k(\nabla T)_q - \frac{M_k}{\rho}(\nabla p)_q\right] \qquad \text{for} \quad i_q = (k-1)m + q; \quad q = 1,..., m; \quad k = 2, 3,..., n.$$

$$b_{i_q j_q} = M_k \qquad \text{for} \quad i_q = 1,..., m; j_q = (k-1)m + q; q = 1,..., m; k = 1, 2,..., n.$$

$$b_{i_q j_q} = 0 \qquad \text{for} \quad i_q = 1,..., m; j_q = 1,..., N \text{ but } j_q \neq (k-1)m + q; \quad q = 1,..., m; \quad k = 1, 2,..., n.$$

$$b_{i_q j_q} = \frac{x_k}{c\varepsilon D_{kl}} \qquad \text{for} \quad i_q = (k-1)m + q;\ j_q = (l-1)m + q;\ \ j_q \neq i_q;$$
$$k = 2, 3, \ldots, n; \qquad l = 1, 2, \ldots, n;\ l \neq k.$$

$$b_{i_q i_q} = -\sum_{l \neq k}^{n} \frac{x_l}{c\varepsilon D_{kl}} \qquad \text{for} \quad i_q = (k-1)m + q;\ q = 1, \ldots, m;\ k = 2, 3, \ldots, n.$$

Mole Fraction of Species *n*. Consistency condition dictates the mole fraction of species n:

$$\sum_{i=1}^{n} x_i = 1 \tag{2.7}$$

Electrical Potential in Solid Electrode. The principle of charge conservation between the liquid electrolyte phase and the solid electrode phase can be used to describe the electrical potential in the solid electrode:

$$\nabla \cdot \boldsymbol{i}_2 = -\nabla \cdot \boldsymbol{i}_1 = F \sum_{i=1}^{n} z_i r_i \tag{2.8}$$

Superficial Current Density in Solid Electrode. Ohm's law governs the superficial current density in the solid electrode:

$$\boldsymbol{i}_1 = -\sigma \nabla \Phi_1 \tag{2.9}$$

Substituting Equation (2.9) into Equation (2.8) yields a Poisson equation that governs the electrical potential in the solid electrode:

$$\nabla \cdot (-\sigma \nabla \Phi_1) = -F \sum_{i=1}^{n} z_i r_i \tag{2.10}$$

Electrical Potential in Liquid Electrolyte. The constraint of electroneutrality, which is assumed to be satisfied everywhere within the liquid electrolyte phase, provides an equation for the solution of the electrical potential in the liquid electrolyte:

$$\sum_{i=1}^{n} z_i x_i = 0 \tag{2.11}$$

Equation (2.11) is an algebraic constraint, which, though simple, is not convenient to use since it destroys the banded structure of the matrix that results from the finite-element formulation of the governing partial differential equations (the direct use of Equation (2.11) reduces the computational efficiency that can otherwise be achieved from exploiting the banded structure in

the resultant matrix equations). This issue is not unique to the finite element formulation of the governing equations; the same reduction in computational efficiency also arises when solving the governing equations using finite difference methods. A preferred equation for the electrical potential Φ_2 in the liquid electrolyte is one in which Φ_2 appears explicitly, thus preserving the banded matrix structure and ensuring the non-zero diagonal entry. Multiplying Equation (2.1) by z_iF (the product of charge number of species i and the Faraday constant), summing the resultant equation from $i = 1$ to $i = n$ and applying the electroneutrality constraint, Equation (2.11), yields:

$$\nabla \cdot \sum_{i=1}^{n} F z_i \boldsymbol{J}_i = F \sum_{i=1}^{n} z_i r_i \tag{2.12}$$

Solving Equation (2.6) for $\boldsymbol{J}_i$ and substituting into Equation (2.12) gives:

$$\nabla \cdot (-\kappa \nabla \Phi_2) = F \sum_{i'=1}^{n} z_{i'} r_{i'} - \nabla \cdot \sum_{i=1}^{N} \sum_{k=m+1}^{N} F z_{i'} b_{ik}^{-1} \nabla x_{k'} -$$

$$\nabla \cdot \sum_{i=1}^{N} \sum_{k=m+1}^{N} F z_{i'} b_{ik}^{-1} x_{k'} \sum_{l'=1}^{n-2} \left(\frac{\partial}{\partial x_{l'}} \ln \gamma_{l'} \right)_{T,p} \nabla x_l \tag{2.13}$$

where b_{ik}^{-1} are the components of the inverse of $\mathbf{b}$ and κ is given by:

$$\kappa = \frac{F^2}{RT} \sum_{i=1}^{N} \sum_{k=m+1}^{N} z_{i'} z_{k'} (-b_{ik}^{-1}) x_{k'} \quad \left(\text{where } i' = \frac{i-1}{m} + 1 \text{ and } k' = \frac{k-1}{m} + 1\right) \tag{2.14}$$

Equation (2.13) is a Poisson equation similar to Equation (2.10) with a variable electrical conductivity that implicitly depends on time and position via the mole fractions and their gradients; also there are two additional source-term contributions in Equation (2.13) accounting for effects of concentration gradients and nonideal behavior.

Superficial Current Density in Liquid Electrolyte. The current density in the electrolyte is the result of transport of all the charged species; consequently,

$$\boldsymbol{i}_2 = F \sum_{i=1}^{n} z_i \boldsymbol{J}_i \tag{2.15}$$

Porosity or Electrolyte Volume Fraction. An overall electrode material balance provides an equation for the determination of porosity (cf. Pollard and Newman 1981):

$$\frac{\partial \varepsilon}{\partial t} = \sum_j \sum_{solid} \frac{\overline{V}_i s_{ij}}{n_j F} a i_{j0,ref} \prod_k \left(\frac{x_{ko}}{x_{k,ref}}\right)^{\beta_{kj}} \left[e^{\frac{\alpha_{aj} F(\Phi_1 - \Phi_2 - U_{j,0})}{RT}} - e^{\frac{\alpha_{cj} F(\Phi_1 - \Phi_2 - U_{j,0})}{RT}} \right] \quad (2.16).$$

Superficial Mass-average Velocity. When so desired, the Brinkman equation for fluid flow through a porous medium can be used to determine the superficial mass-average velocity (cf. Gartling et al. 1996):

$$\frac{\partial}{\partial t}\left(\frac{\rho}{\varepsilon}\boldsymbol{u}\right) + \frac{1}{\varepsilon^2}\boldsymbol{u}\cdot\nabla\boldsymbol{u} = -\nabla p + \mu_B \nabla^2 \boldsymbol{u} - \left(\frac{\rho \hat{c}}{\sqrt{k}}\|\boldsymbol{u}\| + \frac{\mu}{k}\right)\boldsymbol{u} \quad (2.17)$$

where μ is the liquid-electrolyte viscosity, and μ_B the Brinkman viscosity. It should be noted that the convective flux contribution to the total flux is insignificant as compared to the diffusive flux contribution in thermal battery processes involving molten-salt electrolytes; convective flow is included here for completeness and to ensure that the accuracy of the electrolyte material balance is maintained (cf. Pollard and Newman 1981).

Hydrodynamic Pressure in Liquid Electrolyte. An overall mass balance on the electrolyte yields an equation that can be used to solve for hydrodynamic pressure in the electrolyte:

$$\frac{\partial}{\partial t}(\varepsilon\rho) + \nabla\cdot\rho u = \sum_{i=1}^{n} M_i r_i \quad (2.18).$$

Temperature in Liquid Electrolyte. The first law of thermodynamics is used to determine the temperature distribution in the liquid electrolyte (cf. Bird et al. 1960):

$$\rho c_p \frac{DT}{Dt} = \nabla\cdot k_T \nabla T + Q \quad (2.19)$$

where the source term, Q, refers mainly to the Joule heating effect although it can include other effects such as viscous dissipation and heat generation from electrolyte solidification. Equation (2.19) describes multi-dimensional heat transfer that occurs in both the ionic transport direction and the direction normal to ionic transport; it can also capture the effects due to nonuniformity of electrode and separator thicknesses. If temperature gradients in the electrolyte are negligible (e.g., if we have a single-cell battery and the electrodes and separator are sufficiently thin), a lumped energy transport model that accounts for Joule heating and heat loss from the cell at the cell/air interfaces, as put forth by Pollard and Newman (1981), can be used:

$$\frac{mc_p}{2A}\frac{dT}{dt} = \left(U_o - V - T_o\frac{\partial U_o}{\partial T}\right)I - h(T - T_a) \qquad (2.20).$$

Density of Liquid Electrolyte. An equation of state is required to relate the electrolyte density to field variables such as species mole fractions, temperature, and pressure. For the LiCl-KCl electrolyte system, an empirical correlation is available (Pollard and Newman 1981):

$$\rho = 1.735 - 0.3x_{Li^+} \qquad (2.21).$$

Total Molar Concentration of Electrolyte. From the definition of total molar concentration of an n component mixture,

$$c = \rho\left(\sum_{i=1}^{n} M_i x_i\right)^{-1} \qquad (2.22).$$

Stefan-Maxwell Diffusivities. The solution of Equation (2.6) requires values of the Stefan-Maxwell diffusion coefficients, D_{ij}. In a mixture of n ionic species the quantities typically measured are: an effective electrical conductivity κ^e, (n-2) independent transference numbers t_i^c and (n-1)(n-2)/2 effective diffusion coefficients D_k^e as well as mean electrolyte activity coefficients $\gamma_{\pm k}$ for neutral combinations. The D_{ij} values can be determined from these measured quantities. For example, for an electrolyte mixture consisting of two salt species A and B decomposing into ions 1, 2, and a common ion 3, Larson (1998) inverted the equation of Pollard and Newman (1979) to obtain:

$$D_{12}^{-1} = D_{21}^{-1} = \frac{-z_1 z_2 c F^2}{RT\kappa^e} + \frac{t_1^c t_2^c c x_3^2\left(\nu_1^A + \dfrac{d\ln\gamma_A}{d\ln x_A}\right)}{x_1 x_2 \nu_3^A \nu_3^B D^e (c_A + c_B)} \qquad (2.23),$$

$$D_{13}^{-1} = D_{31}^{-1} = \frac{-z_1 z_3 c F^2}{RT\kappa^e} - \frac{t_2^c c x_3\left(\nu_1^A + \dfrac{d\ln\gamma_A}{d\ln x_A}\right)}{x_1 \nu_3^A \nu_3^B D^e (c_A + c_B)}\left(1 + \frac{z_3 x_3}{z_2 x_2} t_2^c\right) \qquad (2.24),$$

$$D_{23}^{-1} = D_{32}^{-1} = \frac{-z_2 z_3 c F^2}{RT\kappa^e} - \frac{t_1^c c x_3\left(\nu_1^A + \dfrac{d\ln\gamma_A}{d\ln x_A}\right)}{x_2 \nu_3^A \nu_3^B D^e (c_A + c_B)}\left(1 + \frac{z_3 x_3}{z_1 x_1} t_1^c\right) \qquad (2.25).$$

An alternative method of determining D_{ij} is performing molecular dynamics simulations. Chapter 4 presents a systematic study on the estimation of Stefan-Maxwell diffusion coefficients for liquid processes.

Electrochemical Reactions and Thermodynamic Open-circuit Potential in the Electrode Regions. The governing equations presented above, Equations (2.1 - 2.20) and (2.22), are generic in that they are valid or applicable in all thermal battery processes. Thermal battery systems differ mainly due to: 1) the chemical make-up and compositions of the electrodes and electrolytes employed, which control the electrochemical reactions and thermodynamic open-circuit potentials involved; 2) the geometry of the electrodes, the separator, and the heat source layer; 3) thermal insulation on the outer surface of the thermal battery system. The electrochemical reactions not only affect the species mass balances via the species production/consumption rates (thus the electron flux or current density output by the battery cell) but also determine the thermodynamic open-circuit potentials (thus the battery-cell voltage). In this sub-section, we discuss the electrochemical reactions and the associated thermodynamic open-circuit potentials in a Li(Si)/LiCl-KCl/FeS_2 thermal battery cell in which the anode is made of Li(Si), the cathode FeS_2, and the electrolyte LiCl-KCl mixture. The predecessor of the Li(Si)/LiCl-KCl/FeS_2 cell is the LiAl/LiCl-KCl/FeS cell that was developed more than twenty years ago (see, e.g., Nelson et al. 1979, Gay et al. 1985) and its popularity was due to the fact that an inexpensive current collector (iron) can be used in the FeS electrode. The Li(Si)/LiCl-KCl/FeS_2 system is a more recent development that offers higher cell voltage, which makes it possible to reduce the number of cells per battery or to increase the maximum power achievable relative to the LiAl/LiCl-KCl/FeS cell (cf. Bernardi 1986). As discussed by Guidotti (1995), the Li(Si)/LiCl-KCl/FeS_2 system and its variants (mainly in electrolyte make-up and compositions) are of key interest to Sandia National Laboratories. The electrolyte systems other than LiCl-KCl that have been studied at Sandia and the Argonne National Laboratory include (see, e.g., Guidotti 1995): CsBr-LiBr-KBr, LiBr-KBr-LiF, LiCl-LiBr-KBr, LiCl-LiBr-LiF, which all involve four charged species.

The discharge process in the anode can be described by the following oxidation electrochemical reactions, which are based on the phase composition given by Wen and Huggins (1981) (Bernardi 1986, Bernardi and Newman 1987):

$$\begin{aligned} &\text{I.} && Li_{3.25}Si \rightarrow Li_{2.33}Si + 0.92Li^+ + 0.92e^- \\ &\text{II.} && Li_{2.33}Si \rightarrow Li_{1.71}Si + 0.62Li^+ + 0.62e^- \\ &\text{III.} && Li_{1.71}Si \rightarrow Si + 1.71Li^+ + 1.71e^-. \end{aligned} \qquad (2.26).$$

The thermodynamic open-circuit potentials, relative to LiAl, corresponding to these electrochemical reactions in the anode are (Bernardi 1986, Bernardi and Newman 1987):

$$U_{I,o} = -0.187529 + 0.0000731T$$

$$U_{II,o} = -0.088097 + 0.0001122T \tag{2.27}$$

$$U_{III,o} = -0.0345 + 0.0001056T$$

where the $U_{j,o}$ have a unit of volts and T has a unit of K or Kelvin.

The discharge process in the cathode is much more complex and not yet well understood. The reduction electrochemical reactions in the cathode at 450°C are (Tomczuk et al. 1982, Bernardi 1986, Bernardi and Newman 1987):

a. $2FeS_2 + 3Li^+ + 3e^- \rightarrow Li_3Fe_2S_4$

b. $Li_3Fe_2S_4 + 0.47Li^+ + 0.47e^- \rightarrow 1.58Li_{2.2}Fe_{0.8}S_2 + 0.84Fe_{0.875}S$ (2.28)

c. $Fe_{1-x'}S$ and $Li_{2+x}Fe_{1-x}S_2$ produce Li_2FeS_2

d. $Li_2FeS_2 + 2Li^+ + 2e^- \rightarrow 2\,Li_2S + Fe$

where x and x' are compositional variables ranging from 0.2 to 0 and 0.125 to 0, respectively.

The open-circuit potentials corresponding to these electrochemical reactions in the cathode are (Bernardi 1986, Bernardi and Newman 1987):

$$U_{a,o} = 1.4251 + 0.0004785T$$

$$U_{b,o} = 1.208771 + 0.00065142T \tag{2.29}$$

$$U_{c,o} = U_{b,o} + \frac{0.130129 - 0.00063812T}{1 - [2.2(4x'_o - 2)/(2x'_o - 0.8) - 3]}\left(\frac{q_c 2\tilde{V}_{FeS_2}}{\varepsilon^o_{FeS_2} F}\right)$$

$$U_{d,o} = 1.43211 - 0.000147T$$

where the $U_{j,o}$, are given relative to a two-phase (α-β) LiAl-alloy reference electrode (as in Equation 2.27, the $U_{j,o}$ here also have a unit of volts and T has a unit of K or kelvin); q_c is state-of-discharge (the number of coulombs of charge passed for reaction c per unit volume of the electrode); $\tilde{V}_{FeS_2}$ is the molar volume of FeS_2; $\varepsilon^o_{FeS_2}$ is the initial volume fraction of FeS_2 in the cathode; and x'_o, is a compositional variable given by (Bernardi 1986, Bernardi and Newman 1987):

$$x'_o = 0.91658 - 9.240\times10^{-5}(T - 273.15) \tag{2.30}$$

with T having a unit of K. Specifically, x'_o is defined in such a way that the second product of Reaction b has the temperature-dependent composition $Fe_{x'_0}S$. It can then be shown that the quantity in square brackets in Equation (2.29) is proportional to the electrode utilization during the Reaction b step. In equation (2.29) the term inside the big brackets in the equation for $U_{c,0}$ is a function of fractional utilization of the starting cathode material (FeS_2), f_{FeS_2}, and is given by

$$\frac{q_c 2\tilde{V}_{FeS_2}}{\varepsilon^o_{FeS_2} F} = \frac{(f_{FeS_2} - f_{FeS_2,b})}{(f_{FeS_2,c} - f_{FeS_2,b})} n_c \tag{2.31}$$

where $f_{FeS_2,b}$ and $f_{FeS_2,c}$ are the fractional utilization of the starting cathode material (FeS_2) evaluated at the end of Reactions b and c, respectively; and n_c is the number of electrons consumed per mole of FeS_2 in Reaction c. Specifically, $f_{FeS_2,b} = 0.434$ and $f_{FeS_2,c} = 0.5$, $n_c = 0.53$, and f_{FeS_2} is related to discharge time and current density by (Bernardi and Newman 1987):

$$f_{FeS_2} = \frac{It\tilde{V}_{FeS_2}}{4L_c\varepsilon^o_{FeS_2}F} \tag{2.32}.$$

Similarly, a fractional utilization of the starting anode material ($Li_{3.25}Si$) is defined as

$$f_{Li_{3.25}Si} = \frac{It\tilde{V}_{Li_{3.25}Si}}{3.25L_a\varepsilon^o_{Li_{3.25}Si}F} \tag{2.33}.$$

Clearly, in Equation (2.29) the open-circuit potentials, $U_{j,o}$, in regions a, b, and d depend on temperature only whereas that in region c depends on temperature as well as linearly on utilization of the electrode material.

Interfacial Area and Exchange Current Density for the Cathode. According to Paxton and Newman (1997), the effective interfacial area per unit electrode volume, a, in a porous electrode containing spherical particles is proportional to the volume fraction of active material. Thus, it can be expected to vary linearly with the fractional utilization of electrode material, f. For step a (or Reaction a region) in the discharge of the FeS_2 electrode, the active material is exhausted when $f_{FeS_2} = 0.375$. So

$$a = a_0\left(1 - \frac{f_{FeS_2}}{0.375}\right) \tag{2.34}.$$

As for the exchange current density, it should have an Arrhenius temperature dependence, so

$$i_0 = i_{0,0} e^{-\frac{E}{R}\left(\frac{1}{T}-\frac{1}{T_0}\right)} \tag{2.35}$$

where E is the activation energy. Combining Equations (2.34) and (2.35) yields a model for the product of interfacial area per unit electrode volume by exchange current density, which is a function of the fractional utilization and cell or electrolyte temperature:

$$ai_0 = a_0 i_{0,0}\left(1-\frac{f_{FeS_2}}{0.375}\right)e^{-\frac{E}{R}\left(\frac{1}{T}-\frac{1}{T_0}\right)} \quad (\text{where } 0 \le f_{FeS_2} \le 0.375) \tag{2.36}.$$

In Equation (2.36) both f_{FeS_2} and T are computed as functions of time during the battery simulation. If the current density is constant, then f_{FeS_2} is proportional to t, and if the lumped-parameter energy equation is used, then T will decay exponentially with t. In any case, the product ai_0 will generally decrease over time, leading to a decline in the cell voltage. Equations similar to Equation (2.36) can be developed for Reaction b, c and d regions in the cathode and for the anode.

2.1.2 Boundary and Initial Conditions

Boundary conditions for Equations (2.1), (2.8), (2.10), (2.13), (2.17), and (2.19) are as follow. At the electrode current collectors and the cell/environment or cell/air interfaces,

$$\nabla x_i = 0 \tag{2.37},$$

$$\nabla \Phi_2 = 0 \tag{2.38},$$

$$\boldsymbol{u} = 0 \tag{2.39}.$$

At the anodic current collector,

$$\Phi_1 = 0 \quad \text{and} \quad i_2 = 0 \tag{2.40}.$$

At the cathodic current collector,

$$\Phi_1 = V \quad \text{and} \quad i_2 = 0 \tag{2.41}.$$

At the anode/separator and separator/cathode interfaces,

$$i_1 = 0 \tag{2.42}$$

At the cell/environment interfaces, when the full energy transport model (Equation 2.19) is employed:

$$-k_T \nabla T \cdot \boldsymbol{n} = h(T - T_a) \tag{2.43}$$

When the lumped energy transport model (Equation 2.20) is used, no boundary condition is needed.

Lastly, initial values of species mole fractions, porosity, temperature, and velocities are specified:

$$x_i = x_i^0, \qquad \varepsilon = \varepsilon^0, \qquad T = T^0, \quad \text{and} \quad \boldsymbol{u} = \boldsymbol{u}^0 \tag{2.44}$$

2.1.3 Numerical Solution Methods

Constant total cell voltage with variable current density. In this case the solution process is straightforward since all the boundary conditions are known a priori. We employed GOMA (Schunk et al. 1998), a multidimensional multi-physics finite-element code developed and being enhanced at Sandia National Laboratories, as the basic platform for solving the set of highly nonlinear and coupled partial differential equations as described in Section 2.1.1. GOMA provides an efficient framework of finite-element analysis and fully coupled implicit solution scheme via Newton's method. GOMA also provides a second-order accurate predictor-corrector time integration scheme with adaptive control of the time step in solving transient problems. Readers who are interested in the details of numerical solution methods in GOMA are referred to the GOMA manual (Schunk et al. 1998). In the present work the new multidimensional Stefan-Maxwell model as described in Equation (2.6) was implemented in GOMA. The species mass-balance equation in GOMA was modified to include the effect of porosity variation and to incorporate Butler-Volmer kinetics, accounting for the production/consumption of species from electrochemical reactions in the anode and cathode regions. The voltage equation (in GOMA prior to this work) was modified to incorporate the variable electrical conductivity as described in Equation (2.14) and the various source terms as given on the right hand-side of Equation (2.13). The thermal transport (or temperature) equation (also in GOMA prior to this work) was modified and used to solve Equation (2.10) for the electrical potential in the solid electrode. Lastly, Equation (2.20) was integrated explicitly to obtain electrolyte temperature; similarly, Equation (2.16) was integrated explicitly to yield porosity.

Time-dependent total cell voltage with constant current density. This is how thermal batteries

operate in practice and thus is of importance to thermal battery designers at Sandia. In this case an iteration on total cell voltage is required since the boundary condition for the electrical potential in the electrode at the cathodic current collector is not known a priori; instead, its value is dictated by the constant current density in the separator (in the separator, all the current density is carried by the electrolyte phase). To predict the total cell voltage as a function of time in this case, a driver routine that wraps around GOMA was written. The driver routine, which is essentially a root-finding program based on a secant method, searches for the voltage at each time step required to keep the current density constant during a transient simulation. Figure 2.2 shows a diagram (or flow chart) of the driver-routine operation. A battery-cell simulation is initiated by specifying the desired constant current density and picking two values of the total cell voltage that are expected to bound the voltage. The driver routine picks an initial value of the total cell voltage and performs a GOMA run (in which total cell voltage is specified as the boundary condition for Φ_1 at the cathodic current collector) for a specified time step. At the end of the time step the current density (sampled at the center of the separator) computed by GOMA is compared against the desired value. If the computed current density is within a pre-specified tolerance of the desired current density then the driver routine proceeds to the next time step. If the computed current density from the simulation is not within the pre-specified tolerance then a secant method is used to adjust the value of the battery voltage and the GOMA run for the time step is repeated. A given time step may be repeated several times until the computed current density and desired current density agree to within the specified tolerance.

Adjustment to the total cell voltage at a time step is made with a secant method. The secant method is based on a modification of the formula for Newton's method given by

$$x_{i+1} = x_i - \frac{f(x_i)}{f'(x_i)} \tag{2.45}$$

For the secant method f'(x) in Newton's formula is approximated by the formula

$$f'(x_i) \cong \frac{f(x_i) - f(x_{i-1})}{x_i - x_{i-1}} \tag{2.46}$$

Substituting Equation (2.46) into Equation (2.45) yields the following formula for the secant method (cf. Dahlquist and Bjorck 1974)

$$x_{i+1} = \frac{x_{i-1} f(x_i) - x_i f(x_{i-1})}{f(x_i) - f(x_{i-1})} \tag{2.47}$$

Figure 2.3 shows a schematic of the convergence process for the secant method.

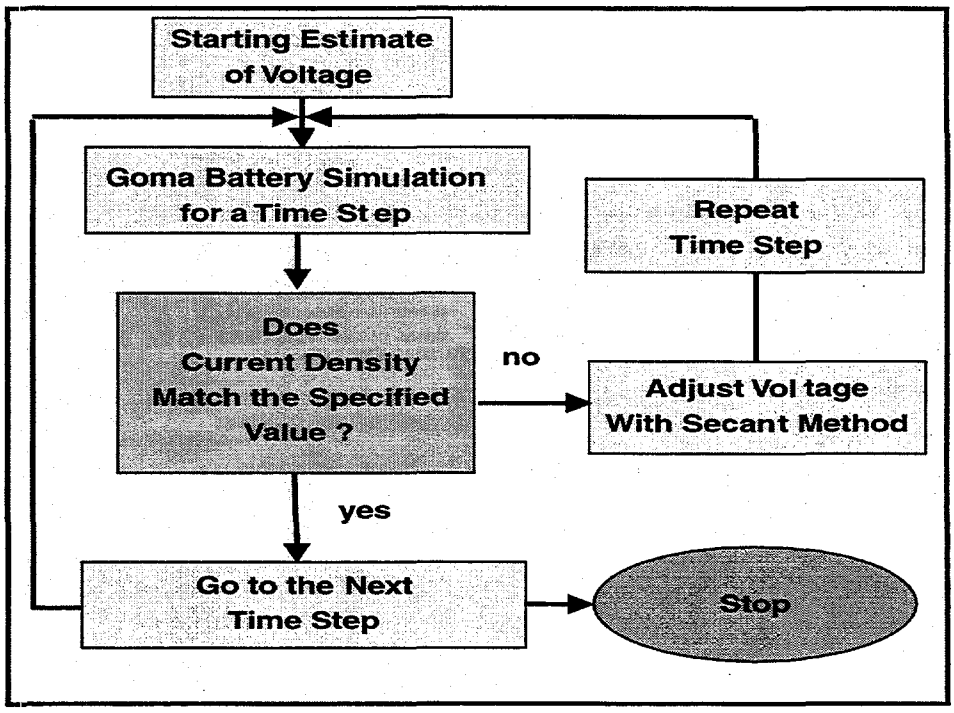

Figure 2.2. Diagram of driver routine for voltage iteration with constant current density.

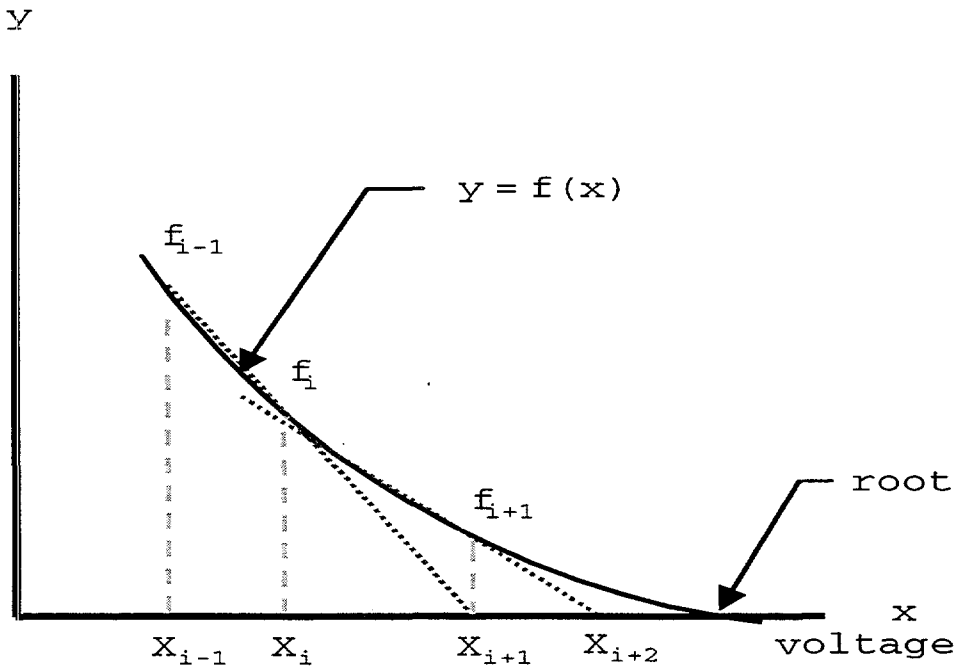

Figure 2.3. Schematic of convergence for the secant method.

2.2 Verification and Validation of the Stefan-Maxwell Flux Model in GOMA: Ternary Gaseous Diffusion in A Stefan Tube

In this section, we report on a verification and validation study of the multidimensional Stefan-Maxwell model implemented in GOMA in this project. The ternary gaseous diffusion in a Stefan tube is an ideal test problem for the Stefan-Maxwell flux model because of the availability of a closed-form analytical solution and experimental data for concentration profiles along the axis of the tube; ternary diffusion in a Stefan tube has become a classical test problem for the Stefan-Maxwell flux model (see, e.g., Duncan and Toor 1962, Getzinger and Wilke 1967, Carty and Schrodt 1975, Taylor and Krishna 1993). The present study focuses on the verification and validation of species concentration profiles along the tube as predicted by the Stefan-Maxwell flux model in GOMA.

The Problem. Figure 2.4 shows a schematic diagram of ternary gaseous diffusion in a Stefan tube. The three neutral species, acetone (species 1), methanol (species 2), and air (species 3), which form a vapor mixture, diffuse within the Stefan tube; acetone and methanol diffuse upward while air diffuses downward. The length of the tube (or diffusion path) was 23.8 cm. Pressure and temperature of the vapor mixture were maintained at 99.4 kPa and 328.5 K, respectively. At the inlet (bottom), mole fractions of each species were kept, respectively, at: $x_1 = 0.319$, $x_2 = 0.528$, and $x_3 = 0.153$; at the outlet (top), only pure air was present: $x_1 = 0$, $x_2 = 0$, and $x_3 = 1$. When the process is maintained at steady state, which is what we consider here, the total flux (diffusive and convective; averaged across the tube) of each species is uniform along the tube. It should be noted here that the convective flux of each species is a result of diffusion; that is, we have diffusion-induced convection. For the conditions as stated above, Taylor and Krishna (1993) reported the following exact values of total fluxes of acetone and methanol (which they calculated numerically using a fourth-order Runge-Kutta method): $N_1 = 1.783\text{x}10^{-7}$ mole/(cm^2 s), $N_2 = 3.127\text{x}10^{-7}$ mole/(cm^2 s), which are in excellent agreement with the following values determined experimentally by Carty and Schrodt (1975): $N_1 = 1.779\text{x}10^{-7}$ mole/(cm^2 s), $N_2 = 3.121\text{x}10^{-7}$ mole/(cm^2 s). The total flux of air was kept at zero: $N_3 = 0$.

Analytical Solution. The Stefan-Maxwell flux equations for an ideal ternary mixture of neutral species, when written in terms of the total fluxes N_i and with concentration gradients as the only driving force, are

$$\nabla x_i = \sum_{j=1}^{3} \frac{x_i N_j - x_j N_i}{c D_{ij}} \qquad (2.48),$$

where x_i is the mole fraction of species i, c the total molar concentration of the mixture, and D_{ij} the Stefan-Maxwell diffusion coefficients. As shown by Evans (1999), in 1-D approximation, Equation (2.48) can be integrated analytically to arrive at closed form solutions for x_1, x_2, and x_3, respectively:

$$x_1 = \frac{N_1}{N_1+N_2} + \frac{N_1(D_{12}-D_{13})}{D_{13}(N_1+N_2)-\frac{D_{12}}{D_{23}}(D_{23}N_1+D_{13}N_2)}x_3 - \left[\frac{N_1}{N_1+N_2} + \frac{N_1(D_{12}-D_{13})}{D_{13}(N_1+N_2)-\frac{D_{12}}{D_{23}}(D_{23}N_1+D_{13}N_2)}\right] e^{\left(\frac{N_1+N_2}{cD_{12}}\right)(z-L)} \quad (2.49)$$

$$x_3 = x_3\big|_{z=0}\, e^{\frac{1}{c}\left(\frac{N_1}{D_{13}}+\frac{N_2}{D_{23}}\right)z} \quad (2.50),$$

$$x_2 = 1 - x_1 - x_3 \quad (2.51)$$

where L is the length of the tube and equal to 23.8 cm, z the coordinate along tube, $x_3\big|_{z=0}$ the mole fraction of species 3 (air) at the inlet ($z = 0$) and equal to 0.153. At constant temperature and pressure the total molar concentration, c, and the binary diffusion coefficients, D_{ij}, are constant. For P= 99.4 kPa and T = 328.5 K, using ideal gas law we have $c = \frac{P}{RT} = 3.64\text{x}10^{-5}$ mole/cm^3. Values of D_{12}, D_{13}, and D_{23} have been reported by Carty and Schrodt (1975) (these D_{ij} values were determined from their experiment): $D_{12} = 0.0848$ cm^2/s, $D_{13} = 0.1372$ cm^2/s, and $D_{23} = 0.1991$ cm^2/s. We applied the boundary conditions at the inlet and the outlet in Equations (2.49) and (2.50) to yield a pair of nonlinear algebraic equations in terms of N_1 and N_2, which were solved numerically to give: $N_1 = 1.7834\text{x}10^{-7}$ mole/(cm^2 s) and $N_2 = 3.1274\text{x}10^{-7}$ mole/(cm^2 s). Our computed values of N_1 and N_2 are in excellent agreement with those calculated by Taylor and Krishna (1993) and those experimentally determined by Carty and Schrodt (1975).

GOMA Model. To compute species mole fractions using GOMA in this problem, in Equation (2.1) porosity is set to unity and the mass (or transient) and source terms are set to zero to yield

$$\nabla \cdot (\boldsymbol{u} c x_i) + \nabla \cdot \boldsymbol{J}_i = 0 \qquad \text{for } i = 1, 2; \quad (2.52)$$

and

$$x_3 = 1 - x_1 - x_2 \quad (2.53).$$

In Equation (2.52) the diffusive flux, $\boldsymbol{J}_i$, is given by the Stefan-Maxwell equations

$$\nabla x_i = \sum_{j=1}^{3} \frac{x_i \boldsymbol{J}_j - x_j \boldsymbol{J}_i}{c D_{ij}} \qquad \text{for i =2, 3;} \qquad (2.54)$$

which is a simplified version of Equation (2.3); specifically, concentration gradient is the only driving force for diffusion, the mixture is ideal, and porosity is set to unity. Equation (2.54) is coupled with Equation (2.5) (the constraint of zero total diffusive mass flux) to give rise to a matrix equation like Equation (2.6) that is solved to yield $\boldsymbol{J}_1$, $\boldsymbol{J}_2$, and $\boldsymbol{J}_3$. In Equation (2.52) the velocity field, $\boldsymbol{u}$, can be described by the Navier-Stokes equation at steady state,

$$\rho \boldsymbol{u} \cdot \nabla \boldsymbol{u} = -\nabla p + \mu \nabla^2 \boldsymbol{u} + \rho \boldsymbol{g} \qquad (2.55)$$

where the gauge hydrodynamic pressure, p, is given by the continuity equation of the mixture at steady state,

$$\nabla \cdot \rho \boldsymbol{u} = 0 \qquad (2.56)$$

and the density of the mixture in Equations (2.55) and (2.56) is taken to obey the ideal-gas law,

$$\rho = \frac{(P+p)}{RT} \sum_{i=1}^{3} M_i x_i \approx \frac{P}{RT} \sum_{i=1}^{3} M_i x_i = c \sum_{i=1}^{3} M_i x_i \qquad (2.57).$$

In Equation (2.57) P is the reference or base pressure of the mixture (= 99.4 kPa in our problem here), which is orders of magnitude larger than the gauge hydrodynamic pressure, p (i.e., $P \gg p$).

The boundary conditions for x_i are as shown in Figure 2.4: $x_1 = 0.319$, $x_2 = 0.528$, and $x_3 = 0.153$ at the inlet, and $x_1 = 0$, $x_2 = 0$, and $x_3 = 1$ at the outlet. As for velocity boundary conditions, perfect slip is assumed along the tube walls (in order to approximate 1-D flow); that is, velocity gradients are set to zero along tube walls. To obtain the velocity component in the axial direction, u_z, at the inlet and outlet planes (velocity profiles are taken to be flat at both the inlet and the outlet planes), we have from the definition of mass-average velocity and the relation between mass and molar fluxes:

$$u_z = \frac{1}{\rho} \sum_{i=1}^{3} M_i N_i = \frac{RT}{P} \frac{\sum_{i=1}^{3} M_i N_i}{\sum_{i=1}^{3} M_i x_i} = \frac{1}{c} \frac{\sum_{i=1}^{3} M_i N_i}{\sum_{i=1}^{3} M_i x_i} \qquad (2.58).$$

Accordingly, at the inlet plane $u_z = 0.014$ cm/s and at the outlet plane $u_z = 0.019$ cm/s using values of $N_1 = 1.7834 \times 10^{-7}$ mole/(cm^2 s) and $N_2 = 3.1274 \times 10^{-7}$ mole/(cm^2 s). To be consistent with the analytical solution, we have $u_r = 0$ (i.e. the r-component velocity vanishes) at both the inlet and the outlet planes.

In summary Equations (2.52), (2.55) - (2.56) (along with Equations 2.53, 2.54, 2.5, and 2.57 and the boundary conditions as discussed above) are solved simultaneously (i.e., in a fully coupled fashion) in GOMA to yield the species mole fractions, x_1, x_2, and x_3.

Results - Comparisons of GOMA Predictions with Analytical Solution and Experimental Data. Figure 2.5 shows a comparison of species mole fractions between the computed GOMA prediction and the analytical solution whereas Figure 2.6 presents a comparison between GOMA prediction and the experimental data of Carty and Schrodt (1975). Excellent agreement is seen in both verification (GOMA vs. exact solution) and validation (GOMA vs. experimental data).

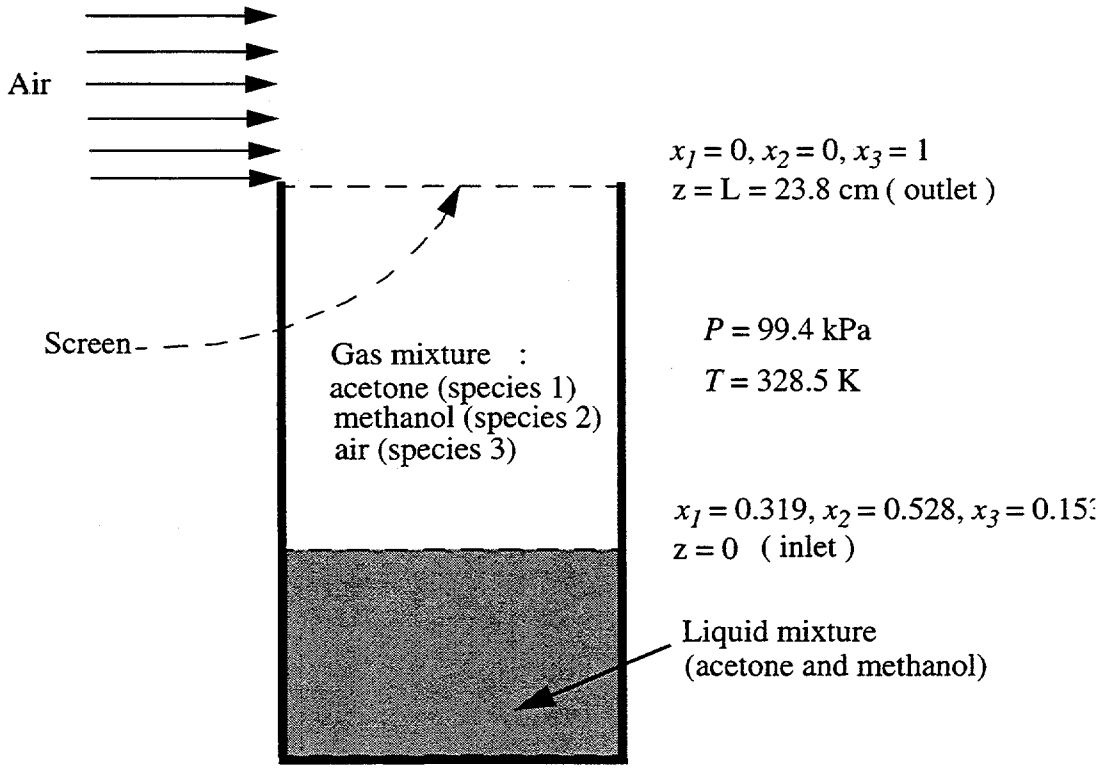

Figure 2.4 Schematic diagram of ternary gaseous diffusion in a Stefan tube (Taylor and Krishna 1993)

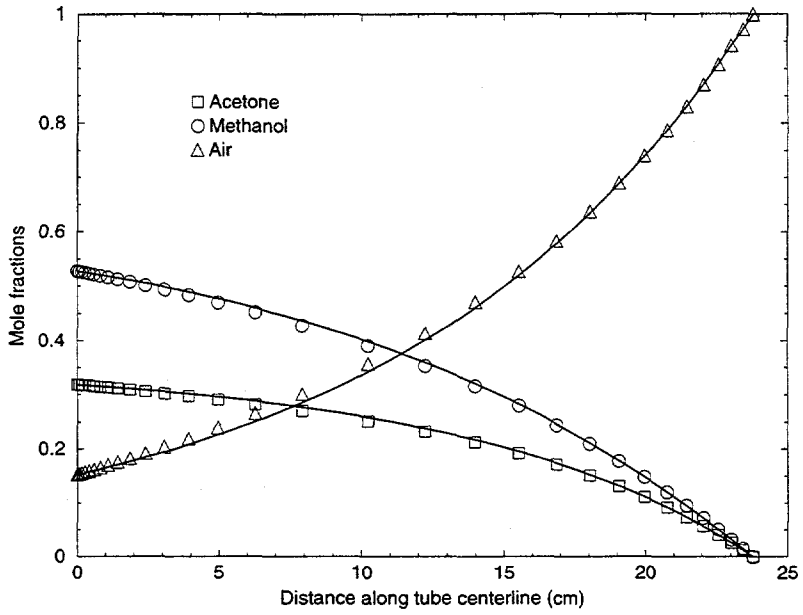

Figure 2.5 Comparison of GOMA prediction with analytical solution - species mole fractions (solid lines - analytical solution; discrete data points - GOMA prediction).

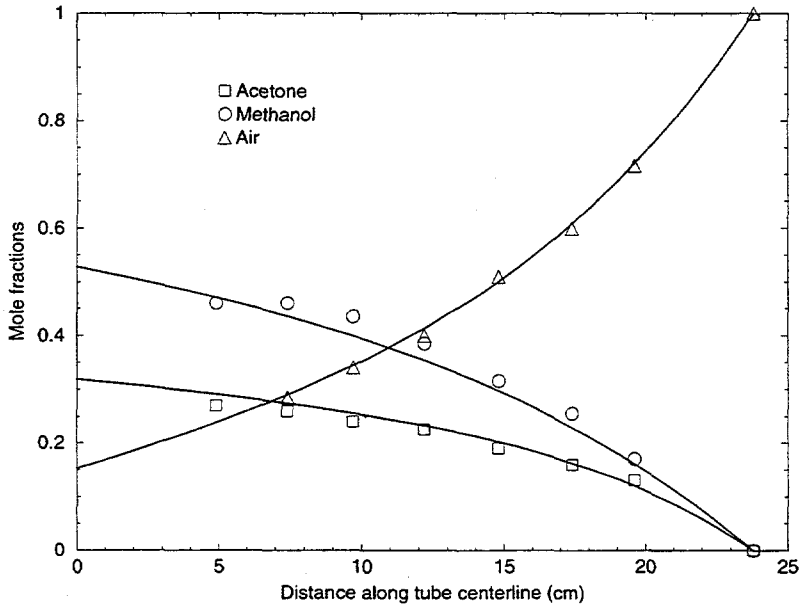

Figure 2.6 Comparison of GOMA prediction with experimental data - species mole fractions (solid lines - GOMA prediction; discrete data points - experimental data from Carty and Schrodt (1975)).

2.3 Verification of the Electrochemical Model in GOMA: modeling of an idealized battery cell

An idealized battery-cell problem in which concentration gradients are absent was suggested by our consultant, Professor John Newman of UC Berkeley, as a mean of verifying the electrochemical model implementation in GOMA. This problem has an analytical solution and brings out several aspects of a battery cell, including electrical potential differences in both electrolyte and electrode regions and chemistry in the electrode regions. The solution of this problem has been used to provide a check on several aspects of the implementation of the thermal battery simulation in GOMA. The model problem is to determine the electrical potential fields and the current density in a battery cell consisting of an anode region, a separator region, and a cathode region as shown in Figure 2.7.

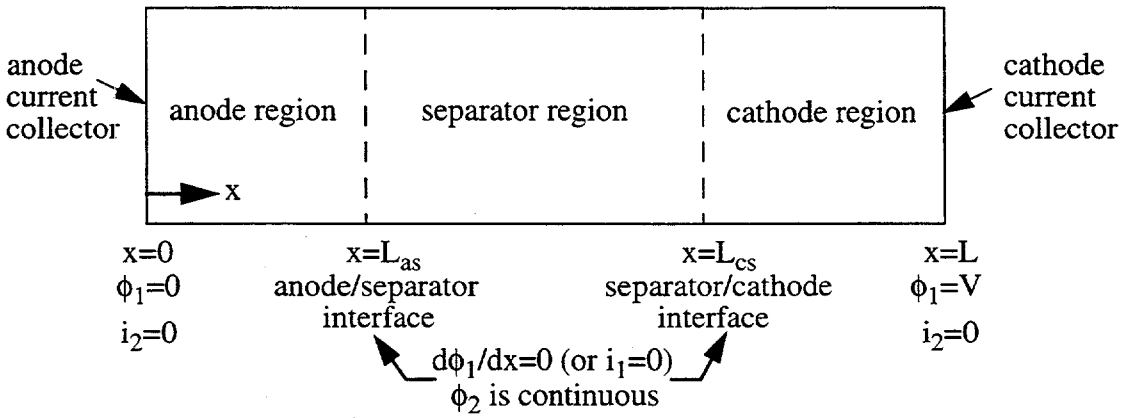

Figure 2.7. Cell description and boundary conditions.

The assumptions made to allow an analytical solution to the problem are: one-dimensional, steady-state operation with linearized Butler-Volmer kinetics, constant properties, and negligible concentration gradients. No chemical reactions are assumed to take place in the separator region. Ohm's law holds for the current densities in the solid electrode and the liquid electrolyte phases:

$$i_1 = -\sigma \frac{d\phi_1}{dx} \qquad (2.59),$$

$$i_2 = -\kappa \frac{d\phi_2}{dx} \qquad (2.60)$$

where i_1, σ, and ϕ_1, and i_2, κ, and ϕ_2 are the current densities, electrical conductivities, and electrical potentials in the electrode and electrolyte phases, respectively. In the liquid electrolyte

phase there is no electrode material so i_1 is zero; similarly, i_2 is absent or zero in the solid electrode phase. From the law of charge conservation, we have

$$\frac{d(i_1 + i_2)}{dx} = 0 \tag{2.61}.$$

Integrating Equation 2.61 yields:

$$i_1 + i_2 = I \tag{2.62}$$

where I is the total current density drawn from the battery cell.

From Faraday's law and using the Butler-Volmer expression for kinetics, we have

$$\frac{di_2}{dx} = ai_o\left[e^{\frac{\alpha_a F}{RT}(\phi_1 - \phi_2 - U_o)} - e^{-\frac{\alpha_c F}{RT}(\phi_1 - \phi_2 - U_o)}\right] \tag{2.63}$$

where a is the interfacial area per unit electrode volume, i_o is the exchange current density, α_a and α_c are anodic and cathodic transfer coefficients, respectively, F is the Faraday constant, R is the universal gas constant, T is the temperature, and U_o is the thermodynamic open circuit potential (here, we consider only a single electrochemical reaction, respectively, in the anode and cathode regions). Linearizing the Butler-Volmer expression and letting $\alpha_a = \alpha_c = 0.5$ yield:

$$\frac{di_2}{dx} = \frac{ai_oF}{RT}(\phi_1 - \phi_2 - U_o) \tag{2.64}.$$

Differentiating Equations 2.59 and 2.60 and using Equations 2.61 and 2.64 lead to the following equation, which holds in both the anode and cathode regions:

$$\frac{d^2Y}{dx^2} = BY \tag{2.65}$$

where

$$Y = \phi_1 - \phi_2 - U_o \tag{2.66}$$

and

$$B = \frac{ai_oF}{RT}\frac{(\sigma + \kappa)}{\sigma\kappa} \tag{2.67}.$$

The boundary conditions are:

$$\phi_1 = 0,\ i_2 = 0 \text{ at } x = 0 \text{ (at the anodic current collector)} \quad (2.68),$$

$$\phi_1 = V,\ i_2 = 0 \text{ at } x = L \text{ (at the cathodic current collector)} \quad (2.69),$$

$$i_1 = 0 \text{ and } \Phi_2 \text{ is continuous at } x = L_{as} \text{ (at the anode/separator interface)} \quad (2.70),$$

$$i_1 = 0 \text{ and } \Phi_2 \text{ is continuous at } x = L_{cs} \text{ (at the cathode/separator interface)} \quad (2.71).$$

The solution of Equation 2.65 in the anode region (applying boundary conditions, Equations 2.68 and 2.70, and constraint 2.62 for the total current density) is

$$Y(x) = -(\phi_2|_{x=0} + U_{o,a})\cosh(\sqrt{B}x) - \frac{I}{\sigma\sqrt{B}}\sinh(\sqrt{B}x) \quad (2.72)$$

where $U_{o,a}$ is the thermodynamic open-circuit potential in the anode region. From

$$\left.\frac{dY}{dx}\right|_{x=L_{as}} = \frac{I}{\kappa} = -\sqrt{B}(\phi_2|_{x=0} + U_{o,a})\sinh(\sqrt{B}L_{as}) - \frac{I}{\sigma}\cosh(\sqrt{B}L_{as}) \quad (2.73)$$

Equation 2.72 can be re-written as:

$$Y(x) = \frac{I}{\sigma\sqrt{B}}\left\{\left[\frac{\sigma + \kappa\cosh(\sqrt{B}L_{as})}{\kappa\sinh(\sqrt{B}L_{as})}\right]\cosh(\sqrt{B}x) - \sinh(\sqrt{B}x)\right\} \quad (2.74).$$

Since

$$i_2 = I - i_1 = -\kappa\frac{d\phi_2}{dx} = I + \sigma\frac{d\phi_1}{dx} \quad (2.75),$$

an expression relating ϕ_1 and ϕ_2 in the anode region is

$$\phi_2(x) = \phi_2|_{x=0} - \frac{I}{\kappa}x - \frac{\sigma}{\kappa}\phi_1 \quad (2.76).$$

Combining Equations 2.66, 2.73, and 2.76 yields an expression for ϕ_1 in the anode region:

$$\phi_1 = \frac{Y - \frac{I}{\kappa}x - \frac{I[\sigma + \kappa\cosh(\sqrt{B}L_{as})]}{\kappa\sigma\sqrt{B}\sinh(\sqrt{B}L_{as})}}{1 + \sigma/\kappa} \qquad (2.77),$$

in terms of the solution $Y(x)$ and the total current density I. The variation of ϕ_2 in the anode region then follows from 2.66. Thus the potentials in the solid electrode and liquid electrolyte phases in the anode region are determined once the total current density is known.

Similarly, the solution of 2.65 in the cathode region (applying boundary conditions, Equations 2.69 and 2.71 and constraint 2.62 for the total current density) is

$$Y(x) = -(\phi_2|_{x=0} + U_{o,c} - V)\cosh[\sqrt{B}(L-x)] + \frac{I}{\sigma\sqrt{B}}\sinh[\sqrt{B}(L-x)] \qquad (2.78)$$

where $U_{o,c}$ is the thermodynamic open-circuit potential in the cathode region. From

$$\left.\frac{dY}{dx}\right|_{x=L_{cs}} = \frac{I}{\kappa} = \sqrt{B}(\phi_2|_{x=0} + U_{o,c} - V)\sinh[\sqrt{B}(L-L_{cs})] - \frac{I}{\sigma}\cosh[\sqrt{B}(L-L_{cs})] \qquad (2.79)$$

Equation 2.78 can be re-written as:

$$Y(x) = -\frac{I}{\sigma\sqrt{B}}\left\{\left[\frac{\sigma + \kappa\cosh[\sqrt{B}(L-L_{cs})]}{\kappa\sinh[\sqrt{B}(L-L_{cs})]}\right]\cosh[\sqrt{B}(L-x)] - \sinh[\sqrt{B}(L-x)]\right\}. \qquad (2.80).$$

From 2.75 and using boundary condition 2.69, ϕ_2 in the cathode region is

$$\phi_2(x) = \phi_2|_{x=L} + \frac{I}{\kappa}(L-x) + \frac{\sigma}{\kappa}(V - \phi_1) \qquad (2.81).$$

Combining Equations 2.66, 2.79, and 2.81 yields an expression for ϕ_1 in the cathode region:

$$\phi_1 = V + \frac{Y + \frac{I}{\kappa}(L-x) + \frac{I\{\sigma + \kappa\cosh[\sqrt{B}(L-L_{cs})]\}}{\kappa\sigma\sqrt{B}\sinh[\sqrt{B}(L-L_{cs})]}}{1+\sigma/\kappa} \tag{2.82}$$

in terms of the solution $Y(x)$ and the total current density I. The variation of ϕ_2 in the cathode region then follows from Equation 2.66.

In the separator region ($L_{as} \le x \le L_{cs}$) there is only the electrolyte phase thus i_1 and ϕ_1 are undefined, yielding a linear variation of ϕ_2:

$$i_2 = I = -\kappa\frac{d\phi_2}{dx} = \text{constant} \tag{2.83}$$

$$\phi_2\big|_{x=L_{as}} - \frac{I}{\kappa}(L_{cs}-L_{as}) = \phi_2\big|_{x=L_{cs}} \tag{2.84}.$$

Now applying the internal conditions, Equations 2.70 and 2.71, to Equation 2.84 and using Equations 2.66 and 2.77 yield

$$\phi_2\big|_{x=L_{as}} = -U_{o,a} - \frac{\frac{\sigma}{\kappa}Y\big|_{x=L_{as}} + \frac{IL_{as}}{\kappa} + \frac{I[\sigma+\kappa\cosh(\sqrt{B}L_{as})]}{\kappa\sinh(\sqrt{B}L_{as})}}{1+\sigma/\kappa} \tag{2.85}$$

and using Equations 2.66 and 2.82 gives

$$\phi_2\big|_{x=L_{cs}} = V - U_{o,c} + \frac{\frac{I(L-L_{cs})}{\kappa} - \frac{\sigma}{\kappa}Y\big|_{x=L_{cs}} + \frac{I\{\sigma+\kappa\cosh[\sqrt{B}(L-L_{cs})]\}}{\kappa\sigma\sqrt{B}\sinh[\sqrt{B}(L-L_{cs})]}}{1+\sigma/\kappa} \tag{2.86}.$$

Substituting Equation 2.74 evaluated at $x = L_{as}$ into Equation 2.85, substituting Equation 2.80 evaluated at $x = L_{cs}$ into Equation 2.86, and substituting the results into Equation 2.84 yields the final expression for the total current density:

$$I = (\sigma+\kappa)(U_{o,c} - U_{o,a} - V) \div \left\{ L + \frac{\sigma}{\kappa}(L_{cs}-L_{as}) + \frac{(\sigma^2+\kappa^2)}{\sigma\kappa\sqrt{B}}\coth(\sqrt{B}L_{as}) + \right. \tag{2.87}.$$

$$\left. \coth[\sqrt{B}(L-L_{cs})]\} + \frac{2}{\sqrt{B}}\{\operatorname{csch}(\sqrt{B}L_{as}) + \operatorname{csch}[\sqrt{B}(L-L_{cs})]\} \right\} .$$

The following example is provided to illustrate the solution and to serve as a verification on the electrochemical-model implementation in GOMA. Let L_{as} = 0.33 cm, L_{cs} = 0.67 cm, L = 1.0 cm, ai_o = 0.05 A/cm^3, T = 723 K, σ = 1900 ohm^{-1} cm^{-1}, κ = 2 ohm^{-1} cm^{-1}, V = 1.25 volt, $U_{o,c}$ = 1.35 volt, $U_{o,a}$ = 0.0 volt, F = 96487 Coulomb/mole, and R = 8.314 J/mole-K. Figure 2.8 shows the variation of the electrolyte potential ϕ_2 across the cell. At the current collectors the slope of the curve is zero, thus satisfying the boundary conditions that the electrolyte current density i_2 is zero at these boundaries. Also note the linear variation of ϕ_2 in the separator region ($L_{as} \le x \le L_{cs}$) noted above in Equation 2.84. The results shown in Figure 2.8 agree with those shown in Figure 3 of Larson (1998). Also shown in Figure 2.8 is the predicted variation of ϕ_2 across the cell from a GOMA calculation; the agreement is good. The total current density I for this case is 0.0128 A/cm^2, in agreement with the value given by Larson (1998). Figures 2.9 and 2.10 show the variation of the electrode potential ϕ_1 in the anode and cathode regions, respectively; both analytical and GOMA results are presented, and the agreement is excellent. In Figure 2.9, the electrode potential is zero at the anode current collector in agreement with the boundary condition, and the gradient of ϕ_1 is zero at the anode/separator interface in agreement with the condition that $i_1 = 0$ at the interface. Similarly in Figure 2.10, the potential is equal to V (=1.25 volt) at the cathode current collector in agreement with the boundary condition, and the gradient of ϕ_1 is zero at the separator/cathode interface in agreement with the condition that $i_1 = 0$ at the interface.

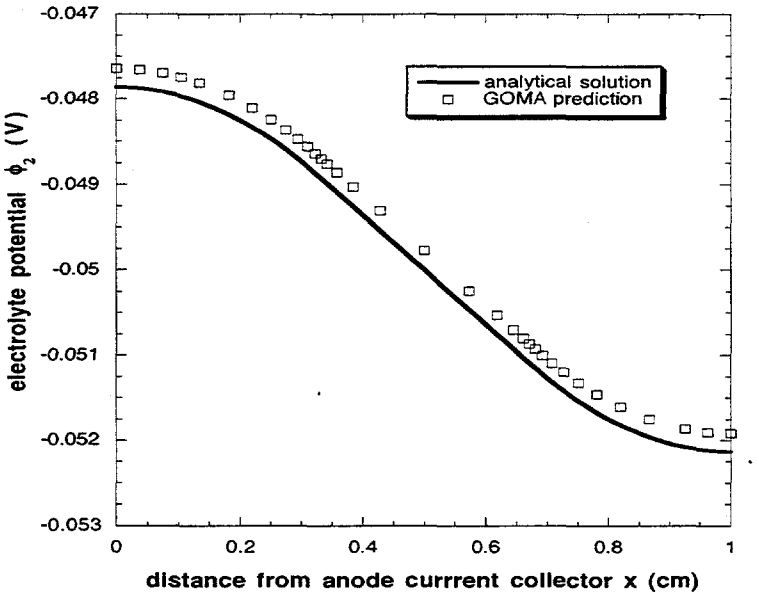

Figure 2.8. Variation of electrolyte potential ϕ_2.

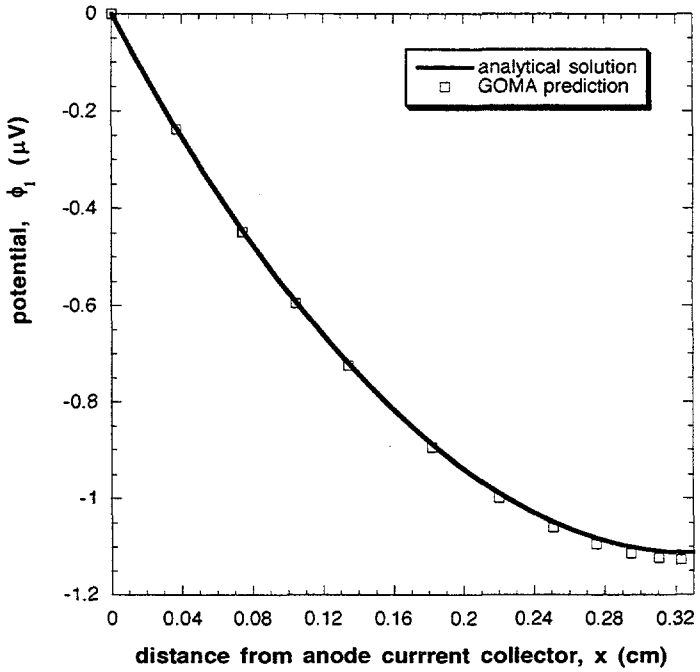

Figure 2.9. Variation of solid-phase potential ϕ_1 in anode region.

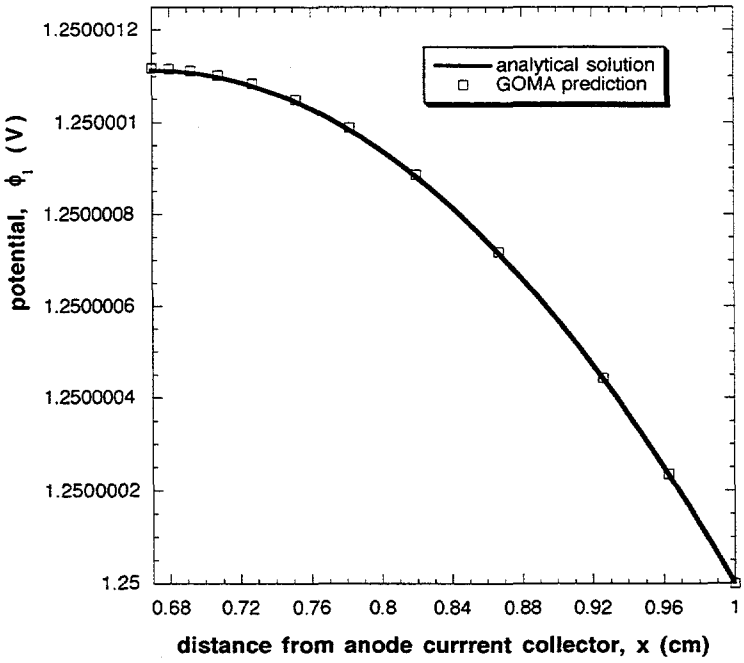

Figure 2.10. Variation of solid-phase potential ϕ_1 in cathode region.

2.4 Results of Base-Case Study, Verification and Validation, and Design-Parameter Studies for the GOMA Thermal Battery Cell Model

There are three sub-sections in this section. To illustrate the application or utility of the GOMA thermal battery cell model, we first report, in Sub-section 2.4.1, results from a base-case study: computed predictions of species mole fractions, electrical potentials in the liquid-electrolyte and solid-electrode phases, average porosity in anode and cathode, electrolyte temperature, cell current density, and total cell voltage by solving the governing equations, Equations 2.1, 2.7, 2.10, 2.13, 2.16 and 2.20 (along with auxiliary equations, Equations 2.2, 2.6, 2.9, 2.15, 2.21, 2.22) along with the boundary conditions (Equations 2.31 - 2.32, 2.34 - 2.36) and initial conditions (Equation 2.38) in GOMA. In Sub-section 2.4.2, we document a study of verifying the GOMA thermal battery cell model by comparing its predictions with those of Bernardi and Newman (1987) for a LiAl/LiCl-KCl/FeS_2 cell; and we also report results on validating the GOMA thermal battery cell model by comparing GOMA predictions with limited thermal battery discharge-performance data from the open literature (Dunning 1981) for a LiAl/LiCl-KCl/FeS_2 cell and from Sandia (Guidotti 1996) for a LiSi/LiCl-KCl/FeS_2 cell. Lastly, in Sub-section 2.4.3, we document parametric studies (in which three key parameters were varied) for a cell operating under constant current density conditions.

2.4.1 Results of Base-Case Study

To focus on the electrochemical aspect of the thermal battery process, we set the velocity vector to zero throughout; this is justifiable because the rate of change of the convective flux is orders of magnitude (about 10^{-4}) smaller than the rate of changes of the diffusive flux and the rate of electrochemical reactions. To simplify our analysis further, we employed a lumped energy-transport model with Joule heating neglected. Table 2.1 lists the process parameters used in the base-case study. Figure 2.11 displays the finite-element mesh employed in our base-case study. This mesh has a total of 120 quadratic elements, which result in a total of 2025 unknowns. As can be seen in Figure 2.11, the mesh is scaled in the direction normal to the current collectors and toward the electrode/separator interfaces in order to properly capture the rapid changes in species mole fractions. Results of a mesh-refinement study are presented in Figure 2.19.

Constant total cell voltage and varying cell current density. Computed predictions for the case of constant total cell voltage (V = 1.7 Volts) are presented in Figures 2.12 - 2.17. Figure 2.12 shows the Li^+ mole-fraction distribution in the direction normal to the current collectors at various times. Clearly, the zero-gradient boundary conditions at the current collectors are met. The mole fraction of Li^+ increases with time in the anode region due to Li^+ production reactions; similarly, it decreases with time in the cathode region due to the Li^+ consumption reaction. Figure 2.13 displays profiles of the electrical potential in the electrolyte at various times. Again, the zero-gradient boundary conditions at the current collectors are met; as time increases, the electrolyte potential level rises with decreasing potential difference between the collectors, indicating the decrease of cell current density with time (cf. Figure 2.16). Figures 2.14a and 2.14b show the profiles of the

solid-phase electrical potential in the anode and cathode regions, respectively. The zero-gradient boundary conditions at the anode/separator and separator/cathode interfaces are met and the slopes at the current collectors are finite; as time increases, the electrode potential level rises in the anode but drops in the cathode; in both electrodes the potential differences between the current collectors and the separator/electrode interfaces decrease, indicating the decreasing cell current density. Figure 2.15a and 2.15b display the average porosity, respectively, for the anode and the cathode. As expected, average porosity in the anode rises because of the consumption of the solid anode material; in contrast, the average porosity in the cathode drops because of the deposition of solid materials generated from the reduction reactions. Figure 2.16 shows that for the Base Case conditions (constant cell voltage of 1.7V and process parameters given in Table 2.1) the cell current density rises slightly during the first 90 seconds or so; it then starts to drop - first slowly but then the rate of drop accelerates as time increases. Lastly, Figure 2.17 shows the average temperature as a function of time in the cell. The cell temperature decreases with time due to the loss of heat to the surroundings, as expected.

Table 2.1. Process Parameters Used in the Base Case

Electrode and separator dimensions:

$L_a = 0.088$ cm

$L_s = 0.07$ cm

$L_c = 0.046$ cm

Electrical conductivity of Solid Electrode:

$\sigma_a = 250000\ \Omega^{-1}\ cm^{-1}$

$\sigma_c = 1900\ \Omega^{-1}\ cm^{-1}$

Stefan-Maxwell diffusivities:

$D_{12} = 4.5x10^{-5}\ cm^2/s$

$D_{13} = 4.5x10^{-5}\ cm^2/s$

$D_{23} = 4.5x10^{-5}\ cm^2/s$

Initial porosity of electrodes:

$\varepsilon_a^0 = 0.275$

$\varepsilon_c^0 = 0.244$

Porosity of separator:

$\varepsilon_s = 0.244$

Total mass of the battery cell:

$m = 2.8634$ g

Cross-sectional area of electrode disks:

$A = 7.917\ cm^2$ (electrode disk diameter = 1.25")

Initial and ambient temperatures:

$T_0 = 846$ K, $T_a = 298$ K.

Heat capacity of the battery cell:

$C_p = 0.874$ J/g-K

Heat transfer coefficient:

$h = 1.25x10^{-4}\ W/cm^2$ - K

Anodic transfer coefficients:

$\alpha_{a,anode} = 0.5$, $\alpha_{c,anode} = 0.5$.

Cathodic transfer coefficients:

$\alpha_{a,cathode} = 1.0$, $\alpha_{c,cathode} = 1.0$.

Exchange current density for anodic reaction:

$ai_{0,anode} = 10\ A/cm^3$.

Exchange current density and activation energy for cathodic reaction at zero utilization:

$ai_{0,0\ cathode} = 20\ A/cm^3$.

E = 20 kcal/mole

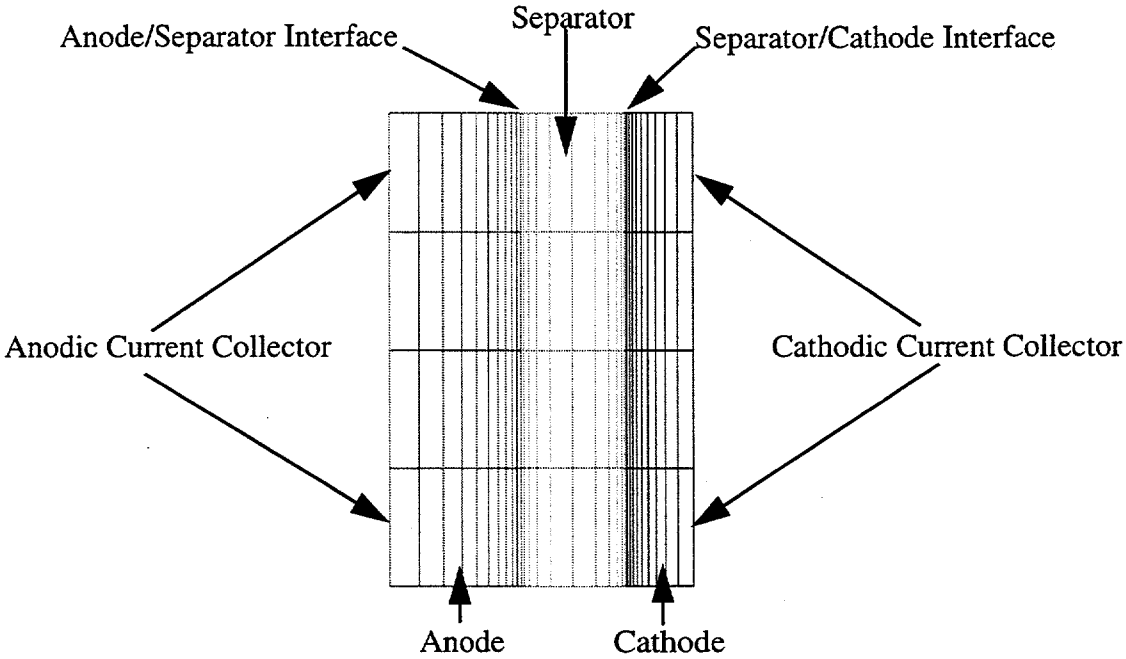

Figure 2.11 Finite-element mesh used in the case-study calculations
(a total of 120 elements and 2025 unknowns)

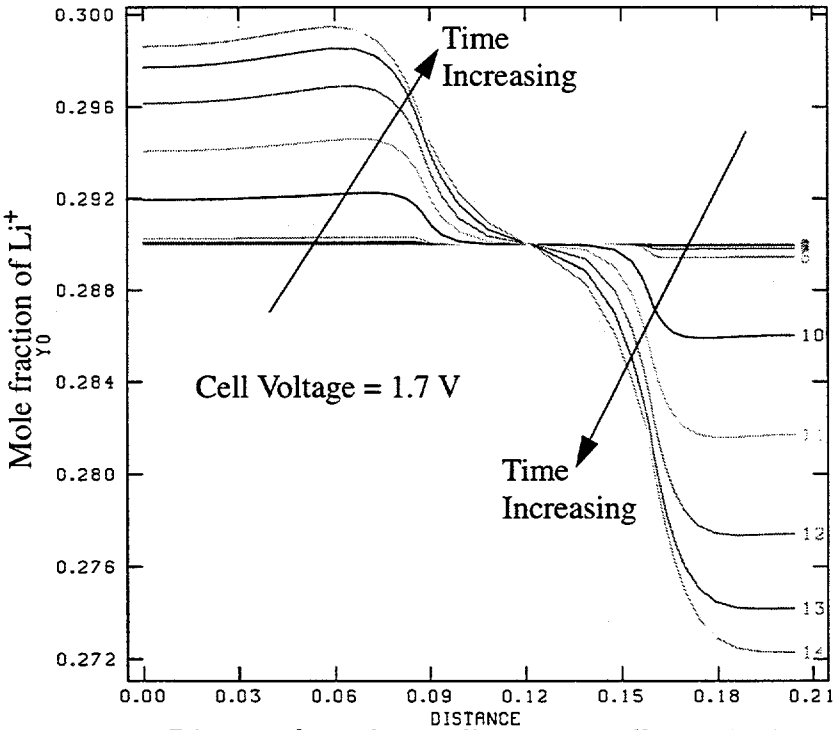

Distance from the anodic current collector (cm)

Figure 2.12 Sample prediction: mole fraction of Li^+ across battery cell with constant cell voltage (Parameters are listed in Table 2.1)

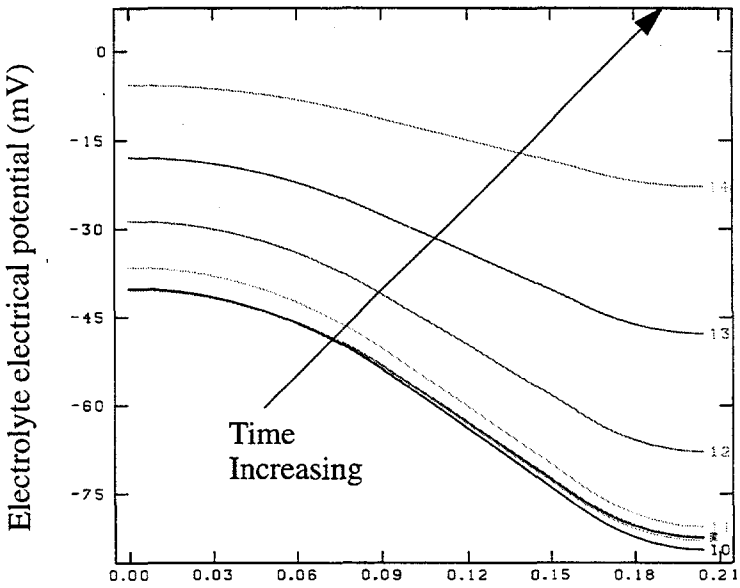

Figure 2.13 Sample prediction: electrolyte electrical potential across battery cell with constant cell voltage (Parameters are listed in Table 2.1)

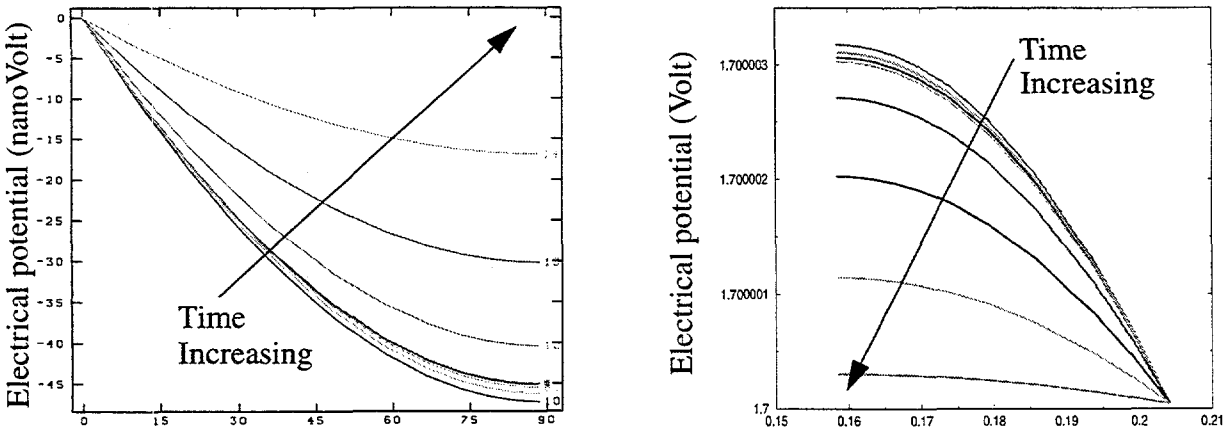

Figure 2.14 Sample prediction: electrical potential in the solid electrode phase across the anode and the cathode with constant cell voltage
(Parameters are listed in Table 2.1).
(a) in the anode region; (b) in the cathode region.

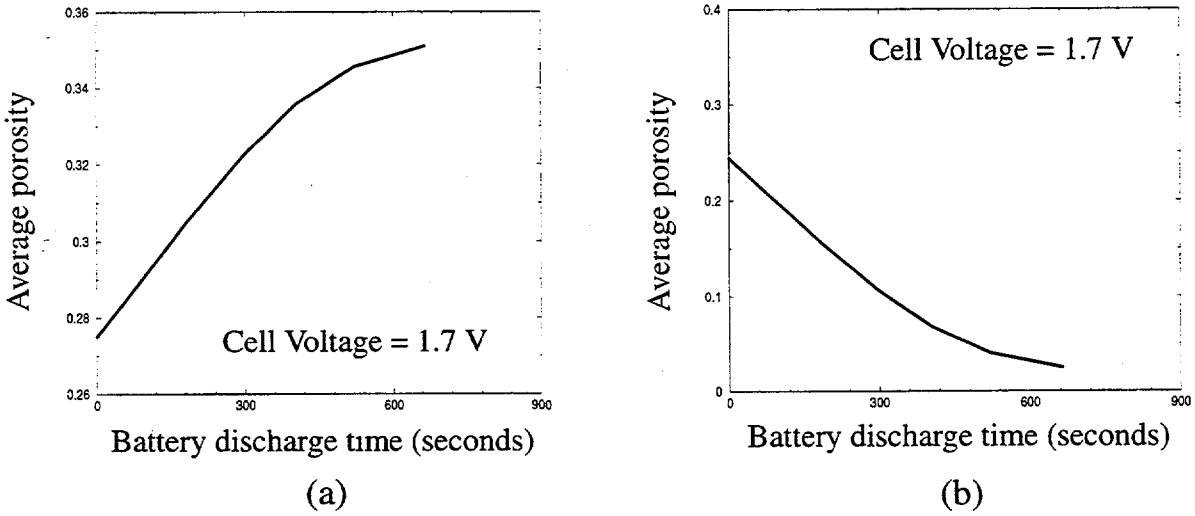

Figure 2.15 Sample prediction: evolution of average porosity in electrodes with constant cell voltage (Parameters are listed in Table 2.1).
(a) Anode; (b) Cathode.

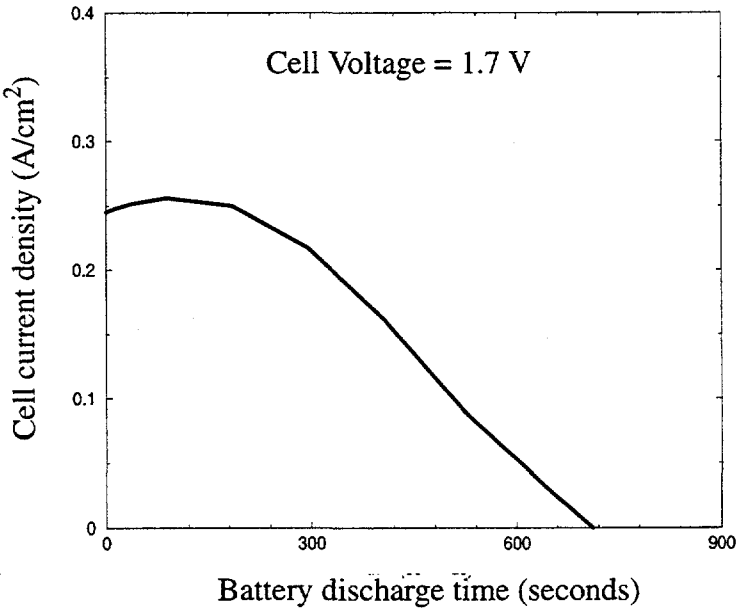

Figure 2.16 Sample prediction: evolution of battery-cell current density with constant cell voltage (Parameters are listed in Table 2.1).

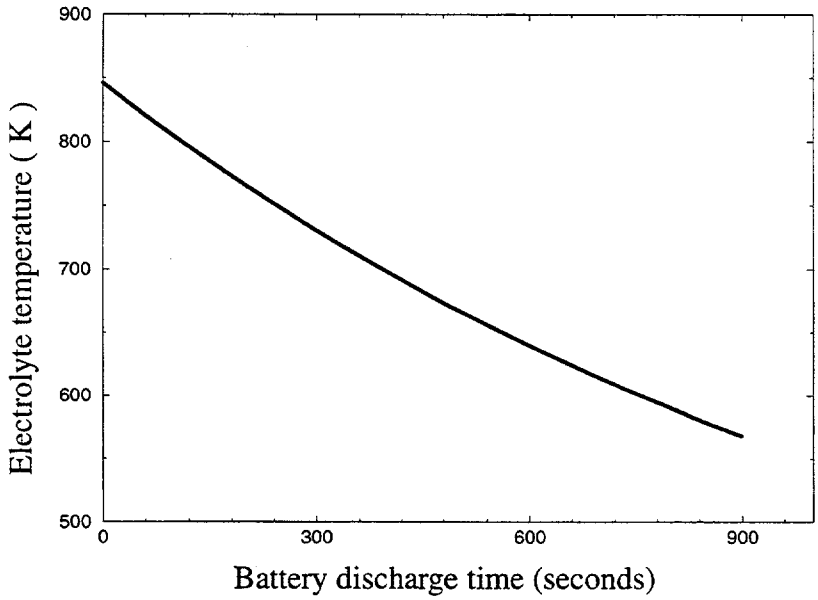

Figure 2.17 Sample prediction: evolution of electrolyte temperature (Parameters are listed in Table 2.1)

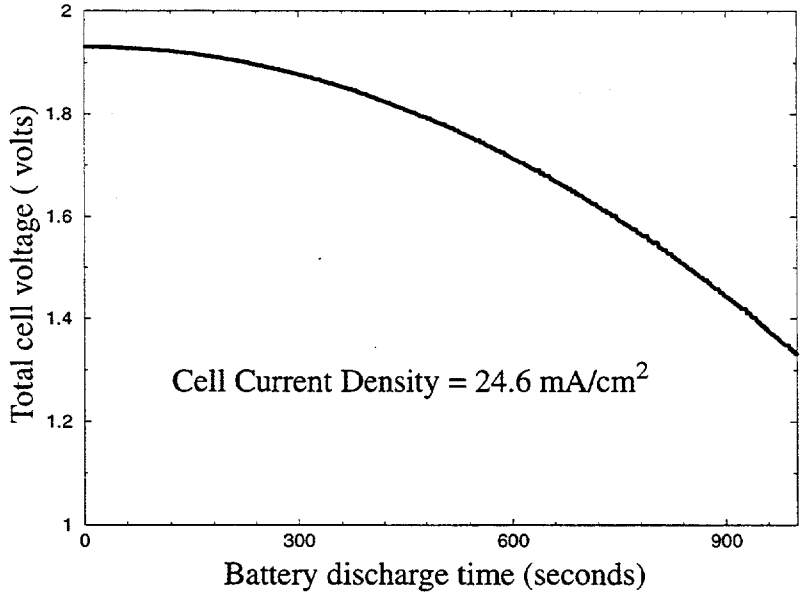

Figure 2.18 Sample prediction: evolution of total cell voltage with constant cell current density (Parameters are listed in Table 2.1).

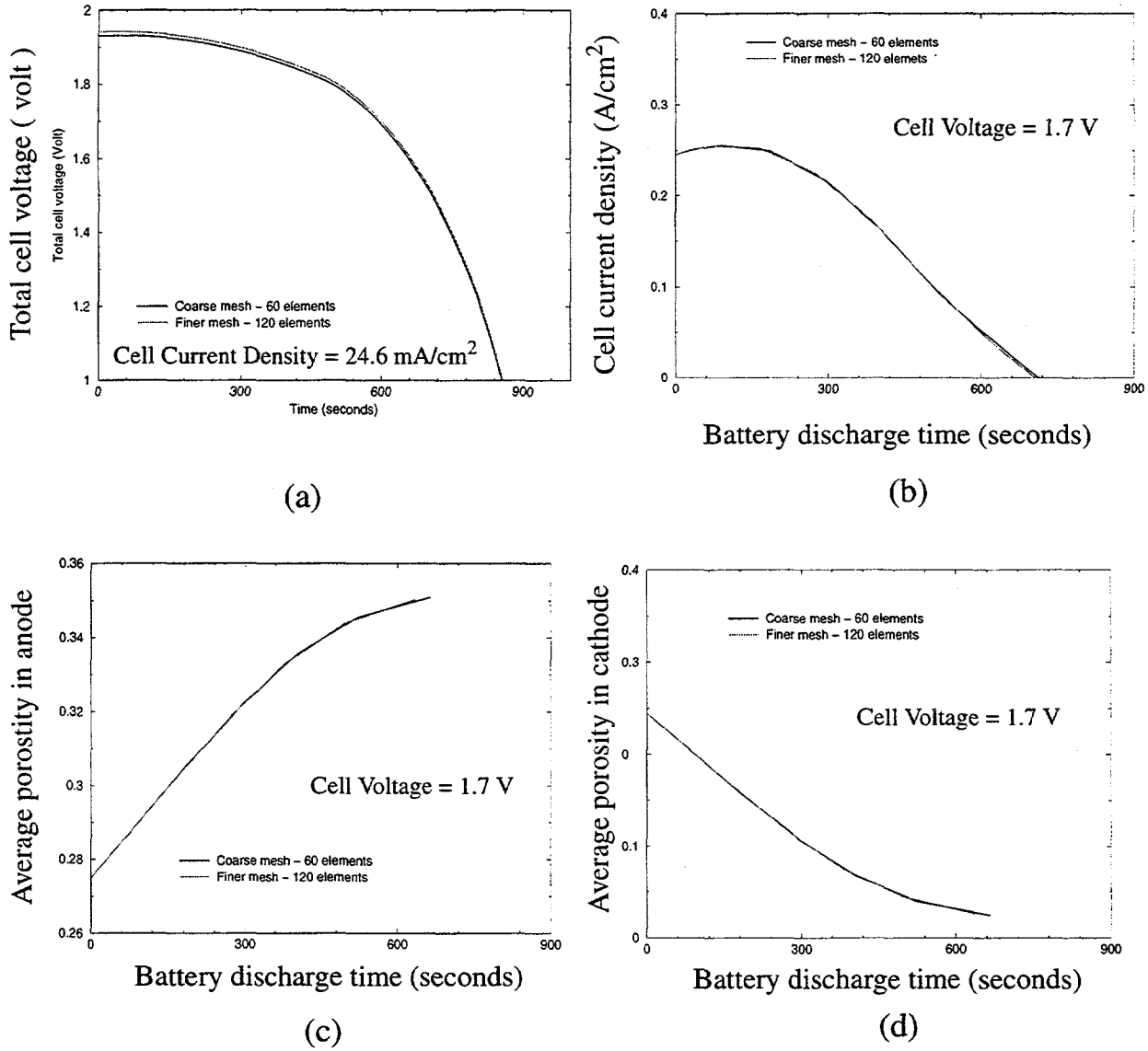

Figure 2.19 Effects of Mesh Refinements on Selected Computed Predictions

a) total cell voltage vs. time,
b) cell current density vs. time,
c) average porosity in anode vs. time,
d) average porosity in cathode vs. time.

Constant cell current density and varying total cell voltage. Figure 2.18 displays the computed prediction of total cell voltage as a function of time for the case of constant current density (I = 24.6 mA/cm^2). As can be seen from Figure 2.18, the total cell voltage decreases slowly for the first 5 minutes or so but drops more rapidly afterward.

The effect of mesh refinement on several results of interest is presented in Figure 2.19, which shows that doubling the total number of mesh elements from 60 to 120 has a very small effect on the computed predictions. Consequently, the 60-element mesh was used in the case-study calculations. With this 60-element mesh and for the case of constant cell voltage and varying cell current density, approximately 30 minutes of CPU time were required to simulate 15 minutes of discharge time on a 400 MHz SUN ULTRASPARC workstation. For the case of constant cell current density and varying cell voltage (again with the 60-element mesh), approximately 8 hours of CPU time were required to simulate 15 minutes of the voltage-vs.-time curve; the significant increase in computer time was due to the iteration required on the voltage boundary condition.

It should be pointed out that the effects of input- (or process-) parameter uncertainties on the statistical variations of computed output variables (e.g. species mole fractions, electrical potentials, cell current density, cell voltage, etc.) have not been investigated. Such effects can be significant, depending on the input-parameter uncertainty distributions, as shown by one of the authors of this report (Chen 1995, 1996; Chen and Cairncross 1997) in two non-deterministic analyses, respectively, for thermal response of a metal-plate object subject to a participating engulfing pool fire and for a liquid polymeric-film drying process. In short, estimation of process parameters (e.g. exchange current density, activation energy, diffusion coefficients, etc.) and assessing the effects of their uncertainties on battery discharge performance remain a challenge that awaits future efforts.

2.4.2 Verification and Validation

To verify our GOMA thermal battery cell model, we computed the discharge cell voltage as a function of time for a LiAl/LiCl-KCl/FeS_2 cell that has been studied by Bernardi and Newman (1987) using a different model formulation (in which the total flux is subdivided into diffusion, migration, and convection) and a numerical solution technique based on the finite difference method. The relevant parameters for this verification study are listed in Table 2.2. Figures 2.20a & 2.20b compare the GOMA predictions of dynamic cell voltage with those of Bernardi and Newman (1987) for two sets of operating conditions and up to the end of the first reduction electrochemical reaction in the cathode (i.e. Reaction a in Equation 2.28). Clearly, predictions from the two models agree very well except toward the end of Reaction a where percent utilization of the cathode starting material, FeS_2, approaches 37.5. The discrepancy near 37.5% utilization is mainly due to the fact that we employed a sequential reaction mechanism in the present GOMA model (i.e. only one reaction is allowed to proceed in each reaction region as presented in Equation 2.28) whereas Bernardi and Newman (1987) allowed simultaneous reactions. Incorporation of the simultaneous reaction mechanism in the present GOMA battery-cell model awaits future efforts.

Table 2.2. Process Parameters Used in the Verification of the GOMA Thermal Battery Cell Model

Electrode and separator dimensions:
$L_a = 0.32$ cm
$L_s = 0.2146$ cm
$L_c = 0.2146$ cm

Electrical conductivity of Solid Electrode:
$\sigma_a = 250000\ \Omega^{-1}\ cm^{-1}$
$\sigma_c = 1900\ \Omega^{-1}\ cm^{-1}$

Stefan-Maxwell diffusivities:
$D_{12} = 3.5x10^{-5}\ cm^2/s$
$D_{13} = 3.5x10^{-5}\ cm^2/s$
$D_{23} = 3.5x10^{-5}\ cm^2/s$

Initial porosity of electrodes:
$\varepsilon_a^0 = 0.755$
$\varepsilon_c^0 = 0.755$

Anodic transfer coefficients:
$\alpha_{a,anode} = 0.5$, $\alpha_{c,anode} = 0.5$.

Cathodic transfer coefficients:
$\alpha_{a,cathode} = 1.0$, $\alpha_{c,cathode} = 1.0$.

Exchange current density for anodic reaction:
$ai_{0,anode} = 10\ A/cm^3$.

Exchange current density for cathodic reaction:
$ai_{0,cathode} = 5\ A/cm^3$.

Porosity of separator:
$\varepsilon_s = 0.755$

In Figure 2.20b the cell voltage predicted by GOMA is compared with the experimental data of Dunning (1981) for a LiAl/LiCl-KCl/FeS_2 cell that operates with an isothermal temperature of 450° C, a cell current density of 50 mA/cm^2, and an initial LiCl molar concentration of 68%. Aside from the initial period of discharge where % utilization is close to zero and the end of Reaction a where % utilization approaches 37.5, the agreement between GOMA prediction and experimental data is very good. The discrepancy near 37.5% utilization can be attributed to the sequential reaction mechanism employed in the GOMA model whereas the discrepancy near 0% utilization may be due to measurement uncertainties and/or the start-up phenomena that is not captured in the model.

In Figures 2.21 and 2.22 the GOMA thermal battery cell model is further validated against the experimental data provided by Ronald Guidotti of the Power Source Engineering Department (formerly Thermal Battery Development and Manufacturing Department) at Sandia for a LiSi/ LiCl-KCl/FeS_2 cell operating under nonisothermal conditions with a constant current density of 24.6 mA/cm^2. The other process and model parameters are those listed in Table 2.1. Figure 2.21 shows the electrolyte (or cell) temperature as a function of time whereas Figure 2.22 displays cell voltage as a function of time. Aside from the initial start-up period of 15 seconds or so, the cell or electrolyte temperature as predicted by GOMA agrees almost perfectly with the experimental data for the first 10 minutes or so of discharge time. Discrepancy arises afterward due to several factors: 1) the Joule heating effect, which has been neglected in the present model, but which can be important as the cell voltage deviates significantly from the thermodynamic open-circuit potential;

2) time-dependent heat capacity of the cell due to the formation and solidification of known and unknown intermediate compounds as heat is lost to the surroundings – in the present GOMA model, the heat capacity of the cell is kept constant; 3) temperature gradients within the cell, which may arise as battery-cell discharge proceeds and more and more intermediate compounds are formed in the electrode regions. Similarly, the cell voltage as predicted by GOMA agrees almost perfectly with the experimental data for the first 10 minutes or so of discharge time, but discrepancy arises after that and becomes more pronounced at longer times. This may be attributed to the following factors: 1) precipitation of KCl and LiCl salts during discharge, which results in the further reduction of porosity in the cathode and thus additional drop in the cell voltage – this effect can eventually result in pore plugging and thus shut off the battery discharge process (cf. Pollard and Newman 1981); 2) a difference between the reduction electrochemical reaction in the cathode and that presented in Equation 2.28 when the cell temperature is well below 450°C (which is the case when discharge time exceeds 10 minutes, as shown in Figure 2.21); 3) formation and solidification of unknown intermediate compounds, which affect not only electrode chemistry but also the species transport processes and properties; 4) discrepancy in cell temperature between model prediction and experimental data.

2.4.3 Design-Parameter Studies

In this sub-section we document the effects of three key design parameters on the battery-cell performance. The ability to explore the dependence of battery performance on battery design parameters is of critical interest to the thermal battery designers at Sandia. The three key design parameters selected are cell current density, cathode thickness, and heat transfer coefficient. Cell current density is the most important design parameter because it specifies the power output by the battery. The electrode thicknesses are relevant because the battery-cell volume depends on them. Since thermal batteries are usually designed so that they are cathode limited, we have chosen to study the effect of the cathode thickness here. Lastly, the heat transfer coefficient controls the rate of heat lost to the surroundings in our lumped energy-transport model. It should be pointed out that time and budget constraints prevented us from conducting more extensive parameter studies; however, the results reported in this sub-section should help illustrate how the GOMA thermal battery cell model can be employed to study battery performance with respect to various process design parameters. The other process and model parameters are those listed in Table 2.1.

Results of our design parameter studies are presented in Figures 2.23 - 2.25: the effect of cell current density on discharge cell voltage is shown in Figure 2.23, the effect of cathode thickness is shown in Figure 2.24, and the effect of heat transfer coefficient is shown in Figure 2.25. With the process conditions chosen (as listed in Table 2.1) and at the discharge time of 15 minutes, lowering the heat transfer coefficient from 2.5×10^{-4} W/cm^2-K to 0.625×10^{-4} W/cm^2-K (a factor of 4) results in an almost 30% increase in the cell voltage, whereas raising the cell current density from 10 mA/cm^2 to 50 mA/cm^2 (a factor of 5) produces a drop in the cell voltage of only 7%. Effect of the cathode thickness is even less significant: increasing the cathode thickness by a factor of 46 (from $L_c = 0.01$ cm to $L_c = 0.46$ cm) raises the cell voltage by merely 2%. It should be emphasized that

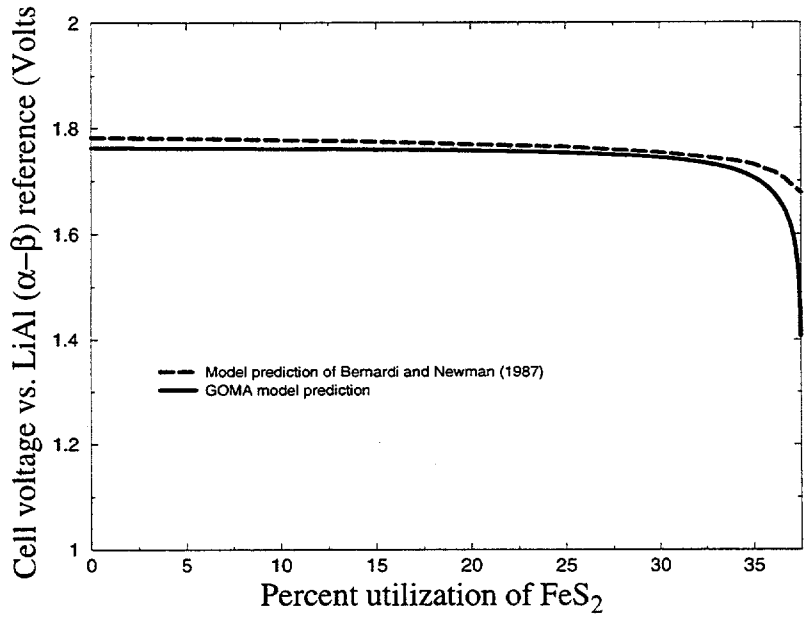

(a)

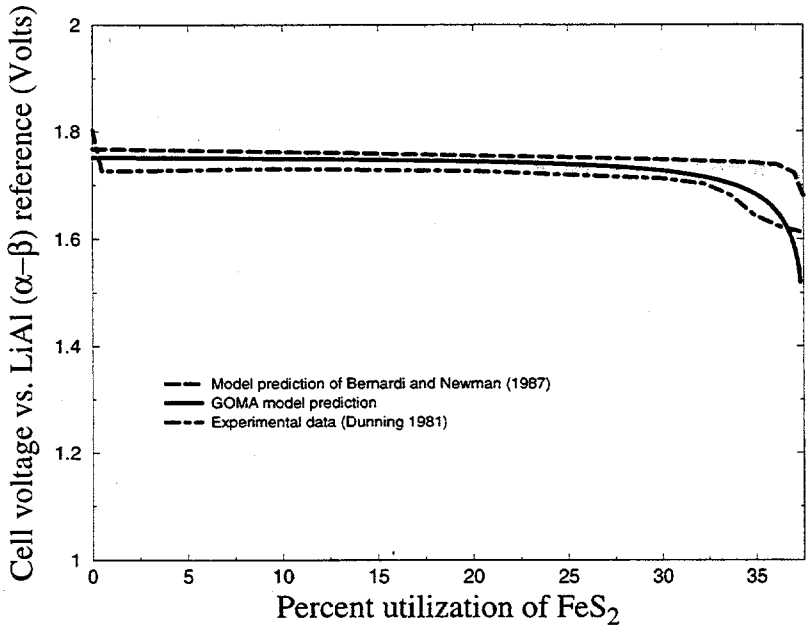

(b)

Figure 2.20 Verification of the GOMA thermal battery cell model
(Parameters are listed in Table 2.2)
(a) T = 470 °C, I = 41.6 mA/cm^2,
initial molar concentration of LiCl = 58%;
(b) T = 450 °C, I = 50 mA/cm^2, 68% LiCl electrolyte.
initial molar concentration of LiCl = 68%.

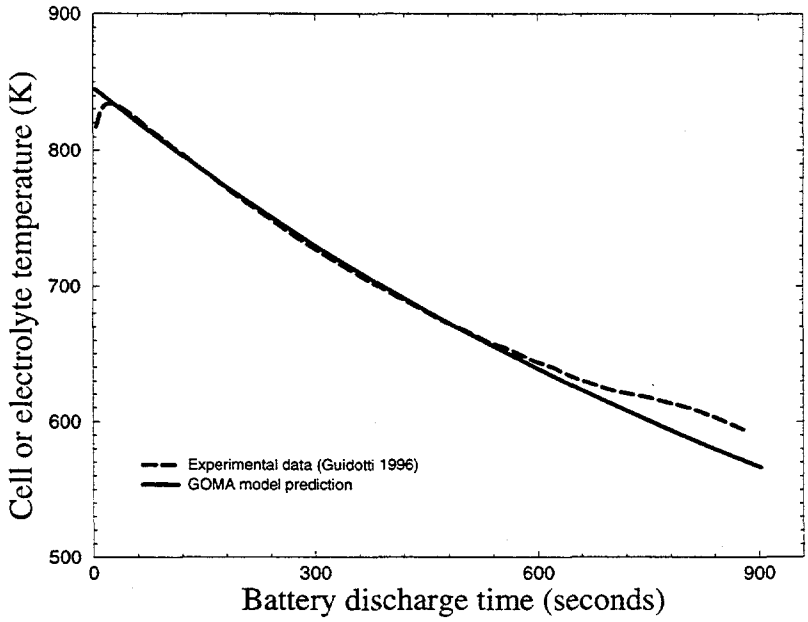

Figure 2.21 Validation of the GOMA thermal battery cell model:
cell or electrolyte temperature as a function of discharge time
(Parameters are listed in Table 2.1; data provided by Guidotti 1996).

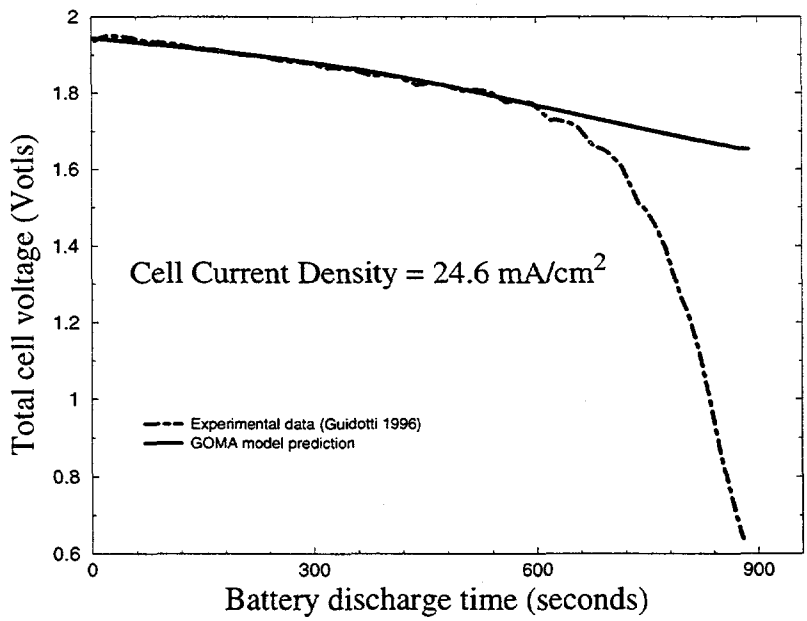

Figure 2.22 Validation of the GOMA thermal battery cell model:
total cell voltage as a function of discharge time
(Parameters are listed in Table 2.1; data provided by Guidotti 1996).

these results apply to a discharge time of 15 minutes and for the process conditions chosen (as listed in Table 2.1) only. It is expected that as discharge time increases, the effects of current density and cathode thickness on cell voltage will significantly increase. Lastly, the effect of the heat transfer coefficient on the cell temperature is presented in Figure 2.26. As expected, the heat transfer coefficient has a significant effect on the cell temperature, and this in turn strongly affects the cell voltage.

A comment is in order before closing this chapter. Due to time and budget constraints, in the present work we have not studied the effects of electrode-thickness non-uniformity, which will introduce the multi-dimensional transport phenomena that the present GOMA model was designed and developed to handle. Carrying out such a study to examine the effects of electrode-thickness non-uniformity on the cell voltage, though, awaits future efforts.

List of Symbols

(see Table 2.1 for others)

A - electrode cross-sectional area (m^2)

a - interfacial surface area per unit volume (m^{-1})

$\hat{c}$ - inertial coefficient

$c_{A,B}$ - molar concentration of salts A,B ($moles/m^3$)

c_p - specific heat at constant pressure (J/kg-K)

D^e - effective diffusion coefficient (m^2/s)

D_{ij} - Stefan-Maxwell diffusion coefficient of species ij pair (m^2/s)

F - Faraday constant (96487 C/mole)

h - heat transfer coefficient (W/cm^2-K)

$i_{j0,ref}$ - exchange current density for reaction j (A/m^2)

I - total current density (A/cm^2)

k_T - thermal conductivity (J/m-s-K)

k - permeability (m^2)

M_i - molecular weight of species i (kg/mole)

m - mass of cell (kg)

N_i - molar flux of species i ($moles/m^2$-s)

n_j - electrons transferred in reaction j

p - pressure (N/m^2)

Q - heat source term in energy equation (W/m^3)

R - gas constant (8.314 J/mole-K)

$\bar{S}_i$ - partial molar entropy of species i (J/mole-K)

s_{ij} - stoichiometric coefficient of species i in reaction j

T_a - ambient temperature (K)

T_o, T^o - initial temperature (K)

t - discharge time (s)

t_i^c - transference number of species i with respect to common ion velocity

U_0 - open-circuit cell potential (V)

$U_{j,o}$ - theoretical open circuit potential of reaction j (V)

$\boldsymbol{u}$, u^o - superficial mass average velocity, initial velocity (m/s)

V - total cell potential (volts)

$\bar{V}_i$, $\tilde{V}_i$ - partial molar volume of species i (m^3/mole)

x_{ko} - mole fraction of species k at the electrode surface

x_i, x_i^o - mole fraction of species i, initial mole fraction of species i

$x_{i,k}$ - value of x_i at node k

z_i - charge number of species i

α_{aj} - anodic direction transfer coefficient of reaction j

α_{cj} - cathodic direction transfer coefficient of reaction j

β_{kj} - effective reactor order of species k in reaction j

γ_A - activity coefficient of salt A

γ_i - activity coefficient of species i

ε, ε^o - porosity or electrolyte volume fraction, initial porosity

σ - electrode-phase conductivity in electrode ($\Omega^{-1}m^{-1}$)

κ - effective ionic electrolyte conductivity ($\Omega^{-1}m^{-1}$)

μ - viscosity (kg/m-s)

ν_1^A - stoichiometric coefficient of species 1 in salt A

ψ_k - local finite-element basis function of node k

Φ_1 - electrical potential in solid electrode

Φ_2 - electrical potential in liquid electrolyte

$\Phi_{1,k}$ - value of Φ_1 at node k

$\Phi_{2,k}$ - value of Φ_2 at node k

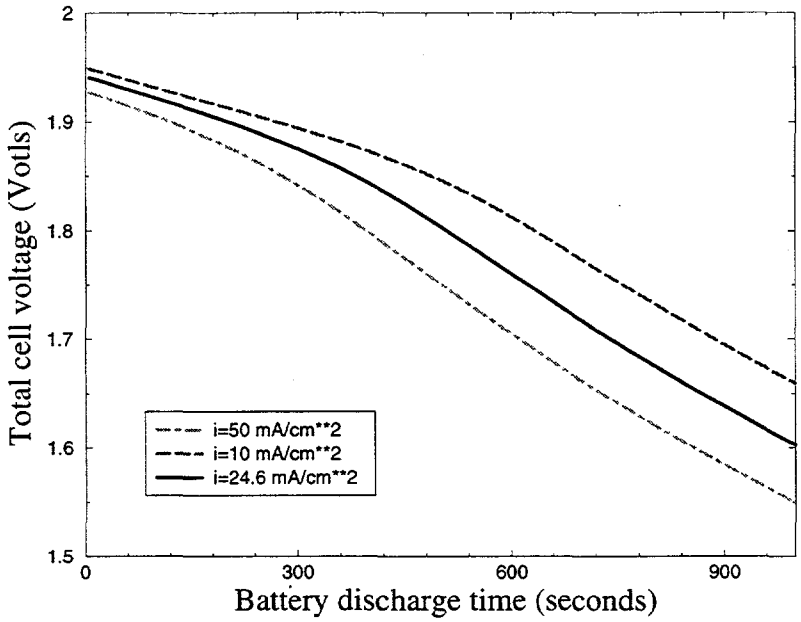

Figure 2.23 Effect of cell current density on discharge cell voltage (other parameters are those listed in Table 2.1)

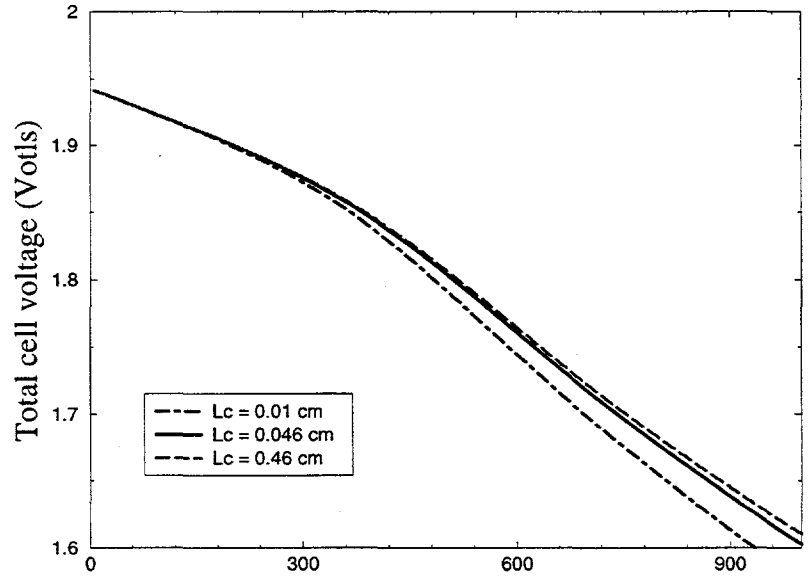

Figure 2.24 Effect of cathode thickness on discharge cell voltage (other parameters are those listed in Table 2.1)

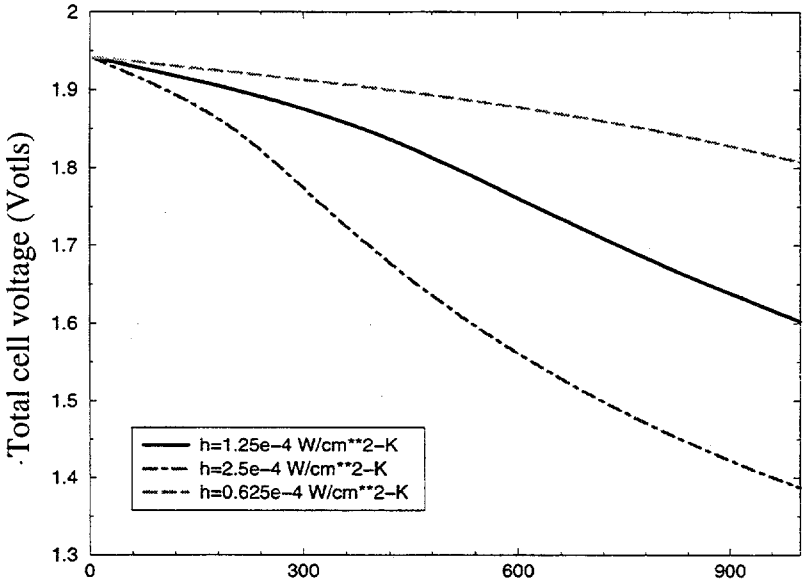

Figure 2.25 Effect of heat transfer coefficient on discharge cell voltage (other parameters are those listed in Table 2.1)

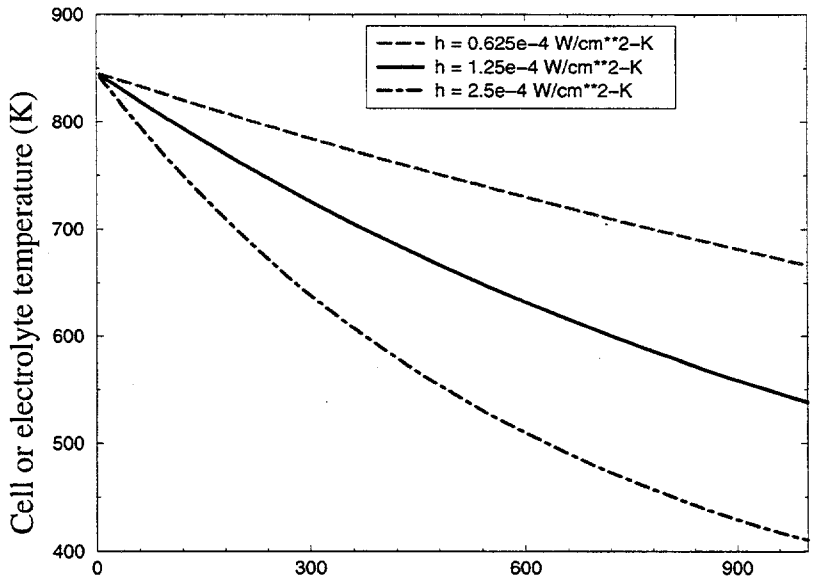

Figure 2.26 Effect of heat transfer coefficient on cell temperature (other parameters are those listed in Table 2.1)

3. CONDENSED-PHASE ENHANCEMENTS TO CHEMKIN

The Chemkin and Surface Chemkin software packages developed at Sandia are widely used in the solution of chemically reacting flow problems. The original Chemkin is applicable to (ideal) gas-phase processes such as those occurring in flames, while Surface Chemkin is designed to handle gas-surface interactions of the type found in, for example, chemical vapor deposition. In order to deal with systems involving condensed phases, and in particular those involving electrochemistry, one might wish to have available a corresponding version of Chemkin. Actually, the formalisms adopted in Surface Chemkin are sufficiently general that it can be adapted for this purpose, especially if one makes use of the multiple materials capability. Therefore, it is not necessary to develop an entirely separate software package. On the other hand, it *is* necessary to supply routines that deal with features that are specific to condensed phases; these include, but are certainly not limited to, various kinds of nonideal solution behavior, potential-dependent electrode kinetics, and vastly different transport properties. In this section we discuss the development and current status of a new Liquid Chemkin package that is designed to provide this capability. Even though a fair amount has been accomplished, the evolution of this package is ongoing and can be expected to continue indefinitely as new kinds of condensed phase behavior are added. As suggested above, the program is subsidiary to Surface Chemkin, just as the latter can be run only in conjunction with gas-phase Chemkin. Each package has its own Interpreter and subroutine library, and the capabilities of any or all of them may be needed in order to model a particular situation.

It should be mentioned at the outset that part of the capability for dealing with condensed phases has been incorporated into Surface Chemkin rather than being made a part of the new package. This has been done only if significant economies in coding would result. These features will be considered first, after which the Liquid Chemkin package itself will be described. This documentation is not intended to serve as a complete user's manual, but it should allow an experienced Chemkin user to understand how Liquid Chemkin can be employed.

3.1 Enhancements to the Surface Chemkin Interpreter

Even when only condensed phases are being considered, the Surface Chemkin Interpreter is to be used to process the phase and species declarations, thermodynamic data, and chemical reaction mechanism(s). However, since different phases will in general exhibit different kinds of thermodynamic and transport characteristics, a method is needed to make this known to the Interpreter. This is done by declaring for each phase a number (possibly zero) of "formulations", using the keyword FORM and a slash-delimited formulation type (which is case-insensitive and may be truncated to three letters). For example, if activity coefficients for the phase are to be computed from the Debye-Hückel theory, then one line in the Interpreter input file might be

```
BULK/SOLUTION/ FORM/Debye-Huckel/
```

Each valid formulation is associated with a subroutine in the Liquid Chemkin library which will perform the necessary computations when the property in question is requested. Multiple formulations can be used for a given phase if they refer to different properties, but formulations corresponding to the same property are mutually exclusive. At present only three formulations have been implemented, all dealing with activity coefficients (nonideal solution behavior): 'Debye-Huckel', 'Regular', and 'Series'; these will be discussed later in detail. Formulations for various transport properties are expected to be added in the near future.

The activity coefficient γ for a particular species in a bulk mixture is ordinarily defined with respect to one of two principal conventions: the standard state can be either the pure component (unit mole fraction) or a hypothetical ideal solution of unit molality (moles of solute per kg of solvent). The choice of convention is made known to the Surface Chemkin Interpreter through the species declarations. If the keyword SOLV appears with one of the species names, then the mole fraction convention is used for that species (the solvent, which must appear last), and the molality convention is used for all other species *in that phase*. Note that the need to compute molalities is the *only* reason for declaring a solvent. If there is no such declaration, then the mole fraction convention is used for all species in the phase. As one example, an aqueous solution of $AgNO_3$ and $Cu(NO_3)_2$ might be presented to the Interpreter as follows:

```
BULK/SOLUTION/ FORM/Debye-Huckel/
CU(+)2(AQ)
NO3(-)(AQ)
AG(+)(AQ)
H2O(L)/SOLV/ /1.0/
END
```

As usual, the number 1.0 following the H_2O declaration refers to the species density.

The handling of chemical reactions by the Interpreter has been enhanced by allowing for electrode processes that obey Butler-Volmer kinetics. (The mathematical details will be given below in the description of the corresponding library routine.) This is best illustrated by means of an example: for the oxidation of copper to cupric ions in aqueous solution, one might have

```
CU(S) = CU(+)2(AQ) + 2ELEC          3.000E-03      0.0      0.0
TRAN / 0.75  0.25 /
OPVOLT / 0.3395 /
```

The three Arrhenius parameters following the reaction represent not a rate constant, but rather the standard state exchange current density, which is understood to be given in A/cm^2. Accompanying the keyword TRAN are the anodic and cathodic transfer coefficients; they must be listed in this order, regardless of the direction in which the reaction is written. The keyword OPVOLT signifies the standard state open circuit potential in Volts; alternatively, one can use the keyword OPERGC to give the value in erg/C, which is an unconventional unit but which is actually the one used internally by Surface Chemkin. (The use of cgs rather than SI units in the Chemkin suite appears rather unfortunate when electrochemical features are added.) More generally, if one wishes to define a temperature-dependent open circuit potential, then one can provide the two parameters a and b in the linear expression $a + bT$, where T is in Kelvins. The decision to supply an open circuit potential is optional; if neither OPVOLT nor OPERGC is used, then the necessary value is calculated internally from the thermodynamic data for the species involved in the reaction.

The string ELEC appearing in the reaction is actually a reserved keyword that denotes an electron being transferred; it is *not* a declared species, because the electron does not exist in free form (as it does, for example, in a plasma). Thus, the electron is excluded from the composition vector for the bulk phase and from the mass-action expression for the reaction kinetics, as it should be. However, its contribution to the free energy change for the reaction cannot be ignored, because it has a nonzero standard state entropy, even though its standard heat of formation is defined to be zero. This dilemma has been resolved by requiring that the electron be declared in the Chemkin Interpreter as a *gas phase* species, but with a standard entropy appropriate to the electrode reaction(s) in question

(15.6 cal/mol · K for processes in aqueous solution, as opposed to the value of 4.98 cal/mol · K from the Chemkin data base). Surface Chemkin is programmed to seek and use this value in the necessary free energy calculations. This procedure is clearly an artifice, but it should not cause problems unless one wishes to deal simultaneously with plasmas and condensed phase electrode reactions—a highly unlikely eventuality.

3.2 Enhancements to the Surface Chemkin subroutine library

Several routines in the Surface Chemkin subroutine library have been added or modified in order to implement some of the features discussed above. (The other features are covered by Liquid Chemkin.) Some descriptive and background information on these routines will now be given.

SKMTX and SKXTM: These routines convert from molalities m_k to mole fractions x_k, and vice versa, for a given phase. These simple transformations can be carried out only if a solvent s has been identified. For SKMTX the formulas are

$$x_k = m_k \left(\frac{1000}{W_s} + \sum_{k \neq s} m_k \right)^{-1} \quad , \quad k \neq s \tag{3.1}$$

and

$$x_s = \left(1 + \frac{W_s}{1000} \sum_{k \neq s} m_k \right)^{-1} \tag{3.2}$$

where W is the molecular weight. On the other hand, SKXTM uses

$$m_k = \frac{1000\, x_k}{x_s W_s} \tag{3.3}$$

The molality of the solvent is not normally considered to be a useful or relevant quantity, but Eq. (3.3) actually gives a valid result for this species.

SKSOLV: This simply returns the species index (if any) for the solvent in each phase.

SKRRPT: This is an existing core routine (not normally called by the user) that calculates the forward and reverse mass-action rate constants k_f and k_r for a variety of different kinds of reactions. It has now been augmented to handle electrode reactions, using a reformulated version of the standard Butler-Volmer equation. For a reaction written in the anodic direction, the expressions used are

$$k_f = \frac{i_0^0}{n_e F} \exp\left[\frac{\alpha_a}{RT} \left(n_e F \Delta\Phi - \Delta G^0 \right) \right] \psi(p_j) \tag{3.4}$$

and

$$k_r = \frac{i_0^0}{n_e F} \exp\left[\frac{-\alpha_c}{RT} \left(n_e F \Delta\Phi - \Delta G^0 \right) \right] \psi(q_j) \tag{3.5}$$

Here i_0^0 is the standard state exchange current density (calculated from the three Arrhenius parameters supplied by the user), n_e is the signed stoichiometric coefficient of the electron (positive for an anodic reaction), F is Faraday's constant, α_a and α_c are the anodic and cathodic transfer coefficients, $\Delta\Phi$ is the surface potential (an input property, like the temperature T), and ΔG^0 is the

standard free energy change for the reaction as written. ΔG^0 is calculated either from the specified open circuit potential,

$$\Delta G^0 = n_e F \Delta \Phi_e^0 \tag{3.6}$$

or, in the absence of any specification, from thermodynamic data for the species. Finally, $\psi(p_j)$ is a correction factor defined by

$$\psi(p_j) = \left(\frac{P_{\text{atm}}}{RT}\right)^{-\sum_{j=1}^{K_g} p_j} \prod_{n=N_s^f}^{N_s^l} \left(\Gamma_n^0\right)^{-\sum_{j=K_s^f(n)}^{K_s^l(n)} p_j} \prod_{j=K_s^f(n)}^{K_s^l(n)} [\sigma_j(n)]^{p_j} \tag{3.7}$$

the p_j being the *unsigned* stoichiometric coefficients (or reaction orders) for the reactants in the anodic direction. $\psi(q_j)$ is defined in exactly the same way and refers to the cathodic direction. Equation (3.7) is similar to Eq. (37) in the Surface Chemkin manual (Coltrin et al., 1996), which should be consulted for the meaning of the rest of the notation.

If the reaction in question is written in the cathodic direction, then $n_e < 0$, and the appropriate equations for the rate constants are

$$k_f = \frac{-i_0^0}{n_e F} \exp\left[\frac{-\alpha_c}{RT}\left(-n_e F \Delta\Phi + \Delta G^0\right)\right] \psi(q_j) \tag{3.8}$$

and

$$k_r = \frac{-i_0^0}{n_e F} \exp\left[\frac{\alpha_a}{RT}\left(-n_e F \Delta\Phi + \Delta G^0\right)\right] \psi(p_j) \tag{3.9}$$

Note that p_j and q_j still refer to the anodic and cathodic directions, respectively.

SKFARD: This returns the value of Faraday's constant, 96486.7 C/mol.

SKSPOT: This routine allows the user to insert a value for the surface potential $\Delta\Phi$ into the Surface Chemkin work array, from which it can be accessed by SKRRPT. The purpose of this device is to eliminate the need to add $\Delta\Phi$ to the call lists of SKRRPT and those routines that access it. Such changes should obviously be avoided whenever possible.

3.3 The Liquid Chemkin Interpreter

The purpose of the Liquid Chemkin Interpreter is to read, check, and store data relating to the various "formulations" declared in the Surface Chemkin input file. Thus, the input to Liquid Chemkin is basically a user-supplied physical property data base for the problem in question. Ideally, the user could draw upon one comprehensive data base to solve a multitude of problems, just as is done with the Chemkin transport package. This may indeed be possible in the future, but Liquid Chemkin must first be developed to a much higher level.

Each line in the Liquid Chemkin input file refers to a particular species and to a particular formulation. Of course, a species may appear on several different lines if there are multiple formulations. As one example, we can consider the following input file for the $AgNO_3/Cu(NO_3)_2$ solution alluded to earlier:

```
H2O(L) Debye/1.3874 -0.003361 8.8911e-6 0.30163 2.6839e-5 2.1348e-7 4.6/
CU(+)2(AQ)    Ion / 6.0 /
NO3(-)(AQ)  Ion / 3.0 /
```

```
AG(+)(AQ) Ion / 2.5 /
```

Each record consists of a species name, a keyword, and a slash-delimited set of parameters (separated by spaces). Each keyword refers to a specific formulation type; in this case, 'Debye' and 'Ion' (case-insensitive) both refer to the 'Debye-Huckel' formulation, the difference being that the former is used for the solvent and the latter is used for all of the solutes. The first six parameters for the solvent are expansion coefficients A_0, A_1, A_2, B_0, B_1, and B_2 to be defined below, while the last parameter is an overall effective ionic radius for the solutes in Angstroms. The lone parameter for each solute is its individual effective ionic radius, also in Angstroms.

At present, the Liquid Chemkin Interpreter is programmed to recognize two other keywords, namely 'Regular' and 'Series'; these obviously correspond to the two remaining formulations mentioned earlier. They might be used as follows:

```
! Regular solution
C6H6     Regular / 59500.   89. /
C6H12    Regular / 53000.  109. /
C6H14    Regular / 47200.  132. /
! Molten salt electrolyte
LICL(L) Series / KCL(L)  0. -21864.  145900. -361320.  362000. -126260. /
KCL(L)  Series / LICL(L) 0.   2619.2 -77534.  209000. -204850.   69674. /
```

The two parameters for a component of a regular solution are the solubility parameter δ_k in $(\text{erg/cm}^3)^{1/2}$ and the liquid molar volume v_k in cm^3/mol. The 'Series' case is more complicated, because here the parameters for a given species depend upon the identities of the other species present in the phase. For this reason, the 'Series' formulation is presently restricted to binary mixtures. The first parameter for a species A is the identity of the other species B, and the six numbers are coefficients in a series expansion of $T \ln \gamma_A$ in powers of x_B. Again, the precise definition will be given below.

3.4 The Liquid Chemkin subroutine library

The main purpose of the Liquid Chemkin subroutine library is to carry out computations specific to each of the formulations that have been defined. There are also many higher-level routines that use the results of the basic computations to return auxiliary quantities that may be of greater interest to the user. Some information on the major routines will now be presented.

LKDEB: This core routine calculates the activity coefficients γ_k (and their temperature derivatives) for all of the species in a Debye-Hückel phase (an electrolyte solution). For each solute, the equation used is

$$\ln \gamma_k = \frac{-A(T) z_k^2 I^{1/2}}{1 + B(T) r_k I^{1/2}} \tag{3.10}$$

where z_k is the ionic charge, r_k is the effective ionic radius mentioned above, and I is the total ionic strength of the solution:

$$I = \frac{1}{2} \sum_{k \neq s} m_k z_k^2 \tag{3.11}$$

$A(T)$ and $B(T)$ are functions characteristic of the solvent, and they are here represented by simple power series expansions, using the coefficients supplied to the Interpreter:

$$A(T) = A_0 + A_1 T + A_2 T^2 \tag{3.12}$$

$$B(T) = B_0 + B_1 T + B_2 T^2 \tag{3.13}$$

The activity coefficient of the solvent is given by the following relation, which can be obtained from the Gibbs-Duhem equation after assuming that each of the radii r_k can be replaced by a single average value r:

$$1000 \ln(\gamma_s x_s) + W_s \sum_{k \neq s} (m_k \ln \gamma_k + m_k) = \frac{-4 W_s A}{Br} \left[\frac{1}{2} I - \frac{I^{1/2}}{Br} + \frac{1}{B^2 r^2} \ln(1 + BrI^{1/2}) \right] \tag{3.14}$$

LKREG: This uses the Scatchard-Hildebrand theory (Prausnitz, 1969) to compute the activity coefficients for all species in a regular solution. The basic equation is

$$\ln \gamma_k = \frac{v_k}{RT} (\delta_k - \bar{\delta})^2 \tag{3.15}$$

where

$$\bar{\delta} = \frac{\sum_k x_k v_k \delta_k}{\sum_k x_k v_k} \tag{3.16}$$

When dealing with a binary mixture, one occasionally has a need for the composition derivative $d \ln \gamma_A / d \ln x_A$. For a regular solution, the result is simply

$$\frac{d \ln \gamma_A}{d \ln x_A} = \ln \gamma_A \cdot \frac{-2 x_A v_A}{x_B (x_A v_A + x_B v_B)} \tag{3.17}$$

LKSER: This routine evaluates power series representations for the activity coefficients, and, as noted above, it applies only to binary mixtures. Assuming that expansion coefficients c_n have been provided for species A, one has

$$\ln \gamma_A = \frac{1}{T} \sum_{n=2}^{7} c_n x_B^n \tag{3.18}$$

According to the Gibbs-Duhem equation, the activity coefficient of species B is then given by

$$\ln \gamma_B = \ln \gamma_A + \frac{1}{T} \sum_{n=2}^{7} \frac{c_n}{n-1} \left(1 - n x_B^{n-1} \right) \tag{3.19}$$

The truncation of the series in Eq. (3.18) after $n = 7$ is completely arbitary; however, c_0 is omitted in order to satisfy the condition that $\gamma_A = 1$ when $x_B = 0$, and c_1 is omitted in order to avoid creating a logarithmic singularity in Eq. (3.19) at that point. Nevertheless, if expansion coefficients have been provided for both species, then Eq. (3.19) is not used; instead, Eq. (3.18) (with obvious changes in notation) is used for species B as well.

From Eq. (3.18), the derivative $d \ln \gamma_A / d \ln x_A$ is given by

$$\frac{d \ln \gamma_A}{d \ln x_A} = \frac{x_B - 1}{T} \sum_{n=2}^{7} n c_n x_B^{n-1} \tag{3.20}$$

In theory, $d \ln \gamma_B / d \ln x_B$ has the same value, and this is precisely true if Eq. (3.19) is used. However, if coefficients are specified for both species, then the two derivatives may not be equal (implying a thermodynamic inconsistency), and the two results should therefore be averaged before being used.

LKSTMX2: This is a rather specialized routine whose purpose is to return transport properties for a molten salt. Specifically, it is designed to calculate the three binary Stefan-Maxwell coefficients in a mixture of two 1-1 molten salts with a common ion. However, the computations are not really predictive, but instead use three experimentally accessible transport properties as inputs. Let us suppose that salt A contains ions 1 and 3, while salt B contains ions 2 and 3. The three required inputs are then the electrical conductivity κ of the mixture, the transference number t_1^c of ion 1 relative to the common ion velocity, and the effective salt diffusivity D based on a mole fraction driving force. The first step is to determine the diffusivity $\mathcal{D}$ based on a thermodynamic (chemical potential) driving force:

$$\mathcal{D} = D \left(1 + \frac{d \ln \gamma_A}{d \ln x_A} \right)^{-1} \tag{3.21}$$

the derivative typically being obtained from a call to LKSER, using the above-mentioned averaging if necessary. The Stefan-Maxwell coefficients are then given by

$$\frac{1}{\mathcal{D}_{12}} = -\frac{2F^2 c}{RT\kappa} + \frac{2t_1^c t_2^c}{\mathcal{D} x_A x_B} \tag{3.22}$$

$$\frac{1}{\mathcal{D}_{13}} = \frac{2F^2 c}{RT\kappa} - \frac{2t_2^c}{\mathcal{D} x_A} \left(1 - \frac{t_2^c}{x_B} \right) \tag{3.23}$$

$$\frac{1}{\mathcal{D}_{23}} = \frac{2F^2 c}{RT\kappa} - \frac{2t_1^c}{\mathcal{D} x_B} \left(1 - \frac{t_1^c}{x_A} \right) \tag{3.24}$$

where $t_2^c = 1 - t_1^c$ and c is the total concentration of salts A and B. Note that this routine does not rely on any input to the Liquid Chemkin Interpreter.

LKACOF: This routine returns activity coefficients for all of the species in all of the phases, using calls to core routines such as LKDEB to do the actual calculations. If no appropriate formulation has been declared for a given phase, then the activity coefficients for that phase default to unity.

LKDLNG: This is similar to LKACOF but returns $\partial \ln \gamma_k / \partial T$ instead of γ_k. In this case the default value is zero.

LKD2LNG: This returns $\partial^2 \ln \gamma_k / \partial T^2$ for every species, again defaulting to zero.

LKDLNGX: This returns the two values $d \ln \gamma_A / d \ln x_A$ and $d \ln \gamma_B / d \ln x_B$ for each binary phase. As noted above, the two values should be equal if the Gibbs-Duhem equation is to be obeyed, but deviations from this can arise with some formulations. The default values are zero.

LKXTA: This routine converts a vector of mole fractions (or, in the case of surface species, site fractions) for all species to a vector of activities, with the effects of nonideality potentially included for all of the phases. The activity a_k of species k is given by either

$$a_k = \gamma_k x_k \tag{3.25}$$

or

$$a_k = \gamma_k m_k \tag{3.26}$$

depending upon whether the mole fraction convention or the molality convention is being used.

LKXTCZ: This is a generalization of the Surface Chemkin routine SKATCZ. It converts a vector of mole fractions (or, in the case of surface species, site fractions) to a vector of concentrations (or, in the case of bulk species, activities) for use in the rate expressions. It differs from SKATCZ only in that it treats bulk species just as does LKXTA, whereas SKATCZ leaves the inputs for the bulk species unchanged.

LKHML: This returns the partial molar enthalpy H_k of each species. Basically, it generalizes the Surface Chemkin routine SKHML by correcting for nonideality according to

$$H_k = H_k^0 - RT^2 \frac{\partial \ln \gamma_k}{\partial T} \tag{3.27}$$

LKCPML: This returns the partial molar heat capacity C_{p_k} of each species, building upon the Surface Chemkin routine SKCPML. The relevant equation is

$$C_{pk} = C_{pk}^0 - RT^2 \frac{\partial^2 \ln \gamma_k}{\partial T^2} - 2RT \frac{\partial \ln \gamma_k}{\partial T} \tag{3.28}$$

LKSML: This returns the partial molar entropy S_k of each species, calculated from

$$S_k = S_k^0 - RT \frac{\partial \ln \gamma_k}{\partial T} - R \ln a_k \tag{3.29}$$

An important distinction between LKSML and the Surface Chemkin routine SKSML should be noted here. Whereas SKSML returns the *standard state* entropy for each species, the values returned by LKSML are partial molar quantities that also include a contribution from the entropy of mixing (as well as any effects of nonideality). The weighted sum of these values over a given phase then provides the average entropy $\overline{S}$ for the phase directly. In Surface Chemkin, on the other hand, the entropy of mixing must be included explicitly in the calculation of $\overline{S}$.

LKHMS, LKCPMS, LKSMS: These simply re-express the corresponding partial molar quantities in mass units.

LKHORT, LKCPOR, LKSOR: These return the dimensionless properties H_k/RT, C_{p_k}/R, and S_k/R.

LKHBML, LKCPBL, LKSBML: These return the molar-average thermodynamic properties $\overline{H}$, $\overline{C}_p$, and $\overline{S}$ for each phase. $\overline{H}$, for example, is computed from

$$\overline{H} = \sum_k x_k H_k \tag{3.30}$$

LKHBMS, LKCPBS, LKSBMS: These routines express the phase averages on a mass basis. This is equivalent to saying that they return mass-average properties, because

$$(\overline{W})^{-1} \sum_k x_k H_k = \sum_k Y_k \frac{H_k}{W_k} \tag{3.31}$$

where the Y_k are mass fractions.

LKIRAD: This routine provides the effective ionic radii that were declared to the Interpreter. Of course, this is not relevant to all of the species, and the default value is set to zero even for ions.

LKINIT: This is the Liquid Chemkin initialization routine. It reads the linking file created by the Interpreter and sets up the integer, real, and character work arrays. As with Chemkin and Surface Chemkin, the initialization routine must be called before the other routines in the library can be used.

4. ESTIMATION OF STEFAN-MAXWELL DIFFUSION COEFFICIENTS FOR LIQUID PHASE PROCESSES

4.1 Introduction

Diffusion may be defined (Newman, 1991, p. 269) as the motion of species relative to the bulk fluid motion as a result of nonuniform thermodynamic potentials. In a binary system (species 1 and 2) diffusion due to concentration gradients (sometimes called ordinary diffusion to distinguish it from thermal diffusion, pressure diffusion, and forced diffusion caused by e.g. gradients in the electrical potential) is described by Fick's first law which serves to define the binary diffusion coefficient, $\mathcal{D}_{12}$, and which relates the diffusion flux of a species to its concentration gradient (Bird et al., 1960, p. 502, Table 16.2-1, Eqn. E):

$$\boldsymbol{J}_1 = c_1(\boldsymbol{v}_1 - \boldsymbol{v}) = -\frac{c^2}{\rho} M_2 \mathcal{D}_{12} \nabla x_1 \,. \tag{4.1}$$

In Equation (4.1) $\boldsymbol{J}_1$ is the molar diffusion flux of species 1 relative to the mass average velocity of the mixture, $\boldsymbol{v}$; c_1 is the molar concentration of species 1; $\boldsymbol{v}_1$ is the average velocity of species 1; c is the molar concentration of the mixture; ρ is the mass density of the mixture; M_2 is the molar mass of species 2; x_1 is the mole fraction of species 1. Note that the diffusion flux is specified relative to a frame of reference (in this case the mass average velocity of the mixture) whereas the binary diffusion coefficient is independent of the reference frame. There are several versions of Fick's first law (cf. Table 16.2-1, Bird et al., 1960, p. 502) depending on the chosen reference frame and the chosen flux quantity (mass, moles, etc.); however all the expressions have the same diffusion coefficient $\mathcal{D}_{12}$ and can be derived from the expression for the mass diffusion flux relative to the mass average velocity, $\boldsymbol{j}_1$:

$$\boldsymbol{j}_1 = \rho_1(\boldsymbol{v}_1 - \boldsymbol{v}) = -\rho \mathcal{D}_{12} \nabla Y_1 \tag{4.2}$$

where Y_1 is the mass fraction of species 1. According to Mills (1995, Ch. 9, p. 818), Equation (4.2) is shown from kinetic theory of gases to be an appropriate form of Fick's first law for binary gas mixtures and dilute liquid and solid solutions.

In general, however, when species 1 is not a dilute species, the mixture may be nonideal, and the driving force for diffusion is the gradient of chemical (or electrochemical) potential $\nabla\mu_1$. For constant temperature and pressure and no gradient of the electrical potential, the chemical potential gradient of species 1 is given by (Guggenheim, 1967):

$$\nabla\mu_1 = \frac{RT}{x_1}\left[1+\frac{\partial \ln \gamma_1}{\partial \ln x_1}\right]\nabla x_1 \tag{4.3}$$

where γ_1 is the activity coefficient of species 1. It can be shown from the Stefan-Maxwell Equations (4.8) (shown below) for a binary system that

$$J_1 = -\frac{c^2}{\rho} M_2 D_{12}\left[1+\frac{\partial \ln \gamma_1}{\partial \ln x_1}\right]\nabla x_1 . \tag{4.4}$$

In comparing Equations (4.1) and (4.4) the relation between the binary diffusion coefficient $\mathcal{D}_{12}$ and the Stefan-Maxwell diffusion coefficient D_{12} is:

$$\mathcal{D}_{12} = D_{12}\left(1+\frac{\partial \ln \gamma_1}{\partial \ln x_1}\right) \tag{4.5}$$

as pointed out by Lightfoot et al. (1962) and also noted by Danckwerts (1971), Newman (1991), pp. 63-64 and p. 268, Taylor and Krishna (1993), pp. 23-26, and Wesselingh and Bollen (1997). The binary diffusion coefficient $\mathcal{D}_{12}$ in a binary liquid solution can be strongly concentration dependent and usually increases with temperature; typical binary diffusion coefficient variations with composition are 30% to more than 100% (Bird et al., 1960, p. 504). In most cases the experimental diffusion coefficient reported in the literature is the binary diffusion coefficient $\mathcal{D}_{12}$; determining the Stefan-Maxwell diffusion coefficient D_{12} requires information on the activity coefficient γ_1. In some binary systems the Stefan-Maxwell coefficient D_{12} is less concentration dependent (Wesselingh and Krishna, 1991, Ch. 9; Bird et al., 1960, Ch. 18, Fig. 18.4-2) but this is not always the case (Rutten, 1992, Appendix B). It is noted that Fick's first law may also be valid for mixtures or solutions of more than two species if species 1 is a minor constituent (e.g., a trace species in a mixture or a dilute solute species in a liquid solution in which the interactions are primarily between the solute species and the solution such that the flux of species 1 depends only on its own concentration gradient and not on the gradients of any other species in the mixture or solution).

In general, in a multicomponent system the diffusion flux of any one species due to concentration gradients depends in a complex way on concentration and concentration gradients of the other species (Bird et al., 1960, p. 567):

$$J_i^{(c)} = \frac{c^2}{\rho RT} \sum_{j=1}^{n} M_j D_{ij} \left(x_j \sum_{\substack{k=1 \\ k \neq j}}^{n} \left(\frac{\partial \overline{G}_j}{\partial x_k} \right)_{T,p,x_{s \neq j,k}} \nabla x_k \right) \tag{4.6}$$

where $\overline{G}_j$ is the partial molal Gibbs free energy of species j; the D_{ij} are the multicomponent diffusion coefficients; $J_i^{(c)}$ is the (concentration gradient) molar diffusion flux of species i relative to the mass average velocity. Note that $D_{ii} = 0$ and $D_{ij} \neq D_{ji}$ in general (however, in a binary system $D_{12} = D_{21}$). Noting that

$$\left(\frac{\partial \overline{G}_j}{\partial x_k} \right)_{T,p,x_{s \neq j,k}} = RT \left(\frac{\partial \ln(\gamma_j x_j)}{\partial x_k} \right)_{T,p,x_{s \neq j,k}} \tag{4.7}$$

Equation (4.6) reduces to Equation (4.4) for a binary system where $D_{12} = D_{12}$ (the multicomponent diffusion coefficient D_{12} and the Stefan-Maxwell diffusion coefficient D_{12} are equal in the binary system).

In a multicomponent system, there are several disadvantages to the diffusion flux formulation of Equation (4.6) that arise from the nature of the multicomponent diffusion coefficients D_{ij}. First, theoretical expressions for D_{ij} are available only for gas mixtures (the complex calculations necessary to evaluate the kinetic theory of gas expressions make the evaluation of the fluxes in Equation (4.6) costly compared with the Stefan-Maxwell approach discussed below; see Dixon-Lewis, 1968); second, there is no simple physical interpretation for the D_{ij} values; third, the multicomponent diffusion coefficients are dependent on concentration and the choice of velocity to which diffusion is relative (mass averaged velocity, molar averaged velocity, volume averaged velocity, etc); fourth, since they are not symmetric ($D_{ij} \neq D_{ji}$), there are $n(n\text{-}1)$ independent coefficients in an n component system (n>2); and fifth, since $D_{ii} = 0$, the diffusion flux of species i given by Equation (4.6) does not depend explicitly on the concentration (or mole fraction) gradient of species i (this can severely degrade the convergence charac-

teristics of some common iterative numerical schemes that solve the species conservation equations; see Coltrin et al., 1986).

Alternatively, diffusion in multicomponent liquid mixtures can be described by the Stefan-Maxwell equations (these equations are often referred to as the Maxwell-Stefan equations; see e.g., Wesselingh and Krishna, 1991) relating the diffusion fluxes (mass or molar) of the species to the driving forces for diffusion (Lightfoot et al., 1962), which in an isothermal, isobaric system of charged and/or uncharged species, consist of gradients of electrochemical potentials :

$$\frac{x_i}{RT}\nabla\mu_i = \sum_{j\neq i}\frac{x_i\boldsymbol{J}_j - x_j\boldsymbol{J}_i}{cD_{ij}} \tag{4.8}$$

In Equation (4.8), $\nabla\mu_i$ is the gradient of electrochemical potential of species i; and D_{ij} is the Stefan-Maxwell diffusion coefficient of the species (i, j) pair (see Chen et al., 1998). Note that although the molar diffusion fluxes with respect to the mass average velocity have been used, the fluxes in Equation (4.8) can be relative to any frame of reference; this is because *differences* in fluxes (actually velocities) appear in this equation.

Some advantages of using the Stefan-Maxwell formulation (Lightfoot et al., 1962; Riede and Schlünder, 1991, p. 611; Krishna and Wesselingh, 1997, p. 869; Pinto and Graham, 1986; Graham and Dranoff, 1982) compared with the diffusion flux formulation given in Equation (4.6) include (a) a more physical interpretation of the coefficients D_{ij} (inverses of binary interaction drag coefficients), (b) independence of the velocity reference frame, (c) less concentration-dependent coefficients in some cases, (d) fewer coefficient evaluations since $D_{ij} = D_{ji}$, and (e) in the case of electrolyte mixtures, coefficients that are less dependent on other ions present in the system. In this memo we describe our approach for determining the Stefan-Maxwell diffusion coefficients for three types of liquid mixtures: (1) multicomponent liquid mixtures of neutral species, (2) multicomponent liquid mixtures of charged species in a solvent including ion-ion and ion-solvent interactions, and (3) multicomponent liquid mixtures of molten salts.

4.2 Mixtures of Neutral Species

4.2.1 Binary Mixtures

Theories of diffusion in liquids are not as well developed as is the kinetic theory of gases. An early theory of diffusion in liquids is the hydrodynamical theory based on the Nernst-Einstein equation which was developed to describe Brownian motion (particle motion in liquids; see Mills, 1995, ch. 9, p. 895):

$$D_{12} = \frac{kT}{f_{12}} \tag{4.9}$$

where f_{12} (defined as the force required to give species 1 a speed of unity,i.e., force per unit speed) is the friction coefficient of a solute (designated species 1) in a solvent (designated species 2), k is the Boltzmann constant, and T is the temperature. Assuming creeping (Stokes) flow, the Stokes-Einstein equation for diffusion of species 1 in species 2 is obtained:

$$D_{12} = \frac{kT}{6\pi\eta_2 R_1} \tag{4.10}$$

where η_2 is the viscosity of the pure liquid solvent and R_1 is the radius of the diffusing solute particle or molecule. Equation (4.10) was developed for large spherical particles in a liquid solution; it must be modified to give reasonable agreement with measured values of binary diffusion coefficients in liquids. A recent modification due to Rutten (1992) is more accurate for similar sized molecules :

$$D_{12}^{x_2 \to 1} = \frac{kT}{4\pi\mu_2 R_1^2 / R_2} \tag{4.11}$$

where R_2 is the radius of the solvent species; similarly when species 1 is the solvent and species 2 is the solute then the analogous formula (Wesselingh and Bollen, 1997) is:

$$D_{21}^{x_1 \to 1} = \frac{kT}{4\pi\eta_1 R_2^2 / R_1} \quad . \tag{4.12}$$

An empirical modification of the Stokes-Einstein Equation (4.10) is the Wilke-Chang

formula for dilute solute species 1 in solvent species 2 (Reid et al., 1987, p. 598):

$$D_{12}^{x_2 \to 1} = \frac{7.4 \times 10^{-8} (\phi M_2)^{1/2} T}{\eta_2 \tilde{V}_1^{0.6}} \tag{4.13}$$

where ϕ is a dimensionless association factor for the solvent species, M_2 is the solvent molar mass in g/mole, T is the temperature in K, η_2 is the solvent viscosity in centipoises, and $\tilde{V}_1$ is the molar volume of the solute species in cm^3/mole; the units of $D_{12}^{x_2 \to 1}$ are cm^2/s. The Wilke-Chang formula was tested on more than 250 solute-solvent systems (Reid et al., 1987), and the average error was about 10%. The above Equations (4.11)-(4.13) apply when the solute species is infinitely dilute in the solvent.

A method of accounting for the effects of variable composition by linearly weighting the infinitely dilute diffusion coefficients using the mole fractions as the weighting functions is due to Darken (Reid et al., 1987, p. 611):

$$D_{12} = x_1 D_{21}^{x_1 \to 1} + x_2 D_{12}^{x_2 \to 1} \ . \tag{4.14}$$

Another method for determining the effects of composition on the diffusion coefficient is the logarithmic expression due to Vignes (1966):

$$\ln D_{12} = x_1 \ln D_{21}^{x_1 \to 1} + x_2 \ln D_{12}^{x_2 \to 1} \ . \tag{4.15}$$

Note that interchanging the indices in Equations (4.14) or (4.15) produces the same result, i.e., $D_{12} = D_{21}$.

According to Wesselingh and Bollen (1997), Equation (4.14) applies when species 1 and 2 are similar chemically and of similar size; then the diffusion coefficients at the two limits don't differ significantly, and as noted by Rutten (1992) Equations (4.14) and (4.15) yield similar results. When the species are of different size, the diffusion coefficients at the two limits do differ considerably, and Equation (4.15) is recommended. Reid et al. (1987, p. 614) recommend the use of Equation (4.15) for estimating the effect of concentration on the diffusion coefficient.

4.2.2 Multicomponent Mixtures

As pointed out in Kooijman and Taylor (1991) and Wesselingh and Bollen (1997), the Stefan-Maxwell equations are only useful for predicting diffusive transport in multicomponent liquid mixtures if the Stefan-Maxwell diffusivities D_{ij} in multicomponent liquid mixtures can be determined. Wesselingh and Krishna (1991) and Kooijman and Taylor (1991) have generalized the Vignes formula, Equation (4.15), to a multicomponent system consisting of n species:

$$D_{ij} = \prod_{k=1}^{n} \left(D_{ij}^{x_k \to 1}\right)^{x_k} \tag{4.16}$$

where $D_{ij}^{x_k \to 1}$ is calculated from:

$$D_{ij}^{x_k \to 1} = \left(D_{ik}^{x_k \to 1} D_{jk}^{x_k \to 1}\right)^{1/2} . \tag{4.17}$$

An alternative to Equation (4.16) for determining the Stefan-Maxwell diffusion coefficients in a multicomponent liquid mixture has recently been described (Wesselingh and Bollen, 1997) using free volume theory. A primary notion in the theory is that the mixture contains openings with volumes approximately equal to the molecular volume. A self diffusion coefficient $D_{i\#,i}$ is derived assuming hard spheres of equal size and density; the model uses a statistical description of free volume for spherical particles to yield:

$$D_{i\#,i} = D_{i\#,i}^{o} \exp\left(-0.7 \frac{\tilde{V}_i}{\tilde{V}_{F,i}}\right) \tag{4.18}$$

where the exponential term is the fraction of space consisting of holes larger than the molecules of species i. Equation (4.18) is for the self diffusivity in a pure substance. In a mixture, the effective self diffusion coefficient is then given by

$$D_{i\#,\text{eff}} = D_{i\#,i}^{o} \exp\left(-0.7 \frac{\tilde{V}_i}{V_{F,i}}\right) \tag{4.19}$$

where

$$D_{i\#,i}^{o} = \frac{1}{6}\sqrt{\frac{3kT}{\bar{\rho} d_i}} \tag{4.20}$$

and

$$\overline{\rho} = \sum_{i=1}^{n} x_i \tilde{\rho}_i \quad . \tag{4.21}$$

The tilde in Equations (4.18)-(4.21) denotes a pure substance property; $\tilde{V}_i$ is the molar volume of pure substance i ; $V_{F,i}$ is the free molar volume of species i in the mixture; d_i is the molecular diameter of species i. The free volume of the mixture is assumed to be the molar average of the free volumes of the pure substances, and the free volume of a single component is assumed to be proportional to the surface fraction σ_i of that component:

$$V_F = \sum_{i=1}^{n} x_i \tilde{V}_{F,i} \tag{4.22}$$

$$V_{F,i} = \frac{\sigma_i}{x_i} \mathrm{V}_F \tag{4.23}$$

where

$$\sigma_i = \frac{x_i \left(\tilde{V}_i\right)^{2/3}}{\sum_{j=1}^{n} x_j \left(\tilde{V}_j\right)^{2/3}} \quad . \tag{4.24}$$

The Stefan-Maxwell diffusion coefficients are given by:

$$D_{ij} = \frac{D_{i\#,\mathrm{eff}} D_{j\#,\mathrm{eff}}}{\left(\sum_{k=1}^{n} x_k / D_{k\#,\mathrm{eff}} \right)^{-1}} . \tag{4.25}$$

In deriving Equation (4.25), the following assumptions are made: (a) the tracer $i\#$ is assumed to have identical physical properties to species i; (b) the Stefan-Maxwell diffusion coefficients are assumed to be the geometrical average of the self diffusion coefficients:

$$D_{ij} = \sqrt{D_{i\#,i} D_{j\#,j}} \quad ; \tag{4.26}$$

and (c) the self diffusion coefficients are related to the effective diffusion coefficients by

$$D_{i\#,\text{eff}} = \left(\sum_{k=1}^{n} x_k / D_{i\#,k} \right)^{-1} . \tag{4.27}$$

Note that the self diffusion coefficients in Equation (4.26) are not given by Equation (4.18), which is for a pure substance. The derivation of Equation (4.25) is given in Wesselingh and Bollen (1997) in terms of the Stefan-Maxwell friction coefficients ζ_{ij} which are related to the Stefan-Maxwell diffusion coefficients by:

$$\zeta_{ij} = \frac{RT}{D_{ij}} \tag{4.28}$$

The theory described by Wesselingh and Bollen (1997) is applicable to mixtures of approximately spherical molecules with similar size and chemical structure that interact as hard spheres. The sequence of steps to evaluate D_{ij} in Equation (4.25) is as follows:

(1) Evaluate $V_{F,i}$ from Equation (4.23), using Equations (4.22) and (4.24);

(2) Substitute $V_{F,i}$ from step 1 into Equation (4.19) to obtain $D_{i\#,\text{eff}}$, using Equations (4.20) and (4.21) to evaluate $D^o{}_{i\#,i}$;

(3) Perform steps 1 and 2 for each species i and evaluate D_{ij} from Equation (4.25).

The required parameters are the molecular diameters d_i; molar masses M_i; molar volumes $\tilde{V}_i$; and free molar volumes $\tilde{V}_{F,i}$ of each species i. The parameters can be determined or estimated for a variety of mixtures of neutral species as noted by Wesselingh and Bollen (1997, pp. 596-600). Examples of the determination of D_{ij} using Equations (4.19)-(4.25) are given in the Appendix.

4.3 Mixtures of Charged Species

Diffusion of electrolytes has been modeled using the theory of Debye and Hückel. The theory has been applied to determine activity coefficients in dilute electrolyte solutions and the results are valid only in the limit of infinite dilution due to the neglect of short-range interaction forces between ions in concentrated electrolyte solutions (Newman, 1991; Pinto and Graham, 1986). In comparing the commonly used form of the electrolyte diffusion equations derived from the theory of irreversible thermodynamics with the Stefan-Maxwell Equations (4.8), Graham and Dranoff (1982) found that the Stefan-Maxwell diffusion coefficients were (a) less concentration dependent than the

phenomenological coefficients of irreversible thermodynamics and (b) less dependent on the presence of other ions in the system. Pinto and Graham (1986) relate the Stefan-Maxwell coefficients to the viscosity of the solution and limiting ionic mobilities; they state that "the coefficients of the Stefan-Maxwell equations, unlike the coefficients of other flux equations, can be individually identified with physical phenomena occurring during the diffusion process."

The Stefan-Maxwell diffusion coefficients (or binary interaction parameters) defined by Equation (4.8) are not easily measured (Miller, 1967, p. 632). In solutions of electrolytes the quantities that are usually measured are (a) the transference numbers, t_i, which are the ratios of current carried by species i to the total current (when concentration gradients are negligible), (b) the electrical conductivity, κ, of the solution, and (c) the diffusion coefficient of the salt, D, based on a concentration gradient.

4.3.1 Binary Electrolyte in a Solvent

In a binary electrolytic solution composed of a cation, an anion, and a solvent, Newman (Chapter 12, p. 268, and Chapter 14, p. 298) has related the quantities that are usually measured (described above) to the Stefan-Maxwell coefficients The results are:

$$D_{o-} = \frac{z_+ D}{(z_+ - z_-)t_+^o} \tag{4.29}$$

$$D_{o+} = \frac{-z_- D}{(z_+ - z_-)(1 - t_+^o)} \tag{4.30}$$

$$\frac{1}{D_{+-}} = -\frac{z_+ z_- c_T F^2}{RT\kappa} - \frac{(z_+ - z_-)c_o t_+^o t_-^o}{z_+ \nu_+ c_s D} \tag{4.31}$$

$$\mathrm{D} = D\frac{c_T}{c_o}\left(1 + \frac{\mathrm{d}\ln\gamma_{+-}}{\mathrm{d}\ln m}\right) \tag{4.32}$$

$$\frac{1}{\kappa} = \frac{-RT}{c_T z_+ z_- F^2}\left(\frac{1}{D_{+-}} + \frac{c_o t_-^o}{c_+ D_{o-}}\right) \tag{4.33}$$

where the symbols +, -, and o refer to the cation, anion, and solvent, respectively; F is the Faraday constant (96487 C/mole); c_T is the total molar concentration; c_s is the concentration of the electrolyte (salt); z is the signed charge number of the ion; $\gamma_{\pm}$ is the mean molal ionic activity coefficient of the electrolyte; ν is the stoichiometric coefficient; D is the diffusion coefficient of the electrolyte (salt) based on a thermodynamic driving force (Newman, 1991, p. 268); D is the diffusion coefficient of the electrolyte (salt) based on a concentration gradient (Newman, 1991, p. 268) and m is the molality of the solution (moles of electrolyte per kg of solvent). Note that the transference numbers given in these equations are for the ions with respect to the solvent velocity. Newman (1991, Ch. 14, Fig. 14.1) shows that the Stefan-Maxwell diffusion coefficients D_{o+} and D_{o-} (the neutral/ion interactions) are reasonably independent of concentration (on a log scale) for an aqueous solution of KCl; the ion-ion coefficient D_{+-} increases with the square root of concentration.

For a dilute solution of a single salt it can be shown (Newman, 1991, Ch. 11, pp. 247-248) that the salt diffusion coefficient is given by:

$$\mathrm{D} = \frac{z_+ u_+ D_- - z_- u_- D_+}{z_+ u_+ - z_- u_-} \tag{4.34}$$

where u_i is the ionic mobility which is related to the ionic diffusion coefficient D_i by the Nernst-Einstein equation:

$$D_i = RTu_i \tag{4.35}$$

where R is the universal gas constant. Ionic equivalent conductances, λ_i, are typically reported in the literature (Newman, 1991, pp. 254-255; Reid et al., 1987, p. 620); these are related to the ionic mobility by:

$$\lambda_i = |z_i| F^2 u_i \quad . \tag{4.36}$$

The transference numbers are related to the ionic equivalent conductances by:

$$t_+^o = 1 - t_-^o = \frac{\lambda_+}{(\lambda_+ + \lambda_-)} \tag{4.37}$$

Substituting (4.36) and (4.35) into (4.34) gives:

$$D = -\frac{RT(z_+ - z_-)\lambda_+\lambda_-}{F^2 z_+ z_- (\lambda_+ + \lambda_-)} \quad . \tag{4.38}$$

This expression is equivalent (using the electroneutrality condition $\nu_+ z_+ = -\nu_- z_-$) to the infinite dilution diffusion coefficient given in Robinson and Stokes (1959) on page 288 (called the Nernst-Hartley relation):

$$D^o = \frac{RT(\nu_+ + \nu_-)}{F^2 \nu_+ z_+} \frac{\lambda_+^o \lambda_-^o}{(\lambda_+^o + \lambda_-^o)} \tag{4.39}$$

where ν_+ and ν_- are the stoichiometric coefficients of the cation and anion, respectively; λ_+^o and λ_-^o are limiting (zero concentration) ionic conductances with units of $(A/cm^2)/(V/cm)(mole/cm^3)$; and R is the gas constant in units of J/(mole-K) to give the diffusion coefficient in units of cm^2/s.

For the effects of concentration, Reid et al. (1987, pp. 621-622) recommend an empirical correlation that has been applied to systems with concentrations as high as 2N (where
N is g-equivalent of solute per liter of solution):

$$D = D^o \frac{\eta_o}{\eta} (c_o \bar{V}_o)^{-1} \left(1 + m \frac{\partial \ln \gamma_{\pm}}{\partial m}\right) \tag{4.40}$$

where c_o is the molar density of the solvent, $\bar{V}_o$ is the partial molar volume of the solvent, η_o and η are the viscosity of the solvent and solution, respectively, in centipoises, m is the molality of the solute in moles/kg of solvent, and $\gamma_{\pm}$ is the mean molal ionic activity coefficient of the solute.

4.3.2 Multicomponent Electrolyte Solution (with a solvent)

By relating the Stefan-Maxwell equations describing a single electrolyte in a solvent under conditions of zero current with the Nernst-Hartley relation, modified for electrophoretic and concentration effects, Pinto and Graham (1986) arrived at the following func

tional form of the Stefan-Maxwell diffusion coefficients:

$$D_{ij} = kTf_1\left(\omega_i^o, \omega_j^o\right) f_2(\kappa d) f_3(\eta) \tag{4.41}$$

where $f_1\left(\omega_i^o, \omega_j^o\right)$ is a mobility function, $f_2(\kappa d)$ is a concentration dependent relaxation effect, and $f_3(\eta)$ is a correction factor for the viscosity change of the solution with concentration. Applied to the case of tracer diffusion in a solution of a single electrolyte they determined the Stefan-Maxwell diffusion coefficients when ions i and j are similarly charged (both positive or both negative):

$$D_{ij} = -\frac{2kT\omega_i^o\omega_j^o}{\left(\omega_i^o|z_i| + \omega_j^o|z_j|\right)}\left(\frac{A_{ij}\sqrt{x_I}}{1+\sqrt{x_I}}\right)\left(\frac{\eta^o}{\eta}\right)^{0.7} \tag{4.42}$$

and when ions i and k are oppositely charged:

$$D_{ik} = \frac{kT\omega_i^o\omega_k^o}{\left(\omega_i^o\nu_k + \omega_k^o\nu_i\right)}\left(\frac{A_{ik}\sqrt{x_I}}{1+\sqrt{x_I}}\right)\left(\frac{\eta^o}{\eta}\right)^{0.7} \quad ; \tag{4.43}$$

ω_i^o is the infinite dilution mobility of species i ; η^o is the viscosity of the solvent; η is the solution viscosity; x_I is the total ionic mole fraction; and A_{ij} and A_{ik} are constants which must be determined. Predictions of tracer diffusivities in single electrolyte solutions at concentrations up to 4M were made using Equations (4.42) and (4.43), and good agreement with experimental values was obtained.

4.3.3 Solventless Electrolyte Solutions

The preceding discussion of charged species diffusion coefficients in electrolyte solutions was for electrolytes in a solvent, usually water. In some important applications (e.g., thermal batteries) the mixture consists of electrolytes without neutral species, and the electrolytes typically form a concentrated mixture.

4.3.4 Molten Salt Mixtures consisting of Two Salt Species and a Common Ion

Pollard and Newman (1979) studied the transport equations including the Stefan-Maxwell formulation for the case of two salt species and a common ion; they formulated the equations in several reference frames. The formulation follows the approach

taken by Newman (1991, Ch. 12) for a single electrolyte in a solvent (discussed above). First the Stefan-Maxwell Equation (4.8) is written for two ionic species (1 and 2; e.g., Li^+ and K^+ formed when a mixture of LiCl and KCl dissociates):

$$c_1 \nabla \mu_1 = \frac{RT}{c_T}\left[\frac{c_1 c_2}{D_{12}}(v_2 - v_1) + \frac{c_1 c_3}{D_{13}}(v_3 - v_1)\right] \tag{4.44}$$

$$c_2 \nabla \mu_2 = \frac{RT}{c_T}\left[\frac{c_2 c_1}{D_{21}}(v_1 - v_2) + \frac{c_2 c_3}{D_{23}}(v_3 - v_2)\right] . \tag{4.45}$$

Then, using the expression for the current density:

$$i = F\sum_{i=1}^{n} z_i N_i \tag{4.46}$$

Equations (4.44) and (4.45) are combined to yield equations for the molar fluxes:

$$N_1 = c_1 v_1 = -\frac{\nu_1^A \nu_3^B D}{RT} c_A \nabla \mu_A + \frac{t_1^c i}{z_1 F} + c_1 v_3 \tag{4.47}$$

$$N_2 = c_2 v_2 = -\frac{\nu_2^B \nu_3^A D}{RT} c_B \nabla \mu_B + \frac{t_2^c i}{z_2 F} + c_2 v_3 \tag{4.48}$$

where A and B designate the two neutral salt species (e.g., LiCl and KCl) which dissociate into

$$\mathrm{M}_A = \nu_1^A \mathrm{M}_1^{z_1} + \nu_3^A \mathrm{M}_3^{z_3} \tag{4.49}$$

$$\mathrm{M}_B = \nu_2^B \mathrm{M}_2^{z_2} + \nu_3^B \mathrm{M}_3^{z_3} \tag{4.50}$$

(the M's and ν's being the chemical symbols and stoichiometric coefficients of the species, respectively); c_T is the total concentration; $c_A = c_1 / \nu_1^A$; $c_B = c_2 / \nu_2^B$; the effective diffusion coefficient D based on a thermodynamic driving force (gradient of chemical potential) is given by:

$$D = \frac{z_3^2 c_T / \left(\nu_1^A \nu_2^B\right)}{\dfrac{z_1^2 c_1}{D_{23}} + \dfrac{z_2^2 c_2}{D_{13}} + \dfrac{z_3^2 c_3}{D_{12}}} \quad ; \tag{4.51}$$

and the transference numbers t_i^c of the ions relative to the velocity of the common ion (species 3; e.g., Cl^-) are:

$$t_2^c = 1 - t_1^c = \frac{\frac{z_2}{D_{13}} - \frac{z_3}{D_{12}}}{\left(\frac{z_2}{D_{13}} - \frac{z_3}{D_{12}}\right) + \frac{z_1 c_1}{z_2 c_2}\left(\frac{z_1}{D_{23}} - \frac{z_3}{D_{12}}\right)} \quad . \tag{4.52}$$

Note that $t_3^c = 0$ in the common ion velocity reference frame. The effective electrical conductivity of the solution is given by:

$$\kappa = \left(\frac{F^2 c_T}{RT}\right) \frac{\left(\frac{z_1^2 c_1}{D_{23}} + \frac{z_2^2 c_2}{D_{13}} + \frac{z_3^2 c_3}{D_{12}}\right)}{\left(\frac{c_1}{D_{12} D_{13}} + \frac{c_2}{D_{12} D_{23}} + \frac{c_3}{D_{13} D_{23}}\right)} \quad . \tag{4.53}$$

The Stefan-Maxwell diffusion coefficients D_{12}, D_{13}, and D_{23} are determined (Larson, 1998) from Equations (4.51)-(4.53) from the measured values of D, t_2^c, and κ. Pollard and Newman (1979) give the fluxes, transference numbers, and diffusion coefficients in several other reference frames including that of the mass average velocity. Although the Stefan-Maxwell diffusion coefficients D_{ij} are independent of the reference frame, the particular expression to use (i.e., Equations (4.51)-(4.53) or similar expressions given in Pollard and Newman (1979)) in determining the D_{ij}'s depends on the reference frame in which the data (e.g., transference numbers, salt diffusion coefficients, and effective electrical conductivity of the solution) is obtained. We note that the measured diffusion coefficient may be based on concentration gradients (i.e., D) rather than D, which is based on gradients in electrochemical potential; the two are related by:

$$\mathrm{D} = D\left(\frac{c_3}{c_A + c_B}\right)\left(\nu_1^A + \frac{d \ln \gamma_A}{d \ln x_A}\right) \quad . \tag{4.54}$$

4.3.5 Multicomponent Molten Salt Mixtures

In a multicomponent mixture of n species (e.g., (n-1) charged species and one solvent species), there are $n(n\text{-}1)/2$ Stefan-Maxwell diffusion coefficients D_{ij} corresponding to

one solution electrical conductivity κ, (n-2) independent transference numbers t_i^o, and (n-1)(n-2)/2 salt diffusion coefficients D_i. A formal procedure for inverting the Stefan-Maxwell equations and relating the Stefan-Maxwell diffusion coefficients D_{ij} to κ, t_i^o, and D_i is described in Newman (1991, Ch. 12, pp. 275-278). The procedure can be implemented in a computer program to determine the Stefan-Maxwell diffusion coefficients D_{ij}, given values of κ, t_i^o, and D_i. If this data is not available it may be possible to calculate the Stefan-Maxwell coefficients directly from molecular dynamics simulations.

4.4 Appendix. Example of calculation of Stefan-Maxwell diffusion coefficients, D_{ij}, using the free volume theory as presented in Wesselingh and Bollen (1997).

Consider the ternary system toluene (species 1), chlorobenzene (species 2), and bromobenzene (species 3). The properties are (see Wesselingh and Bollen, 1997, p. 599):

	$\tilde{V}_i$ (cm^3/mole)	$\tilde{V}_{F_i}$ (cm^3/mole)	d_i (cm*10^8)	M_i (g/mole)
toluene (species 1)	81.32	24.79	5.131	92
chlorobenzene (species 2)	76.17	21.41	5.02	113
bromobenzene (species 3)	83.51	21.86	5.177	157

Assume $x_1 = x_2 = 0.5$; $x_3 = 0$. From equation (4.22)

$$V_F = 0.5(24.79) + 0.5(21.41) = 23.1\,\text{cm}^3/\text{mole}.$$

From equation (4.24)

$$\sigma_1 = 0.5(81.32)^{2/3} / \left[0.5(81.32)^{2/3} + 0.5(76.17)^{2/3}\right] = 0.511;\ \text{similarly}\ \sigma_2 = 0.489.$$

From equation (4.23)

$$V_{F,1} = \frac{0.511}{0.5}(23.1) = 23.6 \text{ cm}^3/\text{mole}; \text{ similarly } V_{F,2} = 22.6 \text{ cm}^3/\text{mole}, \text{ and}$$

$$V_{F,3} = 24.02 \text{ cm}^3/\text{mole}.$$

From equation (4.21)

$$\overline{\rho} = 0.5\left(\frac{92}{81.32}\right) + 0.5\left(\frac{113}{76.17}\right) = 1.31 \text{ g/cm}^3.$$

From equation (4.20)

$$D^o_{1\#,1} = \frac{1}{6}\sqrt{\frac{3kT}{\overline{\rho} d_1}} = 2.268\text{x}10^{-4} \text{cm}^2/\text{s}; \text{ similarly } D^o_{2\#,2} = 2.293\text{x}10^{-4} \text{cm}^2/\text{s}, \text{ and}$$

$$D^o_{3\#,3} = 2.258\text{x}10^{-4} \text{cm}^2/\text{s}.$$

From equation (4.19)

$$D_{1\#,\text{eff}} = D^o_{1\#,1} \exp\left(-0.7\frac{\tilde{V}_1}{V_{F,1}}\right) = 2.033\text{x}10^{-5} \text{cm}^2/\text{s}; \text{ similarly}$$

$$D_{2\#,\text{eff}} = 2.166\text{x}10^{-5} \text{cm}^2/\text{s}, \text{ and } D_{3\#,\text{eff}} = 1.981\text{x}10^{-5} \text{cm}^2/\text{s}.$$

The Stefan-Maxwell diffusion coefficients are now evaluated from equation (4.25)

$$D_{12} = \frac{D_{1\#,\text{eff}} D_{2\#,\text{eff}}}{\left(\frac{x_1}{D_{1\#,\text{eff}}} + \frac{x_2}{D_{2\#,\text{eff}}}\right)^{-1}} = 2.1\text{x}10^{-5} \text{cm}^2/\text{s}; \text{ similarly } D_{13} = 1.92\text{x}10^{-5} \text{cm}^2/\text{s}, \text{ and}$$

$$D_{23} = 2.05\text{x}10^{-5} \text{cm}^2/\text{s}.$$

These values can be compared with those given in Wesselingh and Bollen (1997) in Figure 12, p. 599.

For the composition $x_1 = x_3 = 0.15$; $x_2 = 0.7$, the Wesselingh and Bollen procedure yields $D_{12} = 1.75\text{x}10^{-5} \text{cm}^2/\text{s}$, $D_{13} = 1.598\text{x}10^{-5} \text{cm}^2/\text{s}$, and $D_{23} = 1.706\text{x}10^{-5} \text{cm}^2/\text{s}$. These values can be compared with Stefan-Maxwell coefficients $D_{12} = 1.91\text{x}10^{-5} \text{cm}^2/\text{s}$, $D_{13} = 1.77\text{x}10^{-5} \text{cm}^2/\text{s}$, and $D_{23} = 1.81\text{x}10^{-5} \text{cm}^2/\text{s}$ obtained by Rutten (1992), p. 70, Table 4.3, from measured Fick diffusion coefficients.

4.5 Nomenclature

D	diffusion coefficient of salt based on a concentration gradient, see Equation (4.32), cm^2/s.
$\mathcal{D}$	diffusion coefficient of electrolyte based on a thermodynamic driving force, see Equations (4.29)-(4.33), (4.47)-(4.48), (4.51), cm^2/s.
$\mathcal{D}_{12}$	binary diffusion coefficient of species 1-2 pair, defined by Fick's first law, Equation (4.1) or (4.2), cm^2/s.
D_{12}	diffusion coefficient of infinitely dilute solute (species 1) in solvent (species 2); see Stokes-Einstein and related equations, Equations (4.9)-(4.13), cm^2/s.
$\mathcal{D}_{ij}$	Stefan-Maxwell diffusion (interaction) coefficient of species *i-j* pair, see Equation (4.8), cm^2/s.
D_{ij}	multicomponent diffusion coefficient of species *i-j* pair, see Equation (4.6), cm^2/s.
$D_{i\#,i}$	self diffusion coefficient of species *i*, see Equation (4.18), cm^2/s.
F	Faraday's constant, 96487 C/mole.
$\overline{G}_i$	partial molal Gibbs free energy of species *i*, ergs/mole.
J_i	molar diffusion flux of species *i* relative to the mass average velocity, moles *i*/cm^2-s.
M_i	molar mass of species *i*, g /mole.
N_i	molar flux of species *i*, g/cm^2-s.
R	gas constant, 8.314×10^7 ergs/mole-K (also 8.314 J/mole-K, used in conjunction with variables given in terms of amps (A) and volts (V), as in Equations (4.38) and (4.39)).
R_i	radius of particle (solute) or solvent species in Equations (4.10)-(4.12), cm.
T	temperature, K.
$\tilde{V}_i$	molar volume of species *i*, cm^3 *i*/mole *i*.
Y_i	mass fraction of species *i*.
c_i	molar concentration of species *i*, moles i/cm^3.
c	molar concentration, moles/cm^3.

d_i molecular diameter of species *i*, cm.

f_{12} force required to give species 1 a unit velocity in liquid 2, dynes-s/cm.

i current density, A/cm^2.

j_i mass diffusion flux of species *i* relative to the mass average velocity, g *i*/cm^2-s.

k Boltzmann's constant, 1.38x10^{-16} ergs/molecule-K.

m molality of solution, moles of electrolyte per kg of solvent.

p pressure, dynes/cm^2.

t_i^c transference number of ionic species *i* with respect to the common ion velocity, see e.g., Equation (4.52).

u_i mobility of ionic species *i*, cm^2-mole/erg-s

v_i average velocity of species *i*, cm/s.

v mass average velocity, cm/s.

x_i mole fraction of species *i*.

z_i signed charge number (valence) of ionic species *i*.

γ_i activity coefficient of species *i*.

$\gamma_{\pm}$ mean molal ionic activity coefficient of electrolyte (salt).

ζ_{ij} Stefan-Maxwell friction coefficients, see Equation (4.28), g/mole-s.

η_i viscosity of species *i*, g/cm-s.

κ electrical conductivity of ionic solution, see e.g., Equations (4.33) and (4.53), C^2/erg-cm-s.

λ_i ionic equivalent conductance of species *i*, see Equation (4.36), (A/cm^2)/(V/cm)(C/cm^3) or cm^2/ohm-mole.

μ_i electrochemical (or chemical) potential of species *i*, ergs/mole.

ν_i stoichiometric coefficient of species *i*.

ρ_i mass density of species *i*, g *i*/cm^3.

$\tilde{r}_i$ mass density of pure species *i*, g *i*/cm^3 *i*.

ρ mass density, g/cm^3.

σ_i surface fraction of species *i*, see Equation (4.24).

ω_i mobility of ionic species i as used in Equations (4.41)-(4.43), cm^2-molecule/erg-s

Subscripts

o refers to the solvent species.

s refers to the electrolyte species (or salt).

T refers to total quantity, e.g., total concentration in Equations (4.44) and (4.45).

F refers to free volume, see Equation (4.18).

eff refers to effective diffusion coefficient, see Equation (4.27).

$+$ refers to the cation.

$-$ refers to the anion.

Superscripts

o refers to the solvent species or an infinitely dilute condition as used in Equations (4.39) and (4.40).

c refers to the common ion.

(c) refers to a flux due to concentration gradients.

Overbars

$\bar{}$ average quantity or property of mixture or solution or partial molar (or molal) quantity.

$\tilde{}$ property of pure substance.

5. MICROSCALE MODELING OF DIFFUSION-CONTROLLED TRANSPORT IN A THERMAL-BATTERY USING THE LATTICE BOLTZMANN METHOD

5.1 Introduction

The reliability and performance of thermal batteries depends on the coupled chemistry and transport occurring within the electrodes. These electrodes are porous and have a complex, evolving morphology. Consequently, thermal batteries may be investigated at multiple length scales. This is illustrated in Fig. 5.1. In macrohomogeneous models, developed by Newman and Tobias (1962) and developed extensively in this LDRD work, the details of the electrode pores are not considered. Instead effort is focussed on accurate implementations of the chemistry and concentrated species transport. As shown in the center of the figure, it may be possible to develop mesoscale models in which the electrodes are considered to be inhomogeneous, but the pore scale transport is not addressed. The approach taken in this section is to simulate the transport of ionic species in complex morphologies on the microscale. In order to probe this geometrically complex problem, the chemistry and transport are simplified. The transport is assumed to be diffusion limited, and Fick's law of diffusion is used for the species transport. These simplifications allow the problem to simulated at the microscale, giving insight into two phenomena that occur within the pores of the electrodes. It is known that concentration gradients occur within the pores, especially for early times. In this pulsed or burst power mode, these gradients may effect the performance of the battery. Another concern involves fouling. Under certain conditions, potassium chloride may precipitate within the pores of the cathode. If this precipitate forms a coating over the electrode surface, the power producing reaction is effectively blocked, shortening the lifetime of the battery. Pore scale modeling is needed to investigate these heterogeneous, microscale phenomena which are extremely difficult to probe experimentally.

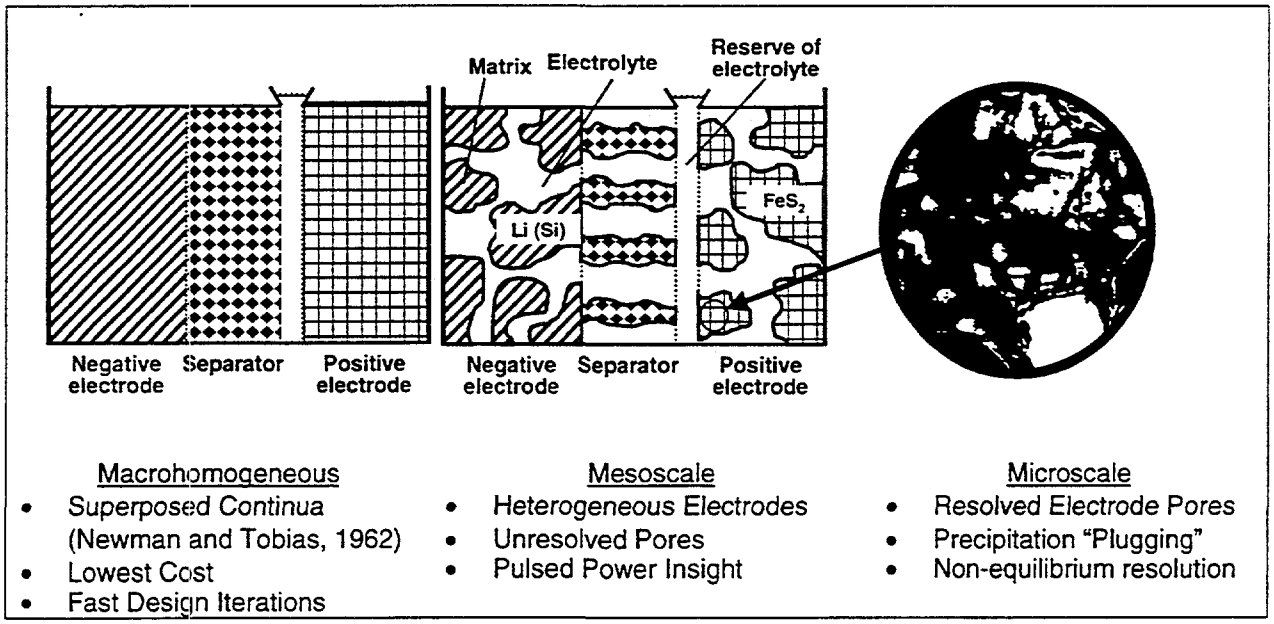

Figure 5.1. Finding the Correct Scale for Thermal Battery Simulations

The lattice Boltzmann (LB) method (McNamara and Zanetti, 1988; Higuera and Jiménez, 1989; Chen and Doolen, 1997) is a relatively new numerical technique for solving transport problems. The method is based on concepts from kinetic theory, but unlike particle-based methods such as Molecular Dynamics (MD) or Direct Simulation Monte Carlo (DSMC), LB does not simulate individual particle motion. Although detailed particle simulations

recover Navier-Stokes behavior in the continuum limit, they are too expensive to use for simulating continuum-scale hydrodynamics. The LB method also recovers Navier-Stokes behavior (Chen et al., 1992) but incorporates a simpler, probabilistic model of particle motion that is far less expensive to compute. Rather than resolving the detailed molecular scale transport, the method provides a kinetic theory-motivated solution technique for macroscopic transport equations.

LB models have been developed for a number of complex transport problems including mixing of miscible fluids (Flekkøy, 1993), multiphase flows (Gunstensen et al., 1991; Grunau et al., 1993) and chemically reacting flows (Dawson et al., 1993). Noble et al. (1997) developed a LB model for simulating inert solute transport in randomly packed beds using a LB model for the advection-diffusion equation. By analogy, these results directly apply to heat transfer as well. Using the Chapman-Enskog expansion technique from kinetic theory, this work showed that the scalar transport equation can be accurately simulated using a four-speed LB model as compared to the nine-speed model used previously (Shan, 1997). More importantly, an expression for the LB particle distribution is derived in terms of the solute concentration and its gradients. This allows the prescription of accurate boundary and initial conditions for the particle distribution function in terms of known macroscopic quantities, such as the concentration and its gradients. This model is applied here to ion species transport in a microscopic model of a thermal battery.

5.2 Lattice Boltzmann Theory

Using the LB method, the Navier-Stokes and advection-diffusion equations are not solved directly. Instead, a discretization of the underlying Boltzmann equation is formulated such that the hydrodynamics and scalar fields (i.e. temperature or concentration) satisfy the correct transport equations to within the discretization error of the method. Although the fluid was assumed to remain stationary for these simulations, the hydrodynamic and scalar transport LB models are both described here for completeness. In LB, the problem is solved in terms of particle distribution functions, f_i and g_i. The quantity f_i relates to the probability of finding a particle in the vicinity of $\mathbf{x}$ at time t that is moving with velocity $\mathbf{e}_i$. For mass transfer, g_i relates to the probability of finding a solute particle in the vicinity of $\mathbf{x}$ at time t that is moving with velocity $\mathbf{e}_i$. Unlike the continuous particle distribution function in kinetic theory, f_i and g_i are defined only for a fixed set of velocities denoted by the subscript i. This discretization of the microscopic velocity space is similar to the discrete ordinate method used for radiative transport. The LB model in this work uses an underlying orthogonal, square lattice superimposed on the non-uniform computational grid. The hydrodynamics are solved on a lattice in which communication occurs over both the Cartesian directions and the diagonal directions. For two-dimensional problems the velocity space is, therefore, discretized into the four Cartesian directions,

$$\mathbf{e}_i = \frac{\Delta x}{\Delta t}\left(\cos\frac{\pi(i-1)}{2}, \sin\frac{\pi(i-1)}{2}\right), i = 1,2,3,4 \tag{5.1}$$

and the four diagonal directions,

$$\mathbf{e}_i = \sqrt{2}\frac{\Delta x}{\Delta t}\left(\cos\frac{\pi(2i-9)}{4}, \sin\frac{\pi(2i-9)}{4}\right), i = 5,6,7,8 \tag{5.2}$$

where Δt is the time step, and Δx is the grid spacing of the underlying LB grid. Also included is the probability that particles are at rest $(\mathbf{e}_0 = \mathbf{0})$. This is called a nine-speed model since the microscopic velocity field is discretized into nine different velocity states. For the species transfer, a four-speed model is sufficient for recovering the linear advection-diffusion equation with g_i being defined for the four Cartesian directions given in Eq. (5.1) (Noble, Georgiadis and Buckius, 1997). The primary variables are calculated from moments of the particle distribution, in direct analogy with the integral moments from kinetic theory. For the incompressible LB model (Zou et al., 1995) the hydrodynamics quantities, velocity and pressure, are found according to

$$p = \sum_{i=0}^{8} f_i \ , \ p_0 \mathbf{u} = \sum_{i=0}^{8} f_i \mathbf{e}_i \tag{5.3}$$

where p_0 is a reference pressure. The concentration is found from the first moment of g_i given by

$$\phi = \sum_{i=1}^{4} g_i \tag{5.4}$$

The particle distributions f_i and g_i are governed by the discrete velocity Boltzmann equation expressed as

$$\frac{\partial f_i}{\partial t} + e_i \cdot \nabla f_i = \Omega_i [f_i(\mathbf{x},t)] + F_i \tag{5.5}$$

and

$$\frac{\partial g_i}{\partial t} + e_i \cdot \nabla g_i = \Omega_i [g_i(\mathbf{x},t)] \tag{5.6}$$

where Ω_i is a collision operator that accounts for the increase or decrease of particles moving with velocity $\mathbf{e}_i$ due to interparticle collisions. The quantity F_i is a forcing term that can be used to implement a body force, such as gravity.

Using the linearized, single time relaxation model (Bhatnagar et al., 1954) from kinetic theory applied to lattice Boltzmann (Qian, 1990; Chen et al., 1991), the collision term is written as

$$\Omega_i[f] = -\frac{1}{\tau_f}\left(f_i - f_i^{(0)}\right) \tag{5.7}$$

where $f_i^{(0)}$ is an equilibrium distribution, and τ_f is the relaxation time, which characterizes the rate of decay toward equilibrium. The collision term in the scalar transport equation is handled identically. Analogous to the Maxwellian distribution, the equilibrium distribution is the distribution to which the system will evolve in the absence of forcing gradients.

Using a first-order Lagrangian discretization of the discrete velocity Boltzmann equation, the LB equations for hydrodynamics and scalar transport are expressed as .

$$f_i(\mathbf{x} + \mathbf{e}_i \Delta t, t + \Delta t) = f_i(\mathbf{x},t) - \frac{\Delta t}{\tau_f}\left[f_i(\mathbf{x},t) - f_i^{(0)}(\mathbf{x},t)\right] + F_i \Delta t \tag{5.8}$$

$$g_i(\mathbf{x} + \mathbf{e}_i \Delta t, t + \Delta t) = g_i(\mathbf{x},t) - \frac{\Delta t}{\tau_g}\left[g_i(\mathbf{x},t) - g_i^{(0)}(\mathbf{x},t)\right] \tag{5.9}$$

Examination of these equations reveals that the solution of the transport problem is reduced to two major steps. First, in a collision and forcing step, the right hand sides of Eqs. (5.8-5.9) are computed, modifying the distributions at location $\mathbf{x}$. Then, a streaming step occurs in which the particle distributions stream to their nearest neighbors. In the case of a uniform spatial grid, this produces the particle distribution at each location for the new time step. It is noted that the collision and forcing step is entirely local since all quantities are evaluated at location $\mathbf{x}$. The non-local communication occurs during the streaming step and involves only the nearest neighbors.

The selection of the equilibrium distribution determines the macroscopic partial differential equation solved by the LB method. For the two-dimensional, square grid, the equilibrium distribution for the incompressible LB hydrodynamics (Zou et al., 1995) is given by

$$f_i^{(0)} = w_i\left\{p + p_0\left[\frac{1}{c^2}(\mathbf{e}_i\cdot\mathbf{u}) + \frac{3}{2c^4}(\mathbf{e}_i\cdot\mathbf{u})^2 - \frac{1}{2c^2}(\mathbf{u}\cdot\mathbf{u})\right]\right\} \tag{5.10}$$

where $c = \Delta x/\Delta t$, and w_i is given by

$$w_i = \begin{cases} \frac{4}{9} & i = 0 \\ \frac{1}{9} & i = 1,2,3,4 \\ \frac{1}{36} & i = 5,6,7,8 \end{cases} \tag{5.11}$$

For the coupled scalar transport, the equilibrium distribution is given by

$$g_i^{(0)} = \frac{\sigma}{4} + \frac{\dot{\sigma}}{2c^2}(\mathbf{e}_i\cdot\mathbf{u}) \tag{5.12}$$

These equilibrium distributions are selected such that the incompressible Navier-Stokes equations and advection-diffusion equations are recovered to within the second-order accuracy of the method. The derivations of these distributions are more thoroughly described elsewhere (Appendix of Hou et al., 1995; Noble, 1997), but a short synopsis is given here. In order to determine the equilibrium distributions, a form of the distribution must be assumed. Typically, a power series in velocity is assumed (which approximates the exponential found in the Maxwell-Boltzmann distribution). The coefficients of the series are determined by comparing the desired transport equation to the near equilibrium behavior of the LB equation. This is accomplished by performing a Taylor series expansion of the particle distribution about the location $\mathbf{x}$ and time t. This is followed by a near equilibrium expansion, called the Chapman-Enskog expansion, in which the particle distribution is assumed to be equal to the equilibrium distribution plus higher order terms. The expansion is in terms of a Knudsen number that compares the mean free collision time to the time scale of the flow. Substituting the assumed form of the equilibrium distribution (which is defined in terms of macroscopic quantities) into the expanded LB equation gives the macroscopic equations. Comparison to the desired transport equations yields the coefficients for the equilibrium distribution along with the definition of the transport coefficients.

The transport coefficients, kinematic viscosity and thermal diffusivity, are controlled by the relaxation times. The Taylor series and Chapman-Enskog analysis of the LB models given above yield

$$\nu = \frac{2(\tau_f/\Delta t) - 1}{6}\frac{(\Delta x)^2}{\Delta t} \tag{5.13}$$

and

$$\alpha = \frac{2(\tau_g/\Delta t) - 1}{4}\frac{(\Delta x)^2}{\Delta t} \tag{5.14}$$

for the kinematic viscosity and thermal diffusivity respectively. In terms of molar quantities, the advection-diffusion equation can be written as,

$$\frac{\partial c_i}{\partial t} + u\cdot\nabla c_i = D_i\nabla^2 c_i + R_i \tag{5.15}$$

where c_i is the molar concentration of species i, D_i is the effective diffusivity, and R_i is a reaction term accounting for the net production due to reactions.

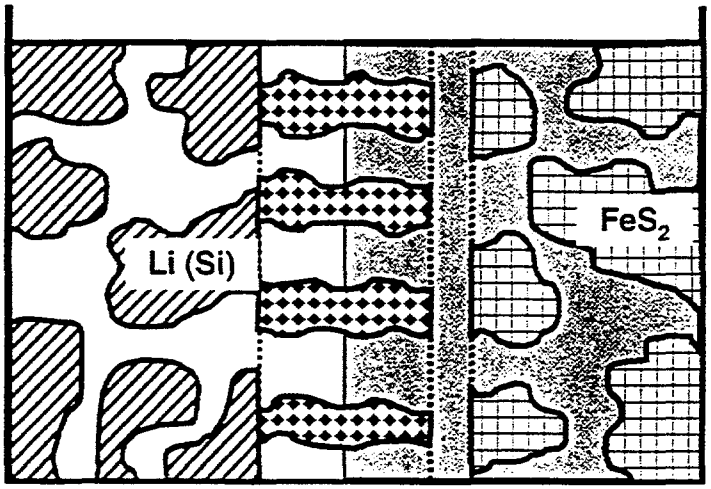

Figure 5.2. Computational Domain for Thermal Battery Simulations

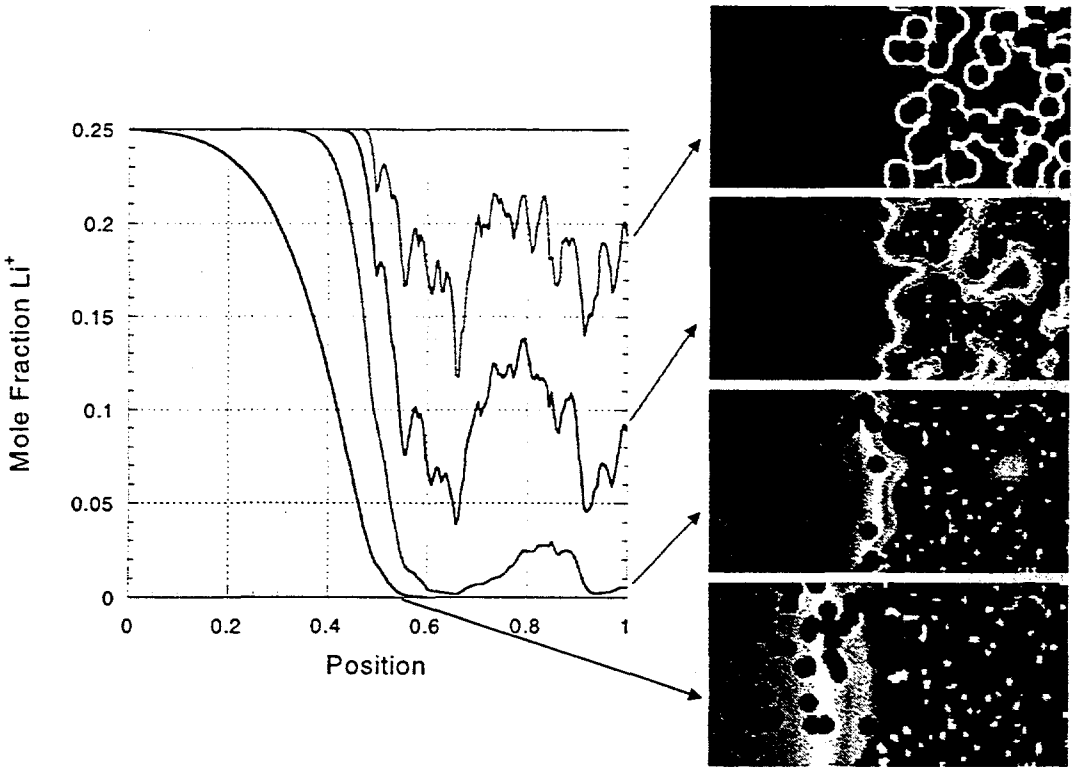

Figure 5.3. LB Simulations of Microscale Transport in Thermal Batteries

5.3 Microscale Simulations of Diffusion-Controlled Transport in Thermal Batteries

This lattice Boltzmann method is used to simulate pore scale transport in a microscopic model of a thermal battery. The computation domain considered consists of a separator region and a cathode region as shown by the shaded

region of Fig. 5.2. The region is initially filled with a relatively high concentration of lithium ions, produced at the anode. These ions diffuse toward the cathode, where they are assumed to be fully consumed instantaneously. Thus the process is assumed to be diffusion-limited for this analysis. Simultaneously, potassium and chloride ions are transported. An additional advection-diffusion LB model is used to simulate the potassium transport. The system is further constrained by the consistency condition that the sum of the mole fractions for the 3 species is unity, and the electroneutrality constraint is also imposed in the electrolyte.

5.4 Results

Figure 5.3 shows the results of a LB simulation, showing the time evolution for the lithium ion concentration within the cathode and separator regions. The right half of the figure shows 4 snapshots as the reaction proceeds. The color indicates the mole fraction of lithium ions. The very light gray regions indicate the growth of potassium chloride precipitate. The left half of the figure shows the volume averaged mole fraction as a function of position in the battery at each of the four times shown on the right, as indicated by the arrows. The noisy structure of this plot indicates the level of inhomogeneity present in the battery. This plot illustrates how "hot spots" may occur within an electrode. In manufactured thermal batteries, the large number of pores within the electrodes confines this effect to early times within small regions, however.

The potassium chloride precipitate structure is an important result of this analysis. These simulations suggest that the precipitate forms in clusters, leaving most of the reaction surface available for the power producing reaction. If instead, a thin coating were to form on the solid surfaces, the reaction could be prematurely ended. However, it appears that the solid fraction of precipitate does appear to occur close to the separator-cathode boundary. In certain configurations, sufficient precipitate formation could wall off the cathode. If so, thermal battery designs that take this into account might result in longer lifetimes and higher efficiency.

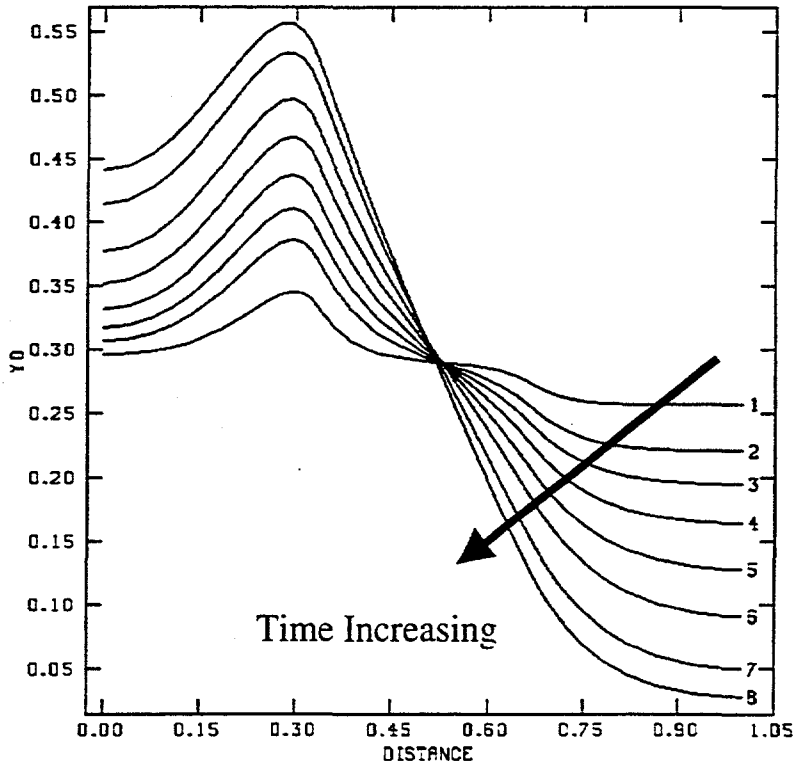

Figure 5.4a. Typical GOMA Simulation Result for Lithium Ion Concentration

Figures 5.4a-5.4b show a qualitative comparison between macrohomogeneous GOMA predictions and these LB results. Figure 5.4a shows a sample result from a GOMA simulation that employs high integrity chemistry and transport. The shaded region corresponds to the domain for the LB simulations, including half the separator and the cathode region. Figure 5.4b shows the LB result. In comparison, the GOMA prediction shows the effect of the reaction kinetics, which effectively slow down the reaction as compared to the diffusion-limited LB result. When the reaction proceeds at a slower rate, the Lithium ions have ample time to diffuse toward the cathode, resulting in the nearly linear profile in the separator exhibited by the GOMA result. When the problem is diffusion limited, the Lithium ions are consumed as fast as they arrive, causing a nonlinear profile in the separator. Improved models for the reactions are needed in the LB simulations to correctly model this effect.

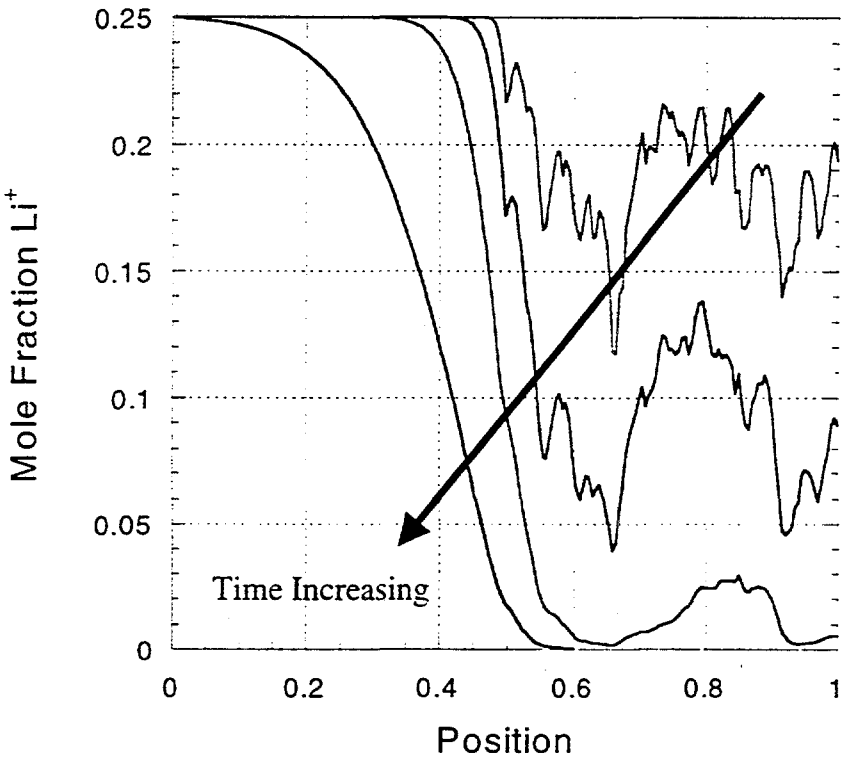

Figure 5.4b. LB Simulation Result for Lithium Ion Concentration

5.5 Conclusions

Lattice Boltzmann (LB) has been applied to the multicomponent transport of ionic species in the electrolyte of a thermal battery. In order to make it feasible to probe the heterogeneous behavior in the cathode, the transport and chemistry is significantly simplified. Fick's law is assumed, but could be extended using the methods described elsewhere in this report. The reactions at the cathode surface are assumed to consume all of the available lithium and occur instantaneously. This also could be dramatically improved using the techniques described elsewhere in this report. The lattice Boltzmann simulations are profitable for investigating the degree of heterogeneity within the cathode and for investigating the morphology of precipitate that forms within the cathode. This initial study suggests that significant heterogeneity may occur within the cathode, especially for early times. This may have significant effects on the pulsed power behavior of thermal batteries and needs to be investigated further. Regarding precipitate formation, these LB simulations suggest that the precipitate forms in small dendritic-type formations on the cathode surface. Such morphology is beneficial since it does not coat the cathode surface. This allows the

reaction to continue without causing premature battery failure. However, the precipitate production appears to occur more in the vicinity of the separator-cathode boundary. If unchecked, this could result in sealing the cathode off from the electrolyte. These microscopic effects may have critical effects on thermal battery performance.

6. LIST OF PUBLICATIONS/PRESENTATIONS/TECHNICAL MEMORANDA

K. S. Chen, G. H. Evans, R. S. Larson, M.E. Coltrin, and J. Newman "Multi-dimensional modeling of thermal batteries using the Stefan-Maxwell formulation and the finite-element method", presented at Electrochemical Society's Battery Applications Symposium, Boston, Nov. 1-6, 1998; and published in Electrochemical Society Proceedings Volume 98-15, Selected Battery Topics, edited by W. R. Cieslak et al., p. 138 - 149.

D. R. Noble and K. S. Chen "Simulation of pore-scale processes in thermal batteries", presented at the 195th Electrochemical Society Meeting, May 2-6, 1999, Seattle, Washington, paper #1015.

K. S. Chen, G. H. Evans, R. S. Larson, and W. G. Houf "Modeling thermal batteries using a multi-dimensional Stefan-Maxwell framework", presented at the Third Biennial Tri-Laboratory Conference on Modeling and Simulation, November 2-3, 1999, Lawrence Livermore National Laboratory, Livermore, CA.

R. S. Larson "Constant voltage vs. constant current in thermal battery analysis", Sandia technical memorandum, July 7, 1999.

G. H. Evans, K. S. Chen, M.E. Coltrin, R. S. Larson, J. S. Newman, J. A. Wesselingh, and R. Greif, "Estimation of Stefan-Maxwell diffusion coefficients for liquid phase processes", Sandia technical memorandum, June 24, 1999.

R. S. Larson "Liquid Chemkin update", Sandia technical memorandum, June 15, 1999.

R. S. Larson "Consecutive vs. simultaneous reactions in a thermal battery", Sandia technical memorandum, May 14, 1999.

R. S. Larson "Testing of remaining routines in Liquid Chemkin", Sandia technical memorandum, April 22, 1999.

R. S. Larson "Testing of electrochemical modeling capabilities in Chemkin", Sandia technical memorandum, April 15, 1999.

R. S. Larson "A benchmark electrochemistry problem", Sandia technical memorandum, March 26, 1999.

G. H. Evans, "Three component Stefan diffusion problem", Sandia technical memorandum, January 26, 1999.

G. H. Evans, "Idealized thermal battery problem", Sandia technical memorandum, Jan. 7, 1999.

R. S. Larson "Reconciliation of solutions to thermal battery problem", Sandia technical memorandum, November 25, 1998.

K. S. Chen "Analytical solutions of electrical potentials and current densities for a model battery cell", Sandia technical memorandum, November 18, 1998.

R. S. Larson "Solution of model thermal battery problem", Sandia technical memorandum,

November 18, 1998.

R. S. Larson "Transport properties in molten salts", Sandia technical memorandum, Oct. 27, 1998

R. S. Larson "The open-circuit potential", Sandia technical memorandum, October 6, 1998.

R. S. Larson "Very general electrode kinetics", Sandia technical memorandum, August 27, 1998.

R. S. Larson "Electrode reactions in the Li(Si)/FeS2 thermal battery", Sandia technical memorandum, June 29, 1998.

K. S. Chen "Electrochemical LDRD Task 2a report: governing equations for a Li(Si)/FeS2 thermal-battery cell", Sandia technical memorandum, June 8, 1998.

R. S. Larson "More thoughts on electrode kinetics in surface chemkin", Sandia technical memorandum, May 20, 1998.

R. S. Larson "Clarification on kinetics of charged-species reactions in condensed phases", Sandia technical memorandum, April 23, 1998.

K. S. Chen "Reactive LDRD project plan", Sandia technical memorandum, April 3, 1998.

R. S. Larson "Electrode kinetics in Surface Chemkin", Sandia technical memorandum, March 24, 1998.

K. S. Chen, G. H. Evans, and R. S. Larson "Reactive LDRD Task 1 report: governing equations for liquid-phase multicomponent transport of charged species", Sandia technical memorandum, March 16, 1998.

R. S. Larson "Proposed enhancements to Surface Chemkin", Sandia technical memorandum, March 6, 1998.

7. SUMMARY AND CONCLUDING REMARKS

In the LDRD project documented in this report, a phenomenological model was developed for multicomponent transport of charged species with simultaneous electrochemical reactions in concentrated solutions, and this was applied to model processes in a thermal battery cell. A new general framework was formulated and implemented in GOMA for modeling multidimensional, multicomponent transport of neutral and charged species in concentrated solutions. The new framework utilizes the Stefan-Maxwell equations that describe multicomponent diffusion of interacting species using composition-insensitive binary diffusion coefficients. The new GOMA capability for modeling multicomponent transport of neutral species was verified and validated using the model problem of ternary gaseous diffusion in a Stefan tube. The new GOMA-based thermal-battery computer model was verified using an idealized battery cell in which concentration gradients are absent; and the full model was verified by comparing with that of Bernardi and Newman (1987) and validated using limited thermal-battery discharge-performance data from the open literature (Dunning 1981) and from Sandia (Guidotti 1996). Moreover, a new Liquid Chemkin software package was developed, which allows the user to handle many aspects of liquid-phase kinetics, thermodynamics, and transport (particularly in terms of computing properties). Also, a systematic study was conducted for the estimation of Stefan-Maxwell diffusion coefficients used in liquid-phase transport processes. Lastly, a Lattice-Boltzmann-based capability was developed for modeling micro-scale phenomena involving convection, diffusion, and simplified chemistry; this capability was demonstrated by modeling phenomena in the cathode region of a thermal-battery cell.

The impact of this LDRD project on Defense Programs at Sandia is obvious and direct because thermal batteries are employed as the primary power sources in nuclear weapons. The GOMA-based thermal-battery computer model reported here can be employed as a tool to provide guidance in process design and optimization of thermal batteries.

In summary, a basic or generic GOMA-based capability has been developed to predict the voltage-vs.-time performance behavior of thermal battery cells during discharge. To be useful in process design and optimization of thermal batteries, however, the present work needs to be extended both at the cell level and at the system level. At the cell level, several areas of further model development are needed:

1) incorporation of a simultaneous reaction mechanism in which two or more electrochemical reactions are allowed to take place at any given discharge time.

2) allowance for precipitation of KCl and LiCl salts during discharge, which can result in pore plugging and thus shut off the battery discharge process (cf. Pollard and Newman 1981).

3) a better understanding of thermodynamic open-circuit potentials for particular thermal battery systems (e.g., Li(Si)/LiCl-KCl/FeS_2) within the temperature range of interest; it was found from the present work that the thermodynamic open-circuit potential has a dominant effect on the battery-cell discharge behavior.

4) investigation of the effect of electrode-thickness nonuniformity, which can cause multi-dimensional transport and localized depletion of electrode materials.

5) GOMA and Liquid Chemkin coupling, which will enable us to efficiently examine complex electrochemistry mechanisms in the anode and cathode.

6) GOMA and Lattice-Boltzmann microscopic model coupling; Chapter 5 only scratches the surface of modeling microscopic phenomena in a thermal battery cell, but the ability to capture phenomena at the microscopic level will significantly increase the fidelity of our thermal battery cell model.

7) determination of Stefan-Maxwell diffusion coefficients using molecular dynamic simulation.

8) determination of other model parameters such as activity coefficients using fundamental thermodynamic data, and estimation of model parameters (e.g., anodic and cathodic transfer coefficients, exchange current density at zero utilization) that cannot be determined from fundamental data.

Lastly, it is also essential to develop system-level models in order to describe more realistically the dynamic discharge behavior of thermal battery systems.

8. REFERENCES

Bernardi, D., "Mathematical Modeling of Lithium(alloy), Iron Sulfide Cells and the Electrochemical Precipitation of Nickel Hydroxide", *Ph. D. Thesis*, University of California, Berkeley (1986).

Bernardi, D. and Newman, J., "Mathematical Modeling of Lithium(alloy), Iron Disulfide Cells", *J. Electrochem. Soc.*, **134**, pp. 1309-1318 (1987).

Bhatnagar, P.L., Gross, E.P., and Krook, M., "A Model for Collision Processes in Gases. I. Small Amplitude Processes in Charged and Neutral One-Component Systems," *Phys. Rev.*, **94**, pp. 511-525 (1954).

Bird, R. B., Stewart, W. E., and Lightfoot, E. N., Transport Phenomena, John Wiley & Sons, Inc., New York (1960).

Carty, R. and Schrodt, T., "Concentration Profiles in Ternary Gaseous Diffusion", *Ind. Eng. Chem., Fundam.*, **14**, pp. 276-278 (1975).

Chen, H., Chen, S., and Matthaeus, W.H., "Recovery of the Navier-Stokes Equations Using a Lattice Boltzmann Method", *Phys. Rev. A*, **45**, pp. R5339-R5342 (1992).

Chen, K. S., "ESRF Non-deterministic Simulation Project Subtask 1 Progress Report: Uncertainty/Sensitivity Analysis of A Polymeric-Film Drying/Solidification Process via Monte Carlo Techniques", *Sandia memorandum*, June 12 (1995).

Chen, K. S., "Uncertainty/Sensitivity Analysis of Thermal Response of A Metal-Plate Object subject to a Participating Engulfing Pool Fire via the Monte Carlo/Latin Hypercube Sampling Technique", *Sandia memorandum*, June 8 (1996).

Chen, K. S. and Cairncross, R. A., "Non-deterministic Analysis of A Liquid Polymeric-Film Drying Process", *IS&T's 50th Annual Conference Proceedings*, pp. 548-553 (1997).

Chen, K. S., Evans, G. H., and Larson, R. S., "Reactive LDRD Task 1 Report: Governing Equations for Liquid-Phase Multicomponent Transport of Charged Species", *Sandia memorandum*, March 16 (1998).

Chen, K. S., Evans, G. H., Larson, R. S., Coltrin, M. E., and Newman, J., "Multi-dimensional modeling of thermal batteries using the Stefan-Maxwell formulation and the finite-element method", presented at the *Electrochemical Society's Battery Applications Symposium*, Boston, Nov. 1- 6, paper #52, and published in *Electrochem. Soc. Proceeding* PV 98-15, Selected Battery Topics, edited by G. Halpert, M. L. Gopikanth, K. M. Abraham, W. R. Cieslak, W. A. Adams, Boston, Massachusetts (1998).

Chen, S., Chen, H. D., Martinez, D., and Matthaeus, W., "Lattice Boltzmann Model for Simulation of Magnetohydrodynamics", *Phys. Rev. Lett.*, **67**, pp. 3776-3779 (1991).

Chen, S., and Doolen, G. D., "Lattice Boltzmann Method for Fluid Flows," submitted to *Ann. Rev. Fluid Mech.* (1997).

Coltrin, M. E., Kee, R. J., and Miller, J. A., "A Mathematical Model of Silicon Chemical Vapor Deposition; Further Refinements and the Effects of Thermal Diffusion", *J. Electrochem. Soc.*, **133**, pp. 1206-1213 (1986).

Coltrin, M. E., Kee, R. J., Rupley, F. M., and Meeks, E., "SURFACE CHEMKIN-III: A FORTRAN Package for Analyzing Heterogeneous Chemical Kinetics at a Solid-surface-Gas-phase Interface", *Sandia National Laboratories Report* SAND96-8217, May (1996).

Dahlquist, G. and Bjorck, A., Numerical Methods, Prentice-Hall, Inc., Englewood Cliffs, NJ.

Danckwerts, P. V., "Diffusion and mass-transfer", in *Diffusion Processes, Proc. Thomas Graham Memorial Symposium,* University of Strathclyde, eds. J. N. Sherwood, A. V. Chadwick, W. M. Muir, and F. L. Swinton, **2**, pp. 545-560, Gordon and Breach Science Publishers, London (1971).

Dawson, S.P., Chen, S., and Doolen, G.,"Lattice Boltzmann Computations for Reaction-Diffusion Equations," *J. Chem. Phys.*, **98**, pp. 1514-1523 (1993).

Dixon-Lewis, G., "Flame structure and flame reaction kinetics II. Transport phenomena in multicomponent systems", *Proc. Roy. Soc. A.*, **307**, pp. 111-135 (1968).

Dobranich, D., "Advances in Modeling Thermally-Activated Batteries", *Sandia memorandum*, June 2 (1995).

Duncan, J. B. and Toor, H. L., *AIChE J.*, **8**, 38-41 (1962).

Dunning, J. S., in Argonne National Laboratory Report ANL-80-128, p.190 (February, 1981).

Evans, G. H., "Three component Stefan diffusion problem", *Sandia memorandum*, January 26 (1999).

Flekkøy, E.G., "Lattice Bhatnagar-Gross-Krook Models for Miscible Fluids", *Phys. Rev. E.*, **47**, pp. 4247-4257 (1993).

Gartling, D. K., Hickox, C. E., and Givler, R. C., "Simulation of Coupled Viscous and Porous Flow Problems", *Comp. Fluid Dyn.*, **7**, pp. 23-48 (1996).

Gay, E. C., Steunenberg, R. K., Miller, W. E., Battles, J. E., Kaun, T. D., Martino, F. J., Smaga, J.

A., and Chilenskas, A. A., *Argonne National Laboratory Report* ANL-84-93 (July 1985).

Getzinger, R. W. and Wilke, C. R., *AIChE J.*, **13**, 577-580 (1967).

Graham, E. E. and Dranoff, J. S., "Application of the Stefan-Maxwell Equations to Diffusion in Ion Exchangers. I: Theory", *Ind. Eng. Chem. Fundam.*, **21**, pp. 360-365 (1982).

Grunau, D., Chen, S., and Eggert, K., "A Lattice Boltzmann Model for Multiphase Fluid Flows," *Phys. Fluids A*, **5**, pp. 2557-2562 (1993).

Guggenheim, E. A., Thermodynamics, Elsevier Science Publishers B. V., North Holland Physics Publishing Division, Amsterdam (1967).

Guidotti, R. A., "Thermal batteries: a technology review and future directions", a paper presented at the 27th International SAMPE Technical Conference, Albuquerque, New Mexico, October 9 - 12 (1995).

Guidotti, R. A., "Battery-Data Package for Performance Modeling Purposes", *Sandia memorandum*, November 20 (1996).

Gunstensen, A.K., Rothman, D.H., Zaleski, S., and Zanetti, G.,"Lattice Boltzmann Model of Immiscible Fluids", *Phys. Rev. A*, **43**, pp. 4320-4327 (1991).

Higuera, F., and Jiménez, J., "Boltzmann Approach to Lattice Gas Simulations," *Europhys. Lett.*, **9**, pp. 663-668 (1989).

Hou, S., Zou, Q., Chen, S., Doolen, G.D., and Cogley, A.C., "Simulation of Cavity Flow by the Lattice Boltzmann Method," *J. Comput. Phys.*, **118**, pp. 329-347 (1995).

Kooijman, H. A. and Taylor, R., "Estimation of Diffusion Coefficients in Multicomponent Liquid Systems", *Ind. Eng. Chem. Res.*, **30**, pp. 1217-1222 (1991).

Krishna, R. and Wesselingh, J. A., "The Maxwell-Stefan approach to mass transfer", *Chemical Engineering Science*, review article 50, **52**, pp. 861-911 (1997).

Larson, R. S., "Transport Properties in Molten Salts", *Sandia memorandum*, October 27 (1998).

Larson, R. S., "Reconciliation of Solutions to Thermal Battery Problem," *Sandia memorandum*, November 25 (1998).

Lightfoot, E. N., Cussler, E. L. Jr., and Rettig, R. L., "Applicability of the Stefan-Maxwell Equa-

tions to Multicomponent Diffusion in Liquids", *AIChE Journal*, **8**, pp. 708-710 (1962).

Martinez, D.O., Matthaeus, W.H., Chen, S., Montgomery, D.C., "Comparison of Spectral Method and Lattice Boltzmann Simulations of Two-Dimensional Hydrodynamics", *Phys. Fluids*, **6**, pp. 1285-1298 (1994).

McNamara, G., and Zanetti, G., "Use of the Boltzmann Equation to Simulate Lattice-Gas Automata", *Phys. Rev. Lett.*, **61**, pp. 2332-2335 (1988).

Meyers, J. P., *Ph. D. Thesis*, University of California, Berkeley (1998).

Miller, D. G., "Application of Irreversible Thermodynamics to Electrolyte Solutions. II. Ionic Coefficients l_{ij} for Isothermal Vector Transport Processes in Ternary Systems", *J. Phys. Chem.*, **71**, pp. 616-632 (1967).

Mills, A. F., Heat and Mass Transfer, Richard D. Irwin, Inc., Chicago (1995).

Nelson et al., *Progress Report for the period 11/78-3/79*, ANL, 79-39, Argonne National Laboratory, May (1979).

Newman, J. S., Electrochemical Systems, Prentice Hall, Inc., Englewood Cliffs, New Jersey (1991).

Newman, J. and Tiedemann, W., "Porous-electrode Theory with Battery Applications", *AIChE J.*, **21**, pp. 25-41 (1975).

Newman, J. S. and Tobias, C. W., "Theoretical Analysis of Current Distribution in Porous Electrodes", *J. Electrochem. Soc.*, **109**, pp. 1185-1191 (1962).

Noble, D.R., "Lattice Boltzmann Study of the Interstitial Hydrodynamics and Dispersion in Steady Inertial Flows in Large Randomly Packed Beds", *Ph. D. Dissertation*, University of Illinois at Urbana-Champaign (1997).

Noble, D.R., Georgiadis, J.G., and Buckius, R.O., "Comparison of Accuracy and Performance for Lattice Boltzmann and Finite Difference Simulations of Steady Viscous Flow", *Int. J. Num. Meth. Fluids*, Vol. 23, pp. 1-18 (1997).

Paxton, B. and Newman, J., "Modeling of Nickel/Metal Hydride Batteries", *J. Electrochem. Soc.*, **144**, pp. 3818-3828 (1997).

Pinto, N. deG. and Graham, E. E., "Evaluation of Diffusivities in Electrolyte Solutions using Stefan-Maxwell Equations", *AIChE Journal*, **32**, pp. 291-296 (1986).

Pollard, R. and Newman, J., "Transport Equations for a Mixture of Two Binary Molten Salts in a Porous Electrode", *J. Electrochem. Soc.*, **126**, pp. 1713-1717 (1979).

Pollard, R. and Newman, J., "Mathematical Modeling of the Lithium-Aluminum, Iron Sulfide Battery: I. Galvanostatic Discharge Behavior", *J. Electrochem. Soc.*, **128**, pp. 491-502 (1981).

Prausnitz, J. M., Molecular Thermodynamics of Fluid-Phase Equilibria, Prentice Hall, Inc., Englewood Cliffs, New Jersey (1969).

Qian, Y. H., "Lattice Gas and Lattice Kinetic Theory Applied to the Navier-Stokes Equations", *Ph. D. Dissertation*, Université Pierre et Marie Curie (1990).

Riede, T. H. and Schlünder, E.-U., "Diffusivities of the Ternary Liquid Mixture 2-Propanol-Water-Glycerol and Three-Component Mass Transfer in Liquids", *Chemical Engineering Science*, **46**, pp. 609-617 (1991).

Robinson, R. A. and Stokes, R. H., Electrolyte Solutions, 2nd edition, Butterworths Scientific Publications, London (1959).

Reid, R. C., Prausnitz, J. M., and Poling, B. E., The Properties of Gases & Liquids, 4th ed., McGraw-Hill, Inc., New York (1987).

Reider, M. B. and Sterling, J.D., "Accuracy of Discrete-Velocity BGK Models for the Simulation of the Incompressible Navier-Stokes Equations", *Computers & Fluids*, **24**, pp. 459-467 (1995).

Rutten, Ph. W. M., "Diffusion in Liquids", *PhD thesis*, University of Delft, Delft University Press (1992).

Schunk, P. R., Sackinger, P. A., Rao, R. R., Chen, K. S., Cairncross, R. A., Baer, T. A., and. Labreche, D. A., "GOMA 2.0 - A Fully-Newton Finite Element Program for Free and Moving-Boundary Problems with Coupled Fluid/Solid Momentum, Energy, Mass, and Chemical Species Transport: User's Guide", *Sandia Technical Report* SAND97-2404, revised edition (1998).

Shan, X., "Simulation of Rayleigh-Benard Convection Using a Lattice Boltzmann Method", *Phys. Rev. E*, **55**, pp. 2780-2788 (1997).

Taylor, R. and Krishna, R., Multicomponent Mass Transfer, John Wiley & Sons, Inc., New York (1993).

Tomczuk, Z., Preto, S. K., and Roche, M. F., "Reactions of FeS Electrodes in LiCl-KCl Electrolyte", *J. Electrochem. Soc.*,**128**, pp. 760 - 772 (1981).

Tomczuk, Z., Tani, B., Otto, N. C., Roche, M. F., and Vissers, D. R., "Phase relationships in positive electrodes of high temperature Li-Al/LiCl-KCl/FeS_2 cells", *J. Electrochem. Soc.*,**129**, pp. 925 - 931 (1982).

Tribollet, B. and Newman, J., "Impedance Model for a Concentrated Solution: Application to the Electrodissolution of Copper in Chloride Solutions", *J. Electrochem. Soc.*, **131**, pp. 2780-2785 (1984).

Vignes, A., "Diffusion in Binary Solutions", *Ind. Eng. Chem. Fundam.*, **5**, pp. 189-199 (1966).

Wen, C. J. and Huggins, R. A. *J. Solid State Chem.*, **37**, pp.271 (1981).

Wesselingh, J. A. and Bollen, A. M., "Multicomponent Diffusivities from the Free Volume Theory", *Trans. IChemE*, **75**, pp. 590-602 (1997).

Wesselingh, J. A. and Krishna, R., Mass Transfer, Ellis Horwood, London, U. K. (1991).

Zou, Q., Hou, S., Chen, S., and Doolen, G.D., "An Improved Incompressible Lattice Boltzmann Model for Time-Independent Flows", *J. Stat. Phys.*, **81**, pp. 35-48 (1995).

9 DISTRIBUTION

MS 0828	9101	T. C. Bickel
MS 0834	9112	A. C. Ratzel
MS 0836	9100	C. W. Peterson
MS 0835	9111	S. N. Kempka
MS 0835	9111	P. A. Sackinger
MS 0835	9111	S. R. Subia
MS 0826	9113	W. H. Hermina
MS 0826	9113	D. R. Noble
MS 0826	9113	C. C. Wong
MS 0826	9114	J. E. Johannes
MS 0826	9114	T. A. Baer
MS 0826	9114	K. S. Chen (5)
MS 0826	9114	R. R. Rao
MS 0826	9114	P. R. Schunk(9)
MS 0826	9114	A. C.-T. Sun
MS 0827	9117	R. O. Griffith
MS 0827	9117	D. Dobranich
MS 0828	9132	J. L. Moya
MS 0828	9132	T. Y. Chu
MS 0613	2521	D. H. Doughty
MS 0613	2521	D. Ingersoll
MS 0613	2521	R. G. Jungst
MS 0613	2521	G. Nagasubramanian
MS 0613	2522	P. C. Butler
MS 0614	2522	R. A. Guidotti
MS 0614	2522	S. F. Kuehn
MS 0601	1113	J. S. Nelson
MS 0601	1126	M. E. Coltrin
MS 0601	1126	H. K. Moffat
MS 9405	8700	T. M. Dyer
MS 9042	8728	M. W. Perra
MS 9042	8728	G. H. Evans (5)
MS 9042	8728	S. K. Griffiths
MS 9042	8728	W. G. Houf
MS 9042	8728	M. P. Kanouff
MS 9051	8728	R. S. Larson
MS 9042	8728	R. H. Nilson
MS 9042	8728	A. Ting
MS 0820	9225	H. E. Fang
MS 1111	9225	A. P. Thompson
MS 0188	4001	LDRD Office
MS 0612	4912	Review and Approval Desk (1) for DOE/OSTI
MS 0899	4916	Technical Library (2)
MS 9018	8940-2	Central Technical Files

Dr. Ellen Meeks
Reaction Design
304 Daisyfield
Livermore, CA 94550

Dr. Robert J. Kee
George R. Brown Professor of Engineering
Colorado School of Mines
Golden, CO 80401-1887

Prof. John Newman
Department of Chemical Engineering
University of California, Berkeley
Berkeley, CA 94720-1462

Prof. Ralph Greif
Department of Mechanical Engineering
University of California, Berkeley
Berkeley, CA 94720

Prof. John W. Weidner
Department of Chemical Engineering
University of South Carolina
Columbia, SC 29208